Element composition of particulate matter in the North-West Barents Sea

Iliana – Vasiliki Ntinou

MASTER OF SCIENCE IN MARINE BIOLOGY

Supervisors:

Jorun Karin Egge

PROFESSOR, DEPARTMENT OF BIOLOGICAL SCIENCES, UNIVERSITY OF BERGEN

Tatiana Margo Tsagaraki

RESEARCHER, DEPARTMENT OF BIOLOGICAL SCIENCES, UNIVERSITY OF BERGEN

UNIVERSITY OF BERGEN
Faculty of Mathematics and Natural Sciences

DEPARTMENT OF BIOLOGICAL SCIENCES

AUGUST 2022

The front page picture was taken by Anna Vader above the Gakkel Ridge during the Arctic Basin Joint Cruise 2-2 in September 2021.

Abstract

At the dawn of the 21st century, the Arctic Ocean ecosystem is at great risk due to rapid climatic change. The ice edge retreat observed in the Barents Sea and other sub-Arctic areas is so substantial that has led researchers to characterise them as global warming hotspots. Therefore, there is an immediate need to increase our knowledge on the availability of elements, and especially those in the particulate pool to understand the aftermath of loss of sea ice in those areas. The samples and data for this thesis, were provided through the Nansen Legacy research project "The living Barents Sea", whose focus is to characterize the biological communities and processes of the northern Barents Sea and adjacent Arctic Basin. During two summer cruises with contrasting ice conditions the particulate concentration for P, S, O, Na, Mg, Cl, K, Ca, Si, Fe, Mn, Cu, and Zn, was measured with wavelength dispersive X-ray fluorescence spectroscopy along the study transect to map their distribution. A series of Pearson's correlation tests revealed two groups of elements, one associated with living material in the euphotic zone (2018: P-S-Ca & 2019: P-S-Mg-K-Na-Cl) and one with a greater prominence in the deeper samples (2018: Si-O-Fe-Mn-K-Mg & 2019: Si-Fe-O-Mn) suggesting resuspension of particulate matter. Canonical Correspondence Analysis with complementary biological and hydrographical data further confirmed these patterns and uncovered more detailed information about how the distribution of elements in the particulate pool is linked to biogenic sources in the study area. Examination of samples using a Scanning Electron Microscope revealed the most dominant organisms in the study area each year as well as supporting evidence of strong Atlantic influence in 2018 and the impact of sea ice in 2019 as shown with elemental patterns. These patterns and the investigation of their link with hydrographical and biological factors presented here provide an elaborate overview of the particulate elemental composition in the North-West Barents Sea and contribute to further understanding of the potential effects of loss of sea ice in that area.

Keywords: Particulate matter, elemental composition, marine microorganisms, Barents Sea, sea ice loss

Acknowledgements

Words cannot express my gratitude to my wonderful supervisors, professor Jorun K. Egge and researcher Tatiana M. Tsagaraki for their invaluable patience and feedback and for sharing with me their expertise and knowledge. Most of all I want to thank you for inspiring me and for trusting me throughout this journey. I am also deeply indebted to the marine microbiology group at the University of Bergen and the Nansen Legacy project who gave me the opportunity to join one of the Arctic cruises in 2021 and live the most thrilling adventures both as a scientist and as a person. Additionally, this endeavor would not have been possible without the generous support from the Bodossaki Foundation who granted me a scholarship to pursue my master's degree.

I would like to extend my sincere thanks to Irene Heggstad for her help and guidance with the Scanning Electron Microscope as well as all the technicians and researchers who analyzed the data for this thesis. Special thanks to Selina Våge for being my partner in crime on board of Kronprins Haakon as well as all the scientists and crew for embracing me on this journey. I am also grateful to my co-students for their moral support and advice during desperate times of writing this thesis.

Lastly, I am thankful to my family: mum, dad, Iason, Marissa, Andreas, my partner Kyriakos, and all my friends. Their belief and support in me have kept me motivated during tough times. I love you with all my heart.

Contents

List of abbreviations

ArW: Arctic Water

AW: Atlantic Water

Bact: Heterotrophic bacteria

BS: Barents Sea

BW: Bottom Water

C: Carbon

Ca: Calcium

CCA: Canonical Correspondence Analysis

Chla: Chlorophyll *a*

Cl: Chlorine

Cu: Copper

DM-DOM/DIM: Dissolved Matter - Dissolved Organic / Inorganic Matter

Fe: Iron

H: Hydrogen

HNF: Heterotrophic Nanoflagellates

IW: Intermediate Water

K: Potassium

mAW: modified Atlantic Water

Mg: Magnesium

Mn: Manganese

N: nitrogen

Na: Sodium

Nano: Nanophytoplankton

O: Oxygen

P: Phosphorus

Pico: Picophytoplankton

PM-POM-PIM: Particulate Matter – Particulate Organic / Inorganic Matter

S: Sulfur

SEM: Scanning Electron Microscope

Si: Silicon

wArW: warm Arctic Water

WDXRF: Wavelength Dispersive X-Ray Fluorescence spectroscopy

Zn: Zinc

1. Introduction

The marine ecosystems on Earth comprise a tremendous amount of microbial diversity and abundance that, together with physical and chemical processes, govern the pathways and cycling of biologically essential elements within the marine environment (Arrigo, 2005; Azam et al., 1983). Since the beginning of the 20th century and the pioneering work of Alfred Redfield (Redfield, 1934), our knowledge of the relationships between bioinorganic chemistry and marine biogeochemistry has been steadily growing (Morel et al., 2003). The ongoing flow and balance of elements between the organisms with unique elemental composition and their environment, include among other processes, assimilation, transfer, and mineralization (transformation of organic to inorganic compounds) and is the concept of ecological stoichiometry (Sterner & Elser, 2008).

Matter is made up of chemical elements required for regular functions of living organisms and is abundant in nature in different forms, some directly available for uptake and use and some not (Frausto da Silva & Williams, 2001). The widespread way of characterizing different fractions of matter is based on the size of the particles. Typically, all matter that consists of particles larger than 0.22-0.45 µm is defined as particulate matter and can be retained on filters. In contrast, anything smaller than that is referred to as dissolved matter (Volkman & Tanoue, 2002). Each group is then subcategorized depending on whether they consist of organic or inorganic compounds (Greenwood & Earnshaw, 2012).

Inorganic particles in oceanic systems have various origins. These include erosion by weathering processes (e.g. rivers), land surface drainage, and hydrothermal vents, as well as deposition of biogenic material (e.g., siliceous frustules of diatoms and radiolarians, which are composed of opaline silica ($SiO_2.nH_2O$), $CaCO_3$ shells of coccolithophorids and foraminifera) (Langer, 2008) in the forms of dissolved inorganic matter (DIM) and particulate inorganic matter (PIM) (Frausto da Silva & Williams, 2001). Dissolved organic matter (DOM), on the other hand, includes colloids (<1 µm), viruses, small bacteria, and true solutes (low-molecular-weight compounds: polysaccharides and amino acids). Often DOM materials aggregate to form particles.

Thus, DOM and POM form a continuum, with microbes found in both fractions (Verdugo et al., 2004).

1.1. Marine particulate matter and its constituents

Marine PM or seston is a heterogeneous mixture of living organisms and organic detritus and inorganic particles, which may vary substantially in their elemental compositions in terms of quality and quantity (Collier & Edmond, 1984). During the course of a bloom, phytoplankton constitutes a large fraction of POM together with zooplankton, protists, flagellates, and large bacteria (Verdugo et al., 2004). Additionally, other types of labile particles like organic detritus and lithogenic inorganic materials form particle assemblages in the water column. They can, together with plankton cells and zooplankton fecal material, form large aggregates held together by transparent exopolymeric particles released from plankton, known as marine snow (Grossart et al., 2006; Munn, 2019).

There are various sources of PM in marine systems. Some are connected to terrestrial input (rivers), erosion (heavy rainfall and snowmelt), aerial deposition of dust particles (wind-blown dust, volcanic ash, and cosmogenic dust), crustal enrichment (sediment resuspension) and as mentioned earlier to biogenic origin (Price & Skei, 1975). This variability in the sources of PM is the reason for the great variability in its elemental composition and availability of chemical elements in oceanic systems. If we want to grasp the mechanisms behind nutrient dynamics and energy transfer in the food web or even the evolutionary history behind elemental stoichiometry it is imperative to collect observational data that map the distribution of particulate elemental composition (Finkel et al., 2006; Quigg et al., 2003; Sterner & Elser, 2008). But before that, it is important to understand a little bit about the role of elements and their cycles in marine ecosystems.

Among the 20 essential elements for all marine organisms (Quigg, 2008), C, H, O, N, P, S make up >95% of the total mass of organic matter, mainly in the form of carbohydrates, proteins, nucleic acids and lipids, which have vital roles in the cells (Munn, 2019). P is typically the fifth most abundant element in organisms as it is a constituent of molecules (e.g., DNA, RNA, and phospholipids) and biominerals (e.g., Ca phosphate), it acts as a carrier for energy (e.g., adenosine 59-triphosphate, ATP) and substrates (e.g., glucose phosphate) and it participates in signaling paths (e.g.,

cyclic adenosine monophosphate, c-AMP) (Kay & Vrede, 2008; Vrede & Kay, 2008). However, P is constantly alternating between its organic and inorganic form through microbial activity (White & Dyhrman, 2013). Heterotrophic and autotrophic microbes compete for available P, which affects productivity and that is why its availability has a major limiting effect on oceanic primary production rates and microbial community composition (Thingstad et al., 1993). For almost a century now, it has become a norm for oceanographic and marine studies to use P normalized quotas to characterize the trophic state of a certain system and provide information about the distribution patterns of elements and stoichiometric relationships of natural samples, cell cultures or individual cells (Geider & La Roche, 2002; Ho et al., 2003; Lomas et al., 2019; Martiny et al., 2013; Quigg et al., 2003; Redfield, 1934).

The oceans are the biosphere's greatest repository of S (in the form of sulfate). Even in the most extreme conditions, such as hydrothermal vents, anoxic sediments, and P-dominated supraglacial spring systems, organisms utilize it as a source of energy generation and integrate it into organic compounds like proteins and sulfolipids (Munn, 2019; Trivedi et al., 2018). Despite the abundance of sulfate in seawater, most marine microbes obtain S from recycling of dimethyl sulfoniopropionate (DMSP) which is a compound produced by algae, such as *Phaeocystis globosa* and *Emiliania huxleyi* and some dinoflagellates species. In the cells, DMSP can protect against osmotic stress (Yoch, 2002), but on a greater scale, the DMSP cycle is thought to be a major driver in climate forcing according to the CLAW hypothesis (the acronym stands for the surnames of the scientists who proposed it) (Charlson et al., 1987).

As a component of oxide compounds such as SiO_2, O is the most abundant element in the Earth's crust by mass (Greenwood & Earnshaw, 2012). A wide range of biological and abiotic activities regulate the cycle of O in the atmosphere. Significant progress has been made in understanding the mechanisms that govern concentration of O, particularly as it is a major factor in coupled biogeochemical cycles of many elements, including C, P, N, S, Si, Ca, Fe, and others (Petsch, 2014).

Seawater consists of 6 principal ionic components that account for >99% of the weight of salts. These are Na (55 %), Cl (31%), S (8%), Mg (4%), Ca (1%), and K (1%) (Vrede & Kay, 2008). That is why, aside the essential elements described in the earlier paragraphs, all marine organisms require inorganic ions, as their survival depends

highly on precise osmotic control. Na, K, and Cl, are also of great significance in a number of physiological processes like electrolytic balances, stability of DNA and membranes, chemical uptake of organic metabolites (Frausto da Silva & Williams, 2001). Mg has been found to be an important cofactor for a number enzymes and the chlorophyll molecule, participate in phosphate transfer as well as act as an osmolyte for marine bacteria (Frausto da Silva & Williams, 2001; Heldal et al., 2012). Ca among its various roles in cellular physiology (Frausto da Silva & Williams, 2001), is particularly important for calcifying plankton organisms, as it is a basic component of their cell wall structures in the form of $CaCO_3$ (Langer, 2008; Munn, 2019). *Emiliania huxleyi*, a marine coccolithophore, is one of the most important $CaCO_3$ producers on earth (Fagerbakke et al., 1994; Krumhardt et al., 2017). Unfortunately, there are strong indications that ocean acidification due to climate change combined with Fe repletion will create unfavorable growth conditions for *E. huxleyi* causing it to expand to northern areas and thus significantly affecting the biological C pump (Rosario Lorenzo et al., 2018; Winter et al., 2014).

The biological pump from the upper water column is majorly influenced by the sinking material originating from phytoplankton and especially diatoms (marine snow, resting spores, zooplankton fecal pellets etc.) and is responsible approximately for 40% of oceanic C sequestration (Munn, 2019; Tréguer & De La Rocha, 2013). Si is the essential limiting nutrient for the growth of diatoms as they use it to build their cell wall (frustule) (Borowitzka et al., 2016; Egge & Aksnes, 1992; Lomas et al., 2019) and is also utilized by radiolarians, silico flagellates, several species of choanoflagellates, and some picocyanobacterial (Tréguer & De La Rocha, 2013). Si rarely occurs free but is almost exclusively in the form of silicate dioxide (SiO_2) or silicate (SiO^{4-})(Greenwood & Earnshaw, 2012). Therefore, the Si cycle is strongly coupled with the O cycle and the C flux in marine systems (Egge & Aksnes, 1992; Larsen et al., 2015; Thingstad et al., 2005).

Trace elements are those required in minor quantities (typically <0.01%) by the organisms to maintain proper physiological functions (Quigg, 2008). Among them the most abundant are Fe, Zn, Mn, Cu (Twining & Baines, 2013) which are components of metal-containing enzymes and take part in redox reactions (Frausto da Silva & Williams, 2001). For instance, Fe is a major component of cytochromes and an

important cofactor of enzymes in many metabolic pathways of protists and bacteria (e.g., photosynthesis, N fixation, etc.), and has been reported to be limiting for biological activity in large oceans (Behrenfeld et al., 1996; Frausto da Silva & Williams, 2001; Morel et al., 2003; Munn, 2019). That is why different phytoplanktonic species have developed competitive iron uptake strategies that create complex interactions among functional groups and regulate iron availability in natural systems (Sanchez et al., 2018).

1.2. Microorganisms and their role in the marine ecosystem

Microorganisms are the most abundant organisms on earth, and they play a vital role in the global biogeochemical cycles of the elements (Arrigo, 2005). They are the major components of plankton in many oceanic and coastal regions(Bratbak et al., 2011). They are very often associated with suspended material in the water column but are also found in high abundances in the sea ice and in the marine sediments. An operational approach to categorize microbial plankton groups is to classify them by size. Femtoplankton consists of organisms whose size range falls between 0.01–0.2 µm e.g., marine viruses. Slightly bigger organisms like bacteria, archaea and some eukaryotic protists with a size of 0.2–2 µm belong in a group called picoplankton (Munn, 2019). However, picoplankton, includes both autotrophic and heterotrophic organisms which of course have very different functional roles, therefore it is important to specify the type of picoplankton group one is referring to (Marshall, 2002). To distinguish between autotrophic eukaryotic picoplankton and bacteria it is common to use the term picophytoplankton for the first ones. Because bacteria also can be autotrophic (e.g. cyanobacteria) and generally are the most common and abundant taxa within the autotrophic picoplankton, in many studies they are often grouped separately (e.g. *Synechococcus*)(Marshall, 2002). For the purpose of this thesis, autotrophic eukaryotic picoplankton (e.g., Chlorophytes, Chrysophytes, Haptophytes, Prasinohytes, etc.) will be referred to as picophytoplankton and heterotrophic bacteria belonging to picoplankton as bacteria (Marie et al., 1999; Zubkov et al., 2006). Nanoplankton is the group that comprises organisms from 2 to 20 µm big. Nanoplankton includes among others, diatoms, coccolithophores and

other flagellates (Munn, 2019). Again, in this thesis the term nanophytoplankton will be addressing the autotrophic nanoplanktonic organisms and heterotrophic nanoflagellates (HNF) the heterotrophic organisms in this group respectively (Marie et al., 1999). Finally, microplankton is a term used for organisms with a size between 20–200 μm and that includes ciliates, some very big diatoms, dinoflagellates, foraminifera, etc., and is a highly important component of PM (Munn, 2019).

Our understanding of the recycling of elements within the oceanic food web and between the organisms and their environment has drastically changed the last century. Today, it is broadly accepted that microbes are central factors to the modern understanding of this food web, especially in the photic zone (Azam et al. 1983; Thingstad et al. 2007). The microbial food web links nutrient and C chemistry and energy transfer through the food chain or interior export to the seafloor. Numerous studies have shown that phytoplankton species show variation in their elemental requirements and composition (Bratbak & Thingstad, 1985; Egge & Aksnes, 1992; González-Dávila, 1995; Klausmeier et al., 2004; Lomas et al., 2019; Quigg et al., 2003; Sakshaug et al., 1983; Twining & Baines, 2013). This variation in composition influences both the stoichiometry of phytoplankton-derived PM (Finkel et al., 2006; Klausmeier et al., 2004; Rembauville et al., 2016; Sterner & Elser, 2008).

The first studies on the elemental content of marine PM started to appear during the 1970s (Martin & Knauer, 1973; Price & Skei, 1975). Later, more studies followed that examined the major element compositions as well as ratios from plankton samples to try and link their significance to the fluxes that determine the major element cycles (Collier & Edmond, 1984). Some researchers shed light to the origin (natural/anthropogenic) and spatial distribution of elemental composition of PM in the North Atlantic and the Svalbard area (Barrett et al., 2012; Bazzano et al., 2014). Alongside those efforts, the pioneer technology of X-ray spectroscopy gave the opportunity to reveal the elemental content of PM from water samples (Paulino et al., 2013) and was also used in comprehensive studies that related its seasonal variability to biological and large scale hydrographic processes such as the North Atlantic Oscillation (Erga et al., 2017).

Concurrently, the field of elemental stoichiometry was developing (Sterner & Elser, 2008), expanding from the traditional Redfield ratio to including trace elements

(Twining & Baines, 2013) as researchers gradually realized that there is great variability of the elemental composition between different organismal groups (Frigstad et al., 2011; Geider & La Roche, 2002; Klausmeier et al., 2004). This variability has been attributed to environmental factors (e.g., irradiance) and evolutionary history of marine organisms in seawater (Finkel et al., 2006; Quigg et al., 2003). Consequently, there is an growing need to study which factors and processes affect the distribution of elements in the PM pool, especially in areas that are drastically transformed due to climate change.

1.3. The Barents Sea

The Barents Sea expands from the border with the Norwegian Sea eastwards to Novaya Zemlya Sea with a latitude ranging between 68.5 – 82.6 N up to the Arctic Continental Shelf edge (Figure 1). In total, it covers an area of around 1.6 million km^2, with an average depth of 230 m (~500m maximum)(Sakshaug et al., 2009).

Spatial and temporal variability in the advection of water masses and sea ice cover, are typical characteristics of the BS (Dalpadado et al., 2012; Loeng, 1991). It has been found that the NAO index has a substantial impact on cyclonic circulation and hydrography in the BS on a decadal timeframe (Loeng, 1991; Loeng & Drinkwater, 2007). On an annual basis, however, fluctuations in sea temperatures are controlled by Atlantic inflow in the southern portion, Arctic water and sea ice influx in the northern section, and heat exchange with the atmosphere (Loeng, 1991; Loeng & Drinkwater, 2007). Consequently, this current fluxes and the bathygraphy, confine the water mass distribution in the BS (Oziel et al., 2016).

The annual average primary production in the whole BS is approximately 90 g C per m^2 but it can fluctuate anywhere between 10 and 700 g C per m^2 (Sakshaug et al., 2009). Years of observations and thorough research in the BS (Sakshaug et al., 1992; Sakshaug et al., 2009) suggest that it is becoming the first ice-free Arctic Sea and with the most profound changes taking places in the northern and eastern BS particularly after 2005 (Screen & Simmonds, 2010; Årthun et al., 2012), so much so that it is characterized by researchers as a global warming hotspot (Lind et al., 2018). Over the last few years, the observed 30% increase in net primary production in the BS region, has been attributed to the decline in sea ice cover due to warming (Dalpadado et al., 2020; Loeng & Drinkwater, 2007). Despite the increase in the

primary production, there is still great incertitude on the exact impact on the species distribution and the food web linkages (Dalpadado et al., 2012; Haug et al., 2017; Ingvaldsen et al., 2021; Oziel et al., 2020).

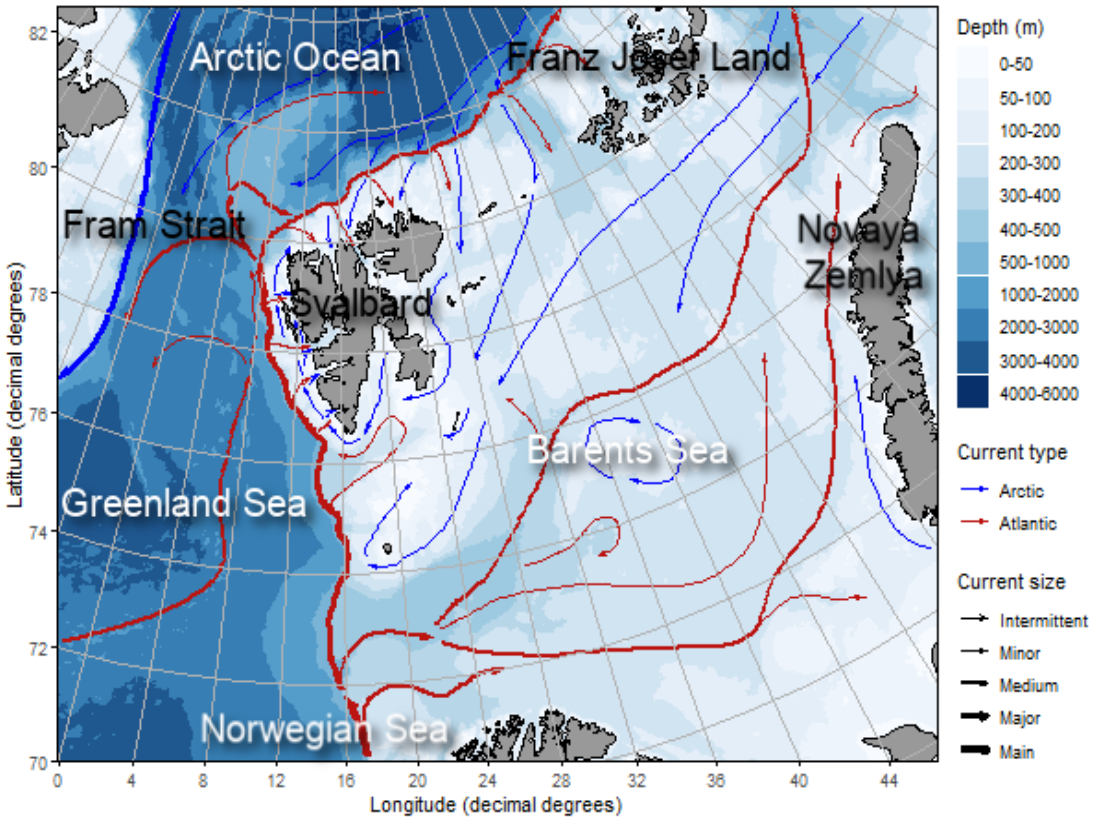

Figure 1. Bathymetric map of the Barents Sea. Arrows represent water currents and their size, Red: Atlantic current & Blue: Arctic current.

1.4. Aim of the thesis

In order to collect information about the chemical composition and distribution of oceanic PM and identify potential patterns and changes due to fluctuating sea-ice conditions, samples for elemental composition were collected along the Nansen Legacy transect during two consecutive summers (2018-2019). The aim of this thesis can be divided into three parts:

- To map the particulate element distribution of P, S, O, Na, K, Cl, Mg, Ca, Si, Fe, Mn, Cu and Zn during two summers of contrasting sea ice conditions in the North-West BS.
- To calculate the correlations and stoichiometric relationships between the elements.
- To investigate the elements' origins and identify the degree to which certain key biological and environmental factors (i.e., chlorophyll *a*, microbial abundances, temperature, salinity) can assist in interpreting the observed elemental patterns.

2. Materials and methods

2.1. Nansen Legacy transect

The samples used for this study were collected from the Nansen legacy process stations P1-P5 in the North-West Part of the BS (Figure 2) covering the northern BS from south of the Polar Front towards the Arctic Ocean (https://arvenetternansen.com/). The sampling was conducted on the Norwegian research icebreaker R/V Kronprins Haakon throughout the course of two research cruises which took place on the 6th-23rd of August 2018 (JC1-2: Joint Cruise 1-2) and 5th-27th of August 2019 (Q3: reference to the 3rd quarter of the year). In the JC1-2 cruise the process stations P1-P5 that were conducted were all open water stations. On the Q3 cruise, seven process stations (P1, P2, P3, P4, P5, P6 and P7) were conducted, of which the first four were open-water stations on the shelf (P1, P2, P3, P4), while the ones situated on the shelf (P5), slope (P6) and deep Nansen Basin (P7) were covered by ice. To compare the two years, only data from stations P1-P5 were analyzed in this thesis.

This area is hydrographically characterized by six water masses based on the description by Sundfjord et al. (2020):

- Arctic Water (ArW): Sea ice melt water is exported southward from the Arctic Ocean onto the BS shelf which then circulates northward back and sinks into the Arctic Ocean (Aagaard & Woodgate, 2001). This water mass is easily recognized by its low salinity (<34.9 PSU) and temperatures below zero.
- Warm Arctic Water (wArW): This water mass can be a result of warming of ArW either by solar radiation or by mixing with Atlantic Water (>0°C, <34.9 PSU).
- Atlantic Water (AW) : Advected from the North Atlantic into the Southwest BS, the Fram Strait, the Eastern Eurasian Basin, and the Arctic Basin (Figure 1). This warm (>2°C) and saline (>34.9 PSU) water mass is distinct from the cold surface water further north due to the strong stratification.
- Modified AW (mAW): The term is used to describe the AW mass that has lost its heat (0<T<2°C & >34.9 PSU) due to sea ice formation and melting.
- Intermediate Water (IW): This definition describes the water mass that has even lower temperature (<0°C & >34.9 PSU) than mAW and is usually found deeper.

- Bottom Water (BW): A locally formed water mass with extremely low temperature (<-1.1°C) and high salinity (>34.9 PSU), as a result of the sinking of a dense surface layer during autumn when the release of brine during sea ice formation and cooling of the atmosphere occurs.

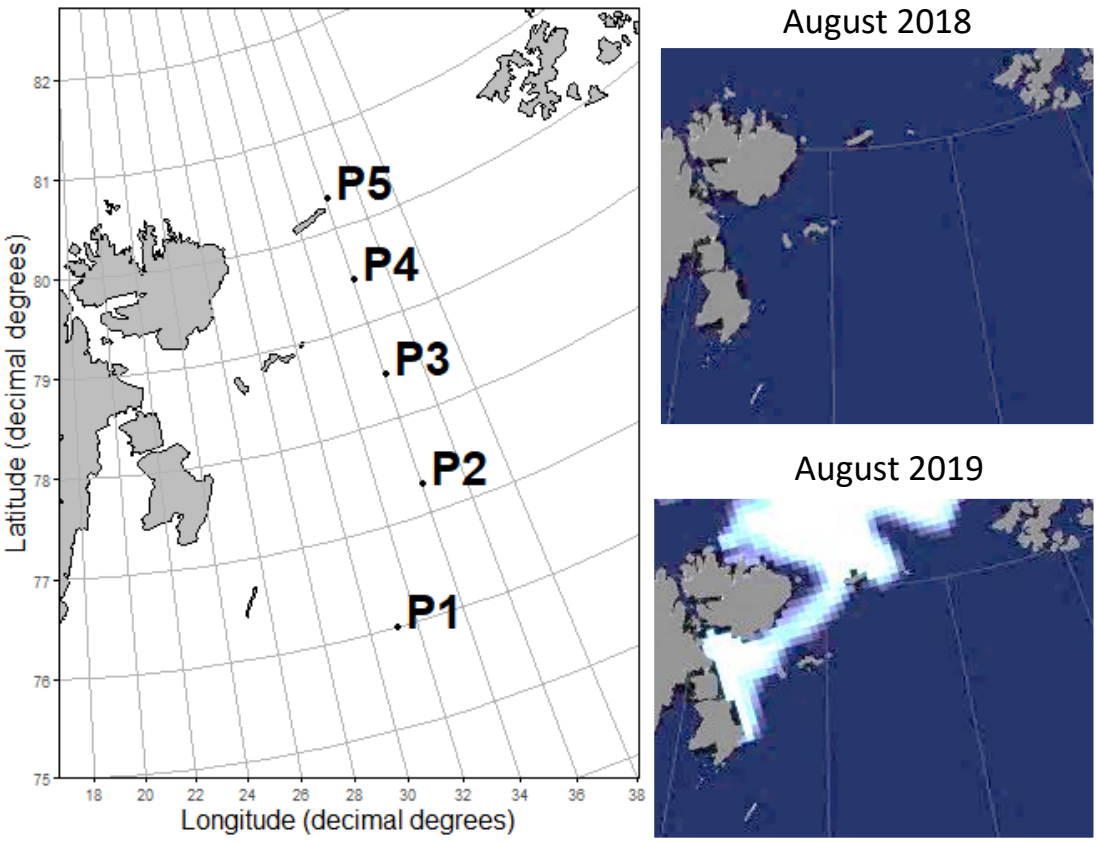

Figure 2. Map of the Nansen Legacy process stations P1-P5 in the North-West Part of the Barents Sea (left). Sea ice coverage for August 2018 (right-top) and August 2019 (right-bottom) Map built under the PlotSvalbard package (Vihtakari, 2020) and sea ice coverage data during the corresponding study periods were provided from https://resources.marine.copernicus.eu/

2.2. Hydrological parameters: temperature and salinity

A SBE 911plus CTD system (Sea-Bird Scientific, WA, USA), documented temperature and salinity, which were used to identify water masses in the study area. The CTD was lowered vertically at a speed between 0.8- 1 m/s on each station and values were recorded upwards.

A 24-Niskin-bottle rosette attached to the CTD cage was use to acquire samples on the upcast for particulate elemental composition, chlorophyll *a*, and flowcytometry at the assigned standardized sampling depths: 5, 10, 20, 30, 40, 50, 60, 90, 120, 150, 200 m, DCM (Deep Chla max: only if present and significantly different from standard depths, i.e., ± 5m) and Bottom-10 m (lowest sampling depth always 10 m above the seafloor to avoid damage to the equipment). Further cruise and sampling details are described in The Nansen Legacy Sampling Protocols (2020a).

2.3. Elemental concentrations of particulate matter

Water samples were acquired with a Niskin-bottle rosette attached to the CTD cast. Samples were taken from the standard depths on every station. The water samples were collected directly from the Niskin bottles into plastics containers that were cleaned with distilled water beforehand and rinsed with a small sample volume before being filled. If necessary, the containers were kept in a dark and cold place until filtration. Right before filtration the containers were gently agitated to resuspend any sunken material. For the total particulate element analysis approximately 1.5 L from each water sample was filtered in triplicate on Whatman® Nuclepore™ polycarbonate (PC) filters, 47 mm in diameter, 0.6 µm pore size, using ≤200 mmHg vacuum pressure. After filtration, each filter was rinsed with 5 ml of distilled water to prevent interference from salt crystals, then left to air-dry and kept try in petri slides until further analysis. Total particulate concentrations of P, S, O, Na, Cl, K, Mg, Ca, Si, Fe, Mn, Cu, and Zn were measured by wavelength dispersive X-Ray fluorescence spectroscopy (WDXRF) in a Bruker® AXE S4 pioneer XRF instrument at the University of Bergen (Figure 3). PC filters have high content of C, and this high background will obscure the WDXRF measurement for that particular element. In addition, N cannot be precisely measured due to influence from the strong C peak (Paulino et al., 2013). C and N are therefore not included in this investigation.

WDXRF analysis has a lot of benefits as it is non-destructive, non-invasive, and requires little preparation of the samples (Gamela et al., 2020). The concentration for the above-mentioned chemical elements was calculated based on the calibration parameters and detection limits explained in Paulino et al. (2013) (Appendix 6.1, Equation 1). The instrument provides a bulk amount of particulate element concentration and does not discern between different chemical forms. At least three blank filters from each new batch and three filters with filtered distilled water were analyzed for reference prior to analyzing the samples. Standard error (SE) is given for all sampling points. More detailed information can be found in the Nansen Legacy Sampling Protocols (2020a).

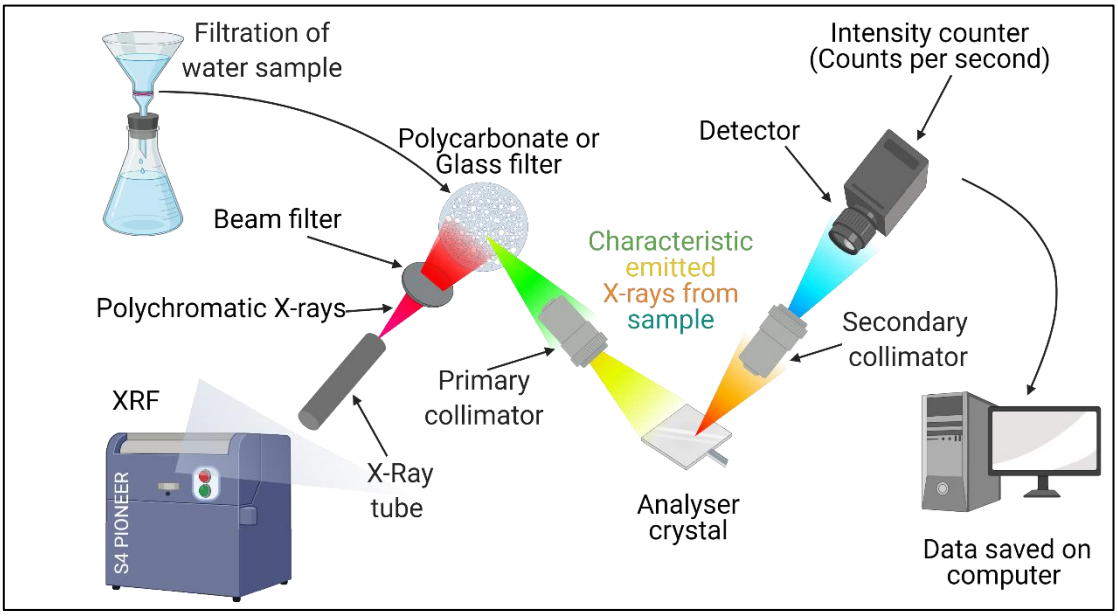

Figure 3. Schematic representation of the main principles of wavelength dispersive X-Ray fluorescence spectroscopy (WDXRF), used to measure particulate elemental stoichiometry from water samples.

2.4. Determination of chlorophyll *a*

Data for quantification of chlorophyll *a* and phaeopigments using the fluorometric acidification method were acquired according to the methodology described in the Nansen Legacy protocols (2020b) Appendix 6.1, Equation 2).

2.5. Abundance of bacteria and small protists

Samples for enumeration of bacteria, heterotrophic nanoflagellates, picophytoplankton, and nanophytoplankton by flow cytometry were analyzed following the methodology described the Nansen Legacy Protocols (2020c)(Appendix 6.1).

2.6. Identification of algal species

For the goal of identifying the PM constituents in samples of interest, some filters used for determination of particulate elemental stoichiometry were prepared to be viewed with a Quanta FEG 450 and a SUPRA 55V scanning electron microscope, at 250–3500× magnification or higher if necessary. SEM specimens were prepared by mounting the filters on Al-stubs and coating them with iridium or gold/palladium in a Polaron SC502 Sputter Coater for 30 s.

2.7. Statistical analysis

Addressing the distribution of the measured variables is the perquisite for choosing the appropriate statistical method and tools to analyze a dataset. For that purpose, a Shapiro-Wilk's test was performed to assess the normality of the distribution of the data (Appendix 6.2). To assess the significance of differences of the measured element concentrations parameters and microbial abundances between the two summers a Welch's ANOVA test together with a pairwise t-test was performed. The Welch's ANOVA test was chosen as it does not assume a normal distribution for the data therefore is non-parametric and is less sensitive to heteroscedasticity (Moder, 2016). P-values were adjusted using the Bonferroni correction. The Bonferroni method is a multiple-comparison correction used when several dependent or independent statistical tests are performed simultaneously to avoid a lot of spurious relationships (type I errors)(Armstrong, 2014).

One of the goals of this this thesis was to describe the distribution of the elements in PM in association with the distribution of microbial groups. Therefore, a series of Pearson correlation tests were performed with the Bonferroni correction method to see if there are any correlations between and among the element concentrations and the microbial groups. The correlation coefficient (a) between for any response-predictor relationship was set at a level of $|a| > 0.3$ to account for the number of comparisons being performed.

Canonical correspondence analysis (CCA) was performed to investigate the relevance of the element concentrations of PM in explaining variation in microbial abundances in the study area. CCA is a constrained ordination method used widely in aquatic studies where a low dimensional ordination space is created through linear

combinations of environmental variables, which makes it a useful method for detecting environmental variables that 'best' describe variation in biological data (Ter Braak & Verdonschot, 1995). In such a space, similar samples are plotted close together while dissimilar ones are placed far apart. It is generally applied to identify and measure associations among two sets of variables where one of them has observations (for example, species abundances in each studied site) and the other has gradients (for example, measurements of environmental variables in each studied site). Here, CCA is used as a tool to help better understand how and why some of these variables could be strongly linked. An initial model including all element concentrations was evaluated with the vegan package in R. To avoid downweighing of the model, a Hellinger transformation was performed on both matrices. The choice of constraining variables in the final model was decided using forward selection with the double stopping criterion as implemented in the ordistep function in Vegan (Blanchet et al., 2008). ANOVA-like Monte Carlo permutation tests (n=999) were implemented to find out which vectors (elements) were statistically significant to explain the variance of the response variables (microbial groups) as well as the significance of the whole model (Appendix 6.2). The results were depicted in a CCA biplot.

All data manipulations and statistical analysis was performed in RStudio and visualization of data was done with the ggplot2 package (R Core Team, 2017; Wickam, 2016). The results for temperature, salinity, elemental concentrations, and chlorophyll *a* are depicted in section plots busing the algorithm Multilevel B-spline Approximation (MBA) for data interpolation as it is implemented in the PlotSvalbard package R (Lee et al., 1997; Vihtakari, 2020). An online repository with all datasets and detailed scripts is available on GitHub (https://github.com/ilianauib/MasterThesis).

3. Results

3.1. Temperature and salinity

The hydrological parameters (temperature and salinity) were investigated to distinguish the origin of the water masses along the Nansen Legacy transect. In August 2018, there appeared to be in general higher temperatures (Welch's ANOVA: F=26.3, p<0.001) compared to August 2019, especially above 40 m depth in all stations. In 2018, P1 was the station with the highest temperature (max: 5.7°C) even down to 240 m depth where the sea temperature was just above 2°C (Figure 4). On the contrary in August 2019 stations P4 and P5 were dominated by water below -1°C, and temperatures above 2°C were found only in the surface layer of P1 and P2 stations.

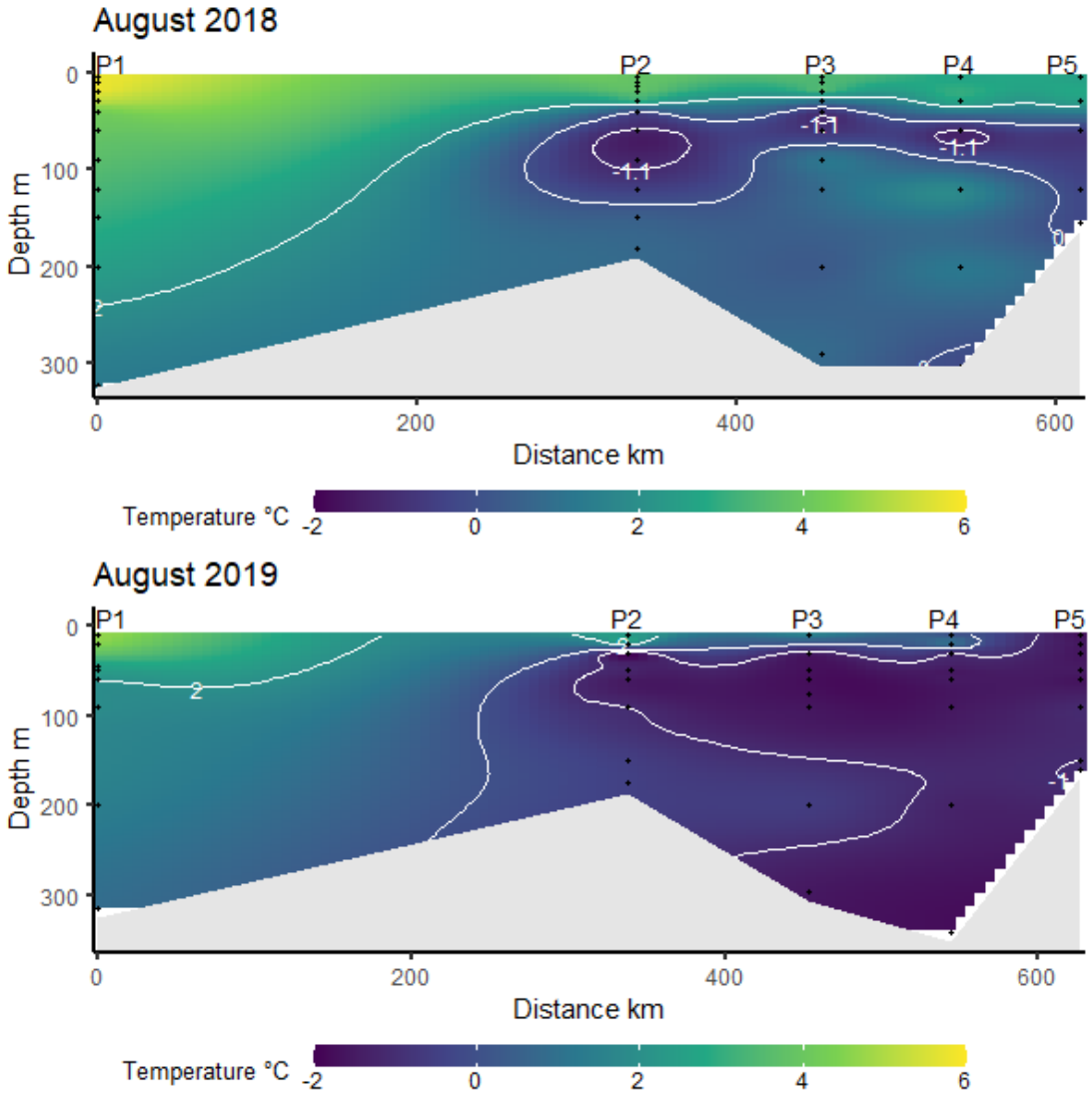

Figure 4. Depth section plots of temperature along the study transect for August 2018 and August 2019. Black dots correspond to sampling points. Contour lines are drawn at -1.1°C, 0°C and 2°C.

Salinity values didn't fluctuate significantly between the two years (p=0.06) however there appeared to be a dominance of less saline water with <34 PSU documented in the surface of P5 (32 PSU), P4 (33 PSU), and P3 (33.8 PSU) in 2019 (Figure 5). Overall, in 2018 the water column appeared to be more mixed with a warm surface layer stretching over the whole study area, while in 2019 there was a greater influence of more cold and less saline water in the study area spreading southwards from the northern part of the transect.

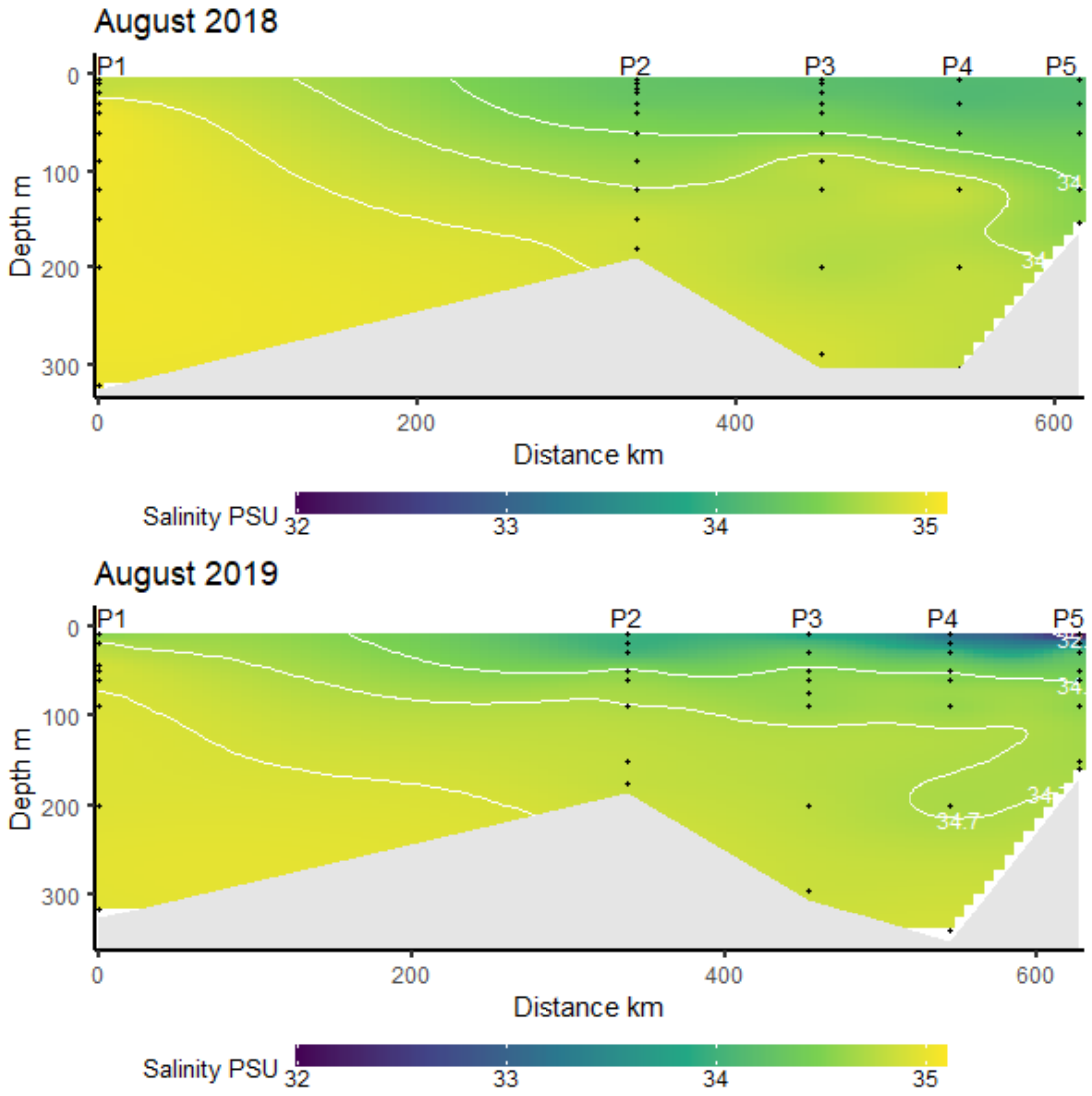

Figure 5. Depth section plots of salinity along the study transect for August 2018 and August 2019. Black dots correspond to sampling points. Contour lines are drawn at 32.4 PSU, 34.5 PSU, 34.7 PSU AND 34.9 PSU.

3.2. Distribution of particulate elemental composition

The results for particulate elemental composition are depicted in section plots. Each plot has its own separate scale to account for the variable range of the measured values on each year. Additionally, the depth axis on some of the plots is in log scale for visualization purposes.

Phosphorus

Particulate P concentrations varied between 0.012±0.004 µM - 0.191±0.006 µM in August 2018 and 0.015±0.000 µM - 0.276±0.021 µM in August 2019 (Figure 6). Although highest concentrations for particulate P were observed above 75m depth for both years and there was not a significant difference in the documented concentrations between the year (Welch's ANOVA: $F=2$, $p=0.15$), its distribution differed largely from one year to the other. As shown in Figure 5, in August 2018 the highest value of particulate P was documented at 20 m depth in the lowest latitude (P1 76N). It is also noteworthy that in 2018 elevated values of P were also documented at P2 station (40m: 0.085±0.006 µM), at P3 40m:0.102±0.123 µM) the bottom samples of the first two stations (P1, 322m: 0.095±0.019 µM and P2, 181m: 0.085±0.006 µM). On the other hand, in August 2019, the maximum concentration of particulate P was observed at the ice covered station P5 between 10-20 m depth (0.264±0.013µM - 0.276±0.021µM), while high values were also registered at P4 30m (0.149±0.010 µM) and at P2 50m (0.143±0.06 µM).

Sulfur

Concentrations of particulate S ranged between 0.004±0.001 µM – 0.046±0.009 µM in 2018 and 0.005±0.001 µM – 0.074±0.023 µM in 2019 (Figure 4), with the latter being significantly higher (Welch's ANOVA: $F=21.1$, $p<0.001$). The distribution varied similarly with particulate S with three distinguishing exceptions (Figure 7). Specifically, in August 2019 the area with the maximum particulate S was found just below the surface (10m) at P2 station with high concentrations (0.058±0.009 µM) also detected down to 30-50m. Another area with high S was the top 20m at P5 (0.066±0.003 µM) and 30m at P4 (0.053±0.004 µM). Interestingly the year prior, elevated concentration of sulfur was documented at 10m depth at P1 station (0.046±0.009 µM).

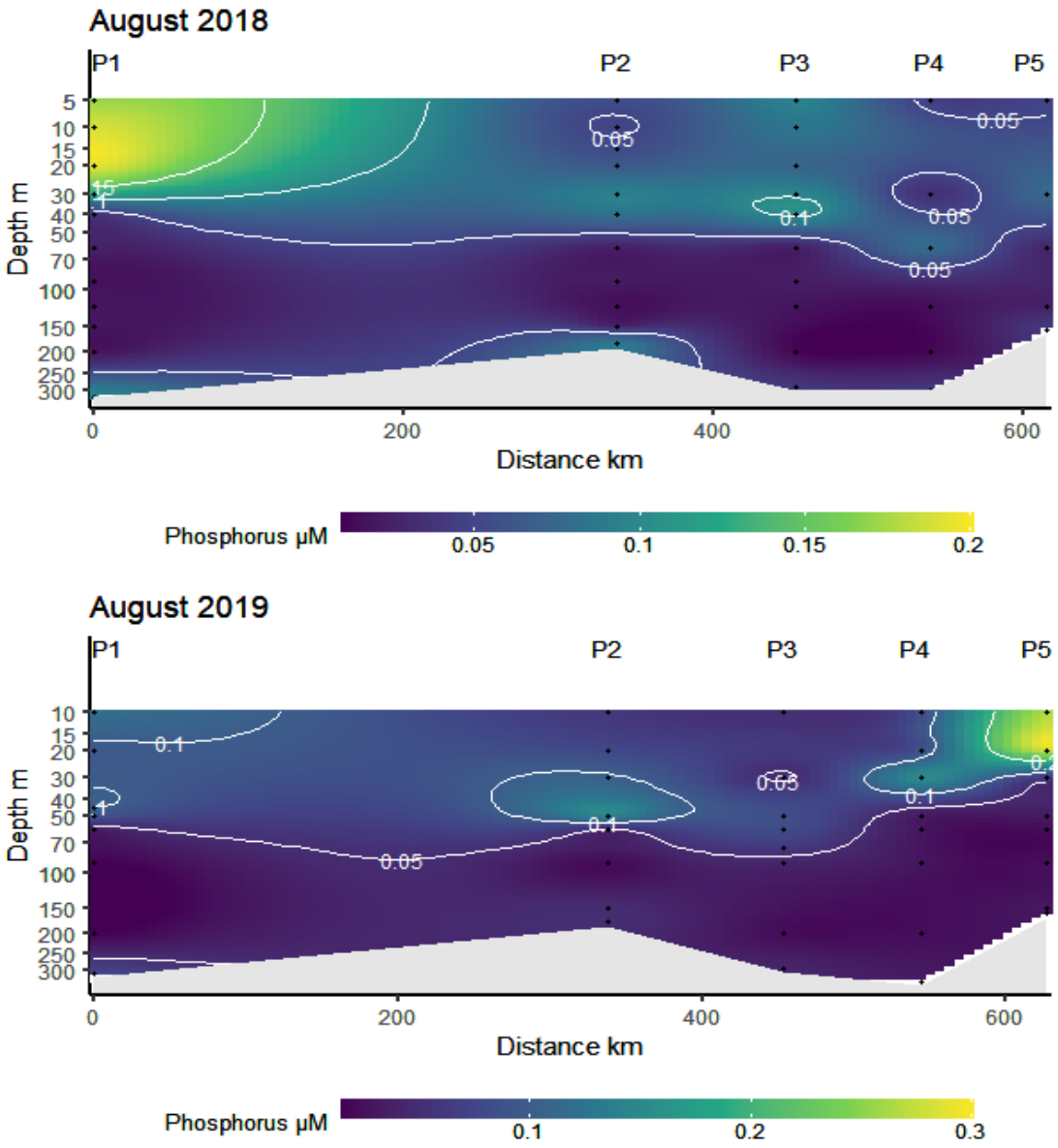

Figure 6. Distribution of particulate P in µM during August 2018 and August 2019 for all five stations of the Nansen Legacy Transect from 76°N to 80.3°N (left to right). Black dots correspond to sampling points. Depth axis is in log scale. Notice the different scale for each year at the bottom of each plot.

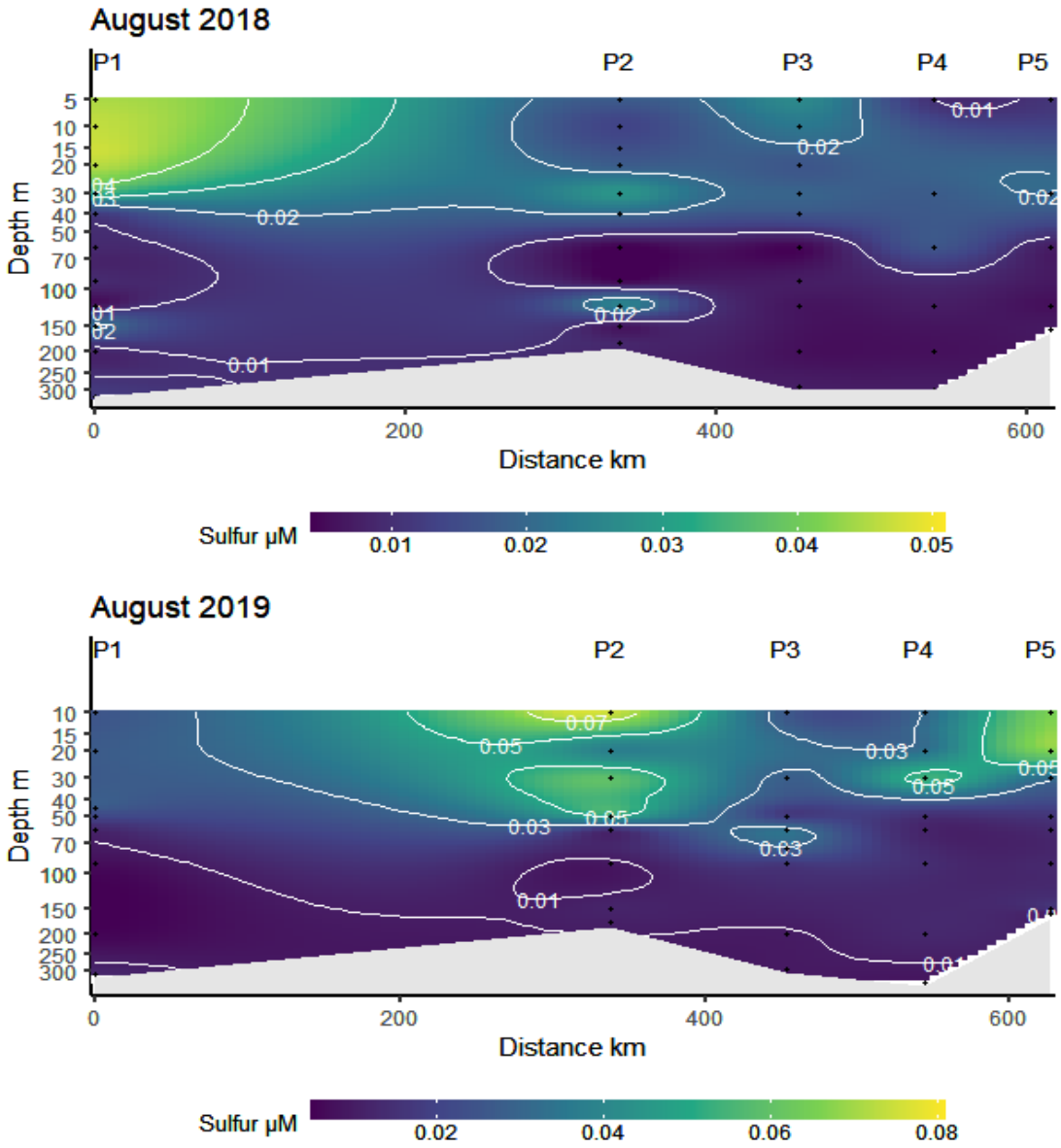

Figure 7. Distribution of particulate S in µM during August 2018 and August 2019 for all five stations of the Nansen Legacy Transect from 76°N to 80.3°N (left to right). Black dots correspond to sampling points. Depth axis in log scale. Notice the different scale for each year at the bottom of each plot.

Oxygen

Unlike P and S, the highest concentration of O was observed in deep water/close to bottom. Particulate O concentration (Figure 8) varied between 0.064±0.000 µM– 0.622±0.071 µM in 2018 with two exceptionally high values 1.707±0.341 µM and 1.465±0.073 µM at the bottom of P1 (322m) and P2 (181m) respectively. On other hand, in 2019 O concentration of the PM ranged between 0.085±0.004 µM - 1.241±0.120 µM (lowest: P2 90m, highest: P1 315m). Despite the similar distribution between the two years and those two high values in 2018 mentioned above, the O concentration of the PM in 2019 was significantly higher than the previous year (Welch's ANOVA: F = 9.2, p<0.005). Another clear difference in the distribution of particulate is a "hotspot" of high particulate O (1.048±0.073 µM) at 5m

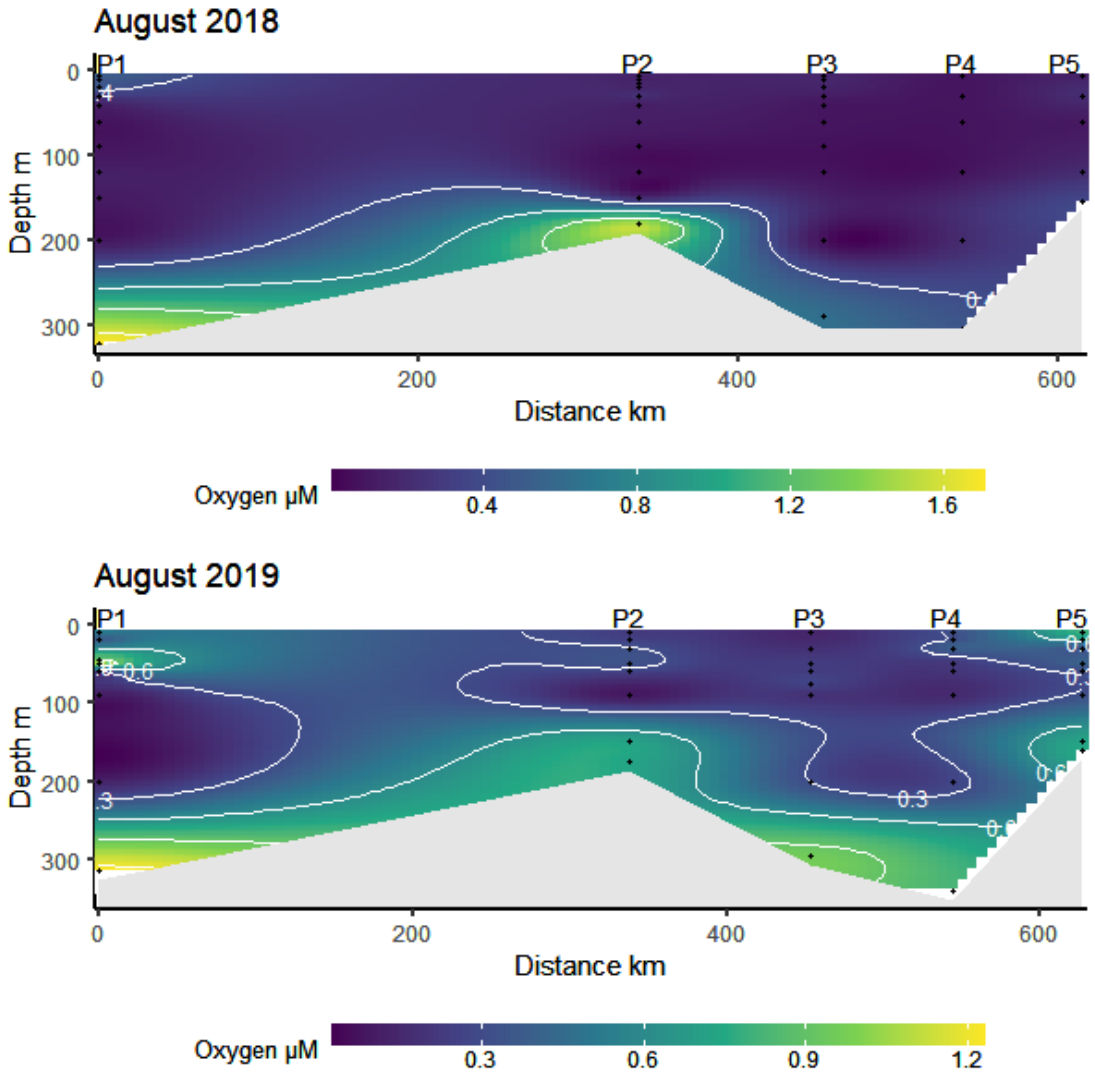

Figure 8. Distribution of particulate O in µM during August 2018 and August 2019 for all five stations of the Nansen Legacy Transect from 76°N to 80.3°N (left to right). Black dots correspond to sampling points. Notice the different scale for each year at the bottom of each plot.

depth on the P1 station in August 2019. As described also later in the results, this particular hotspot of O coincided with high particulate silicate concentration, chlorophyll *a* maximum and high nanophytoplankton abundance.

Sodium, Chlorine, Potassium

Particulate Na and Cl showed similar distribution along the research transect, with some locations of high concentrations (2018: P1-150m and P2-120m, 2019: P2-10m) (Figure 9 & Figure 10). The concentration of particulate K ranged between 0.002±0.001 µM - 0.149±0.040 µM in August 2018 and 0.006±0.001 µM – 0.094±0.003 µM in August 2019, with the highest concentrations registered below 100 m depth in the study area for both years (Figure 11).

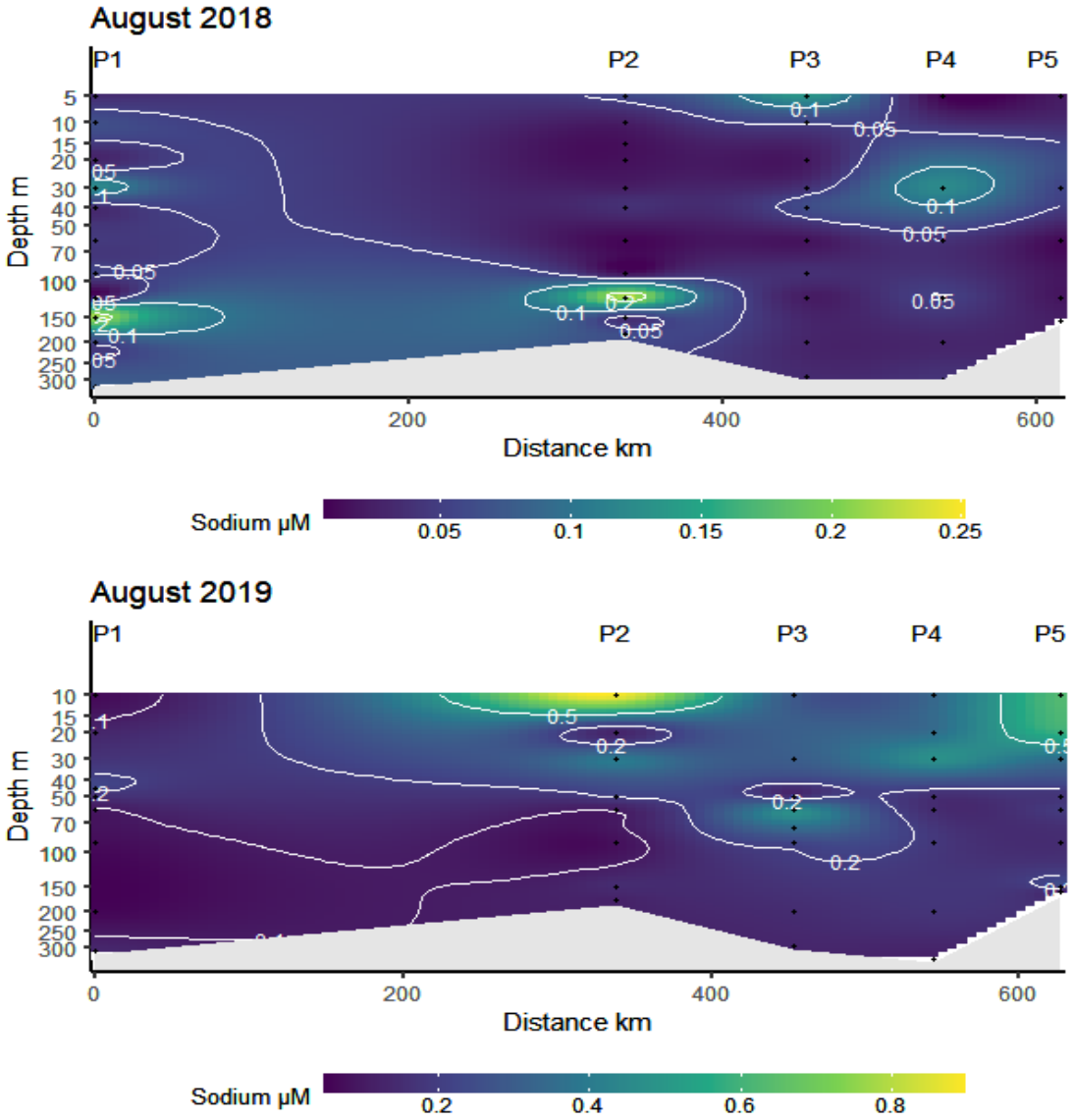

Figure 9. Distribution of particulate Na in µM during August 2018 and August 2019 for all five stations of the Nansen Legacy Transect from 76°N to 80.3°N (left to right). Black dots correspond to sampling points.Depth axis in log scale. Notice the different scale for each year at the bottom of each plot.

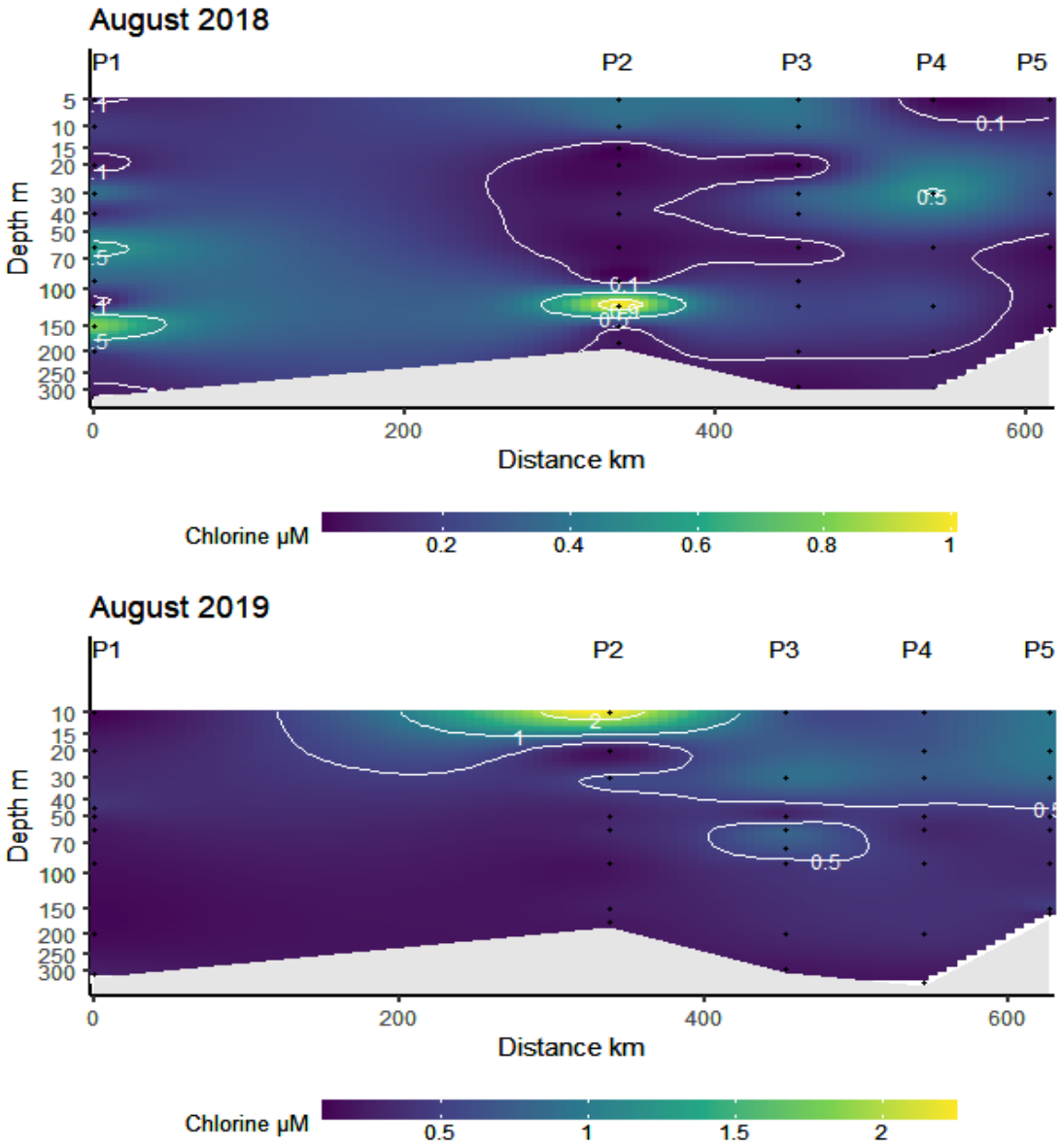

Figure 10. Distribution of particulate Cl in µM during August 2018 and August 2019 for all five stations of the Nansen Legacy Transect from 76°N to 80.3°N (left to right). Black dots correspond to sampling points. Depth axis in log scale. Notice the different scale for each year at the bottom of each plot.

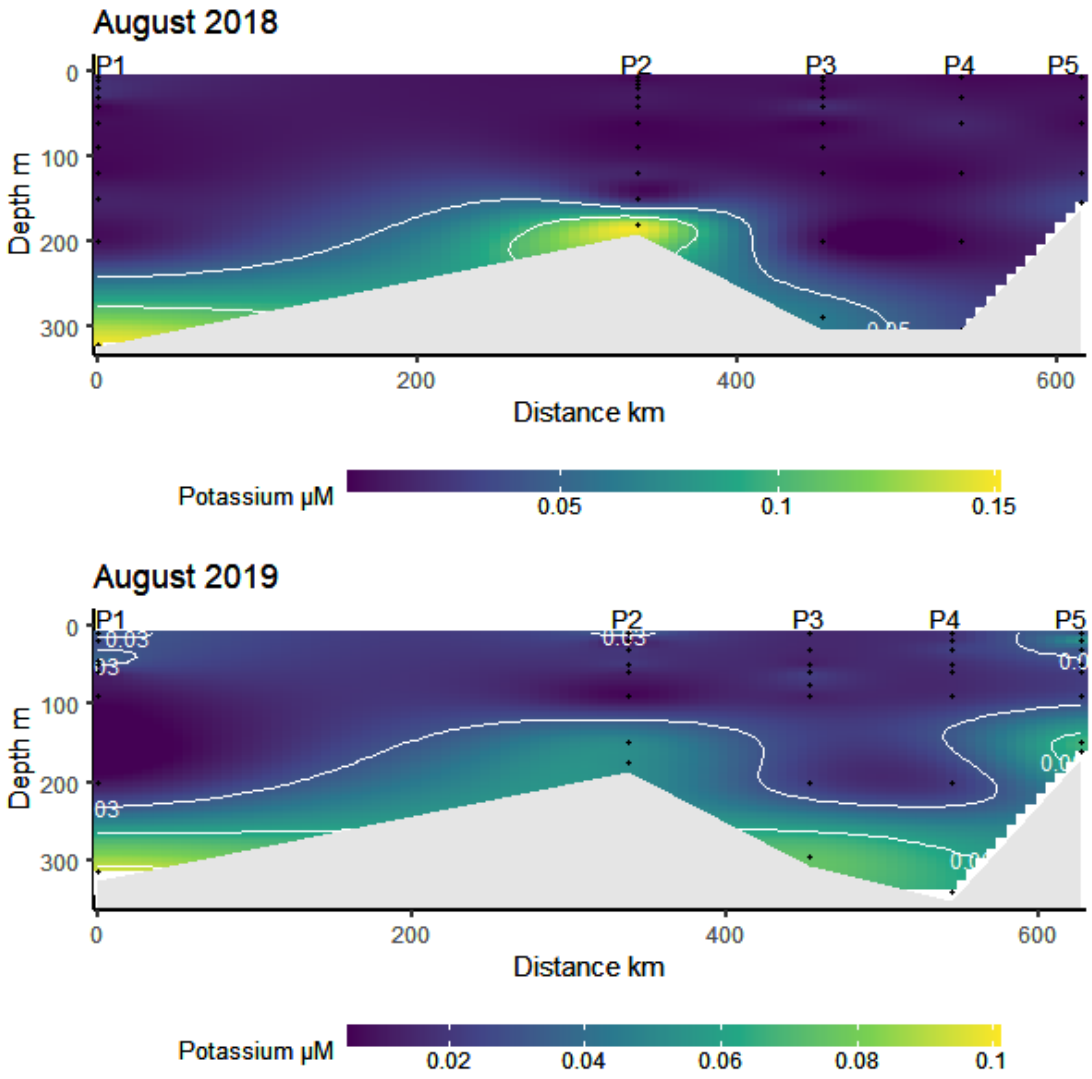

Figure 11. Distribution of particulate K in µM during August 2018 and August 2019 for all five stations of the Nansen Legacy Transect from 76°N to 80.3°N (left to right). Black dots correspond to sampling points. Depth axis in log scale. Notice the different scale for each year at the bottom of each plot.

Magnesium

Particulate Mg varied significantly between the two summers in terms of concentration (Welch's ANOVA: F=61.5, p<0.001) and distribution in the water column (Figure 12). More detailed, in 2018 concentrations varied between 0.007±0.001 µM – 0.065±0.008 µM with highest values 0.171±0.053 µM at P1 322m and 0.140±0.015 µM at P2 181m. On the contrary, in 2019 Mg seemed to be more abundant on the surface layers of P2 (10m : 0.168±0.070 µM) and P5 (10m & 20m : 0.124±0.010 µM).

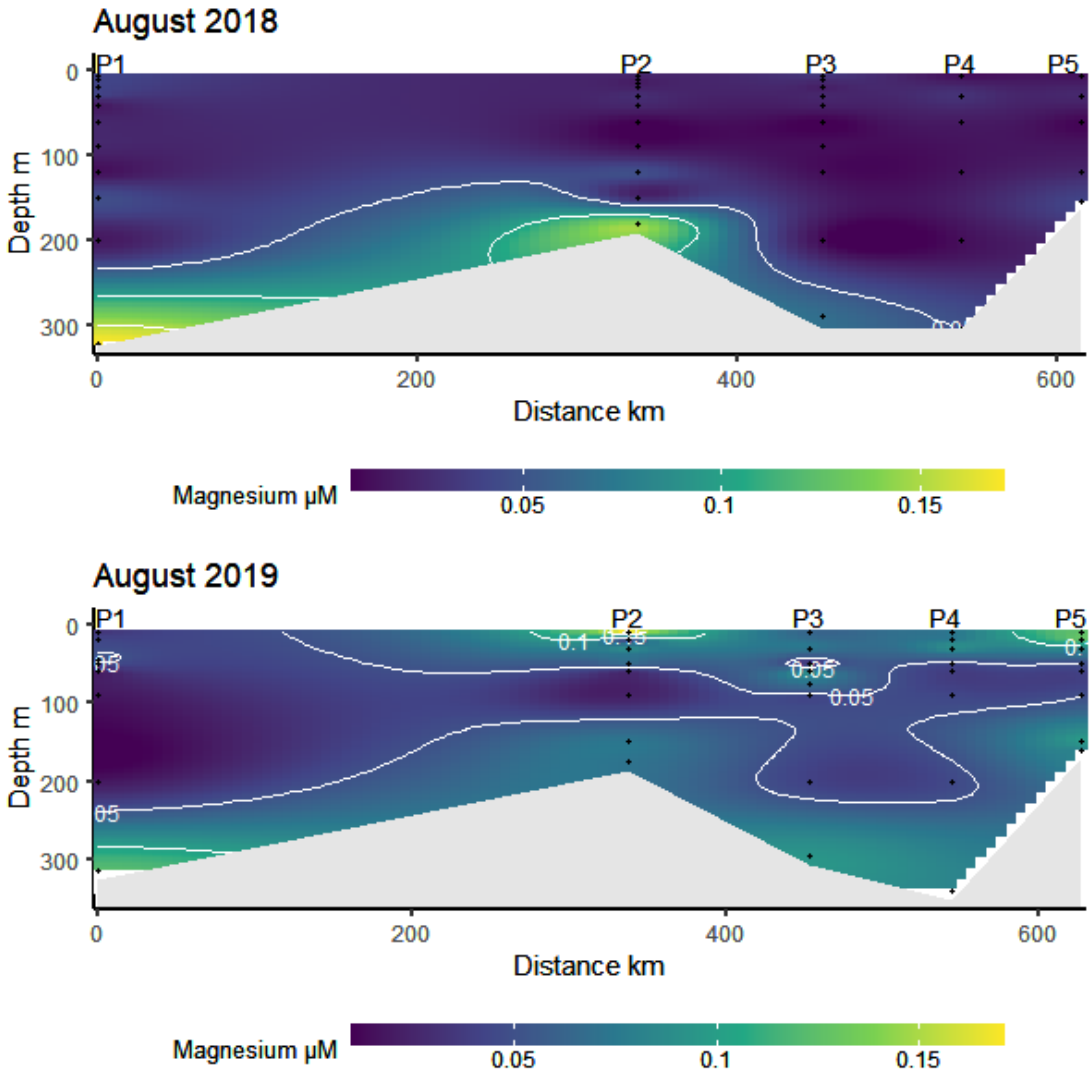

Figure 12. Distribution of particulate Mg in µM during August 2018 and August 2019 for all five stations of the Nansen Legacy Transect from 76°N to 80.3°N (left to right). Black dots correspond to sampling points. Notice the different scale for each year at the bottom of each plot.

Calcium

Concentrations of particulate Ca were significantly higher in August 2018 (2018: 0.007 ±0.003 µM – 0.244±0.041 µM; 2019: 0.011±0.001 µM - 0.079±0.059 µM; Welch's ANOVA: F=4.6, p=0.03). As illustrated in Figure 13, the distribution of Ca between the two summers was disparate. During the August of 2018, there were two primary areas with high concentrations both found at the southernmost station (P1 30m and 60m) with the concentration decreasing northwards along the transect. Contrarily in 2019, high concentrations were documented on the bottom and surface of P1, which expanded across the top water layer until station P2, and most distinctly at 30 m depth at the P3 station.

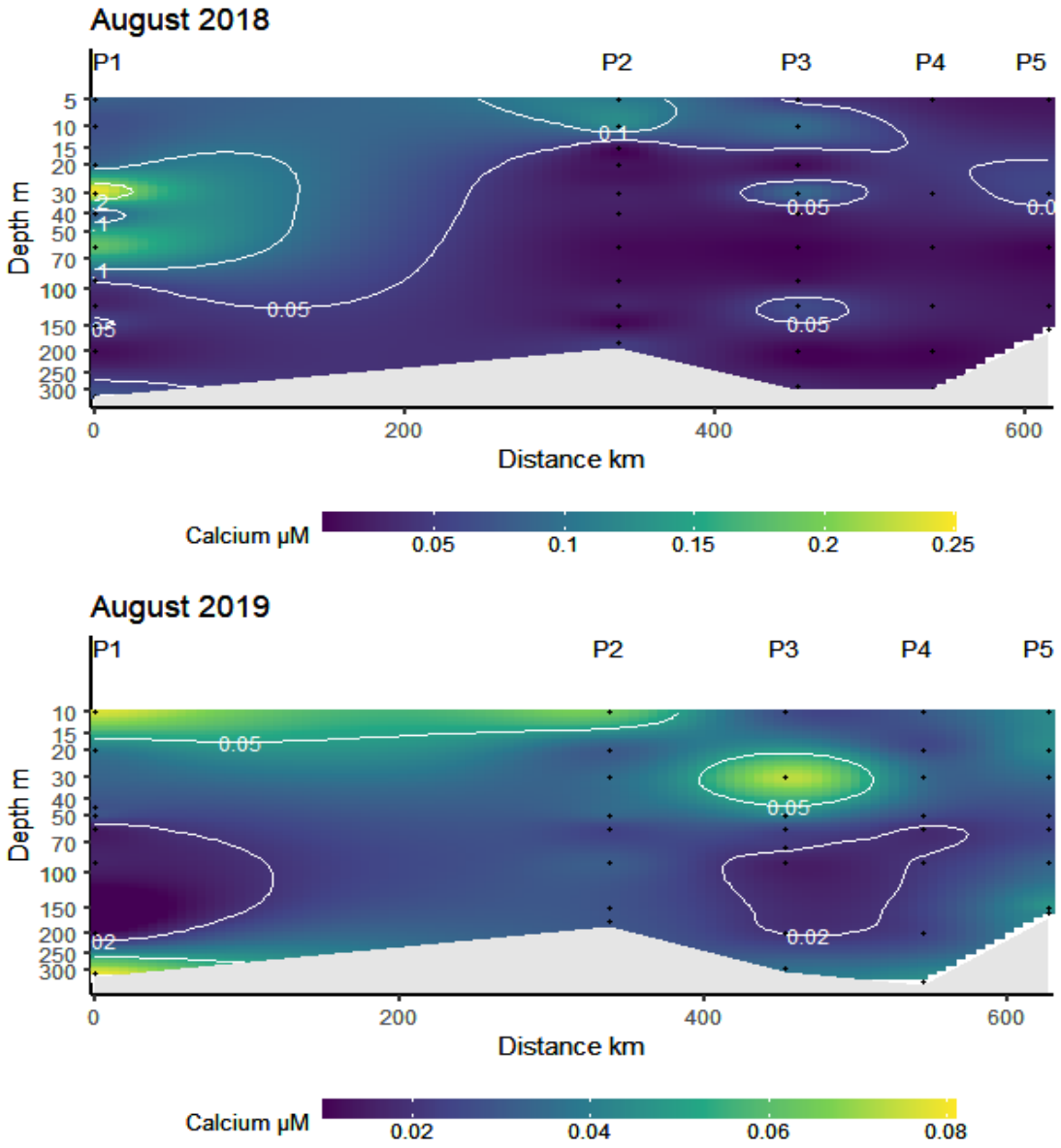

Figure 13. Distribution of particulate Ca in µM during August 2018 and August 2019 for all five stations of the Nansen Legacy Transect from 76°N to 80.3°N (left to right). Black dots correspond to sampling points. Depth axis is in log scale. Notice the different scales for each year at the bottom of each plot.

Silicon

In August 2018 particulate Si varied between 0.009±0.005 µM – 0.585±0.069 µM, with the two highest values reaching 1.484±0.104 µM and 1.593±0.382 µM at P2 181 m and P1 322 m depth, respectively. In 2019, high concentrations were also observed near the surface layers (P1-50m: 0.91±0.056 µM, P5-10m: 0.477±0.028 µM) as well as near the bottom (P1-315m: 0.952±0.038 µM, P3-295m: 0.693± 0.054 µM)(Figure 14).

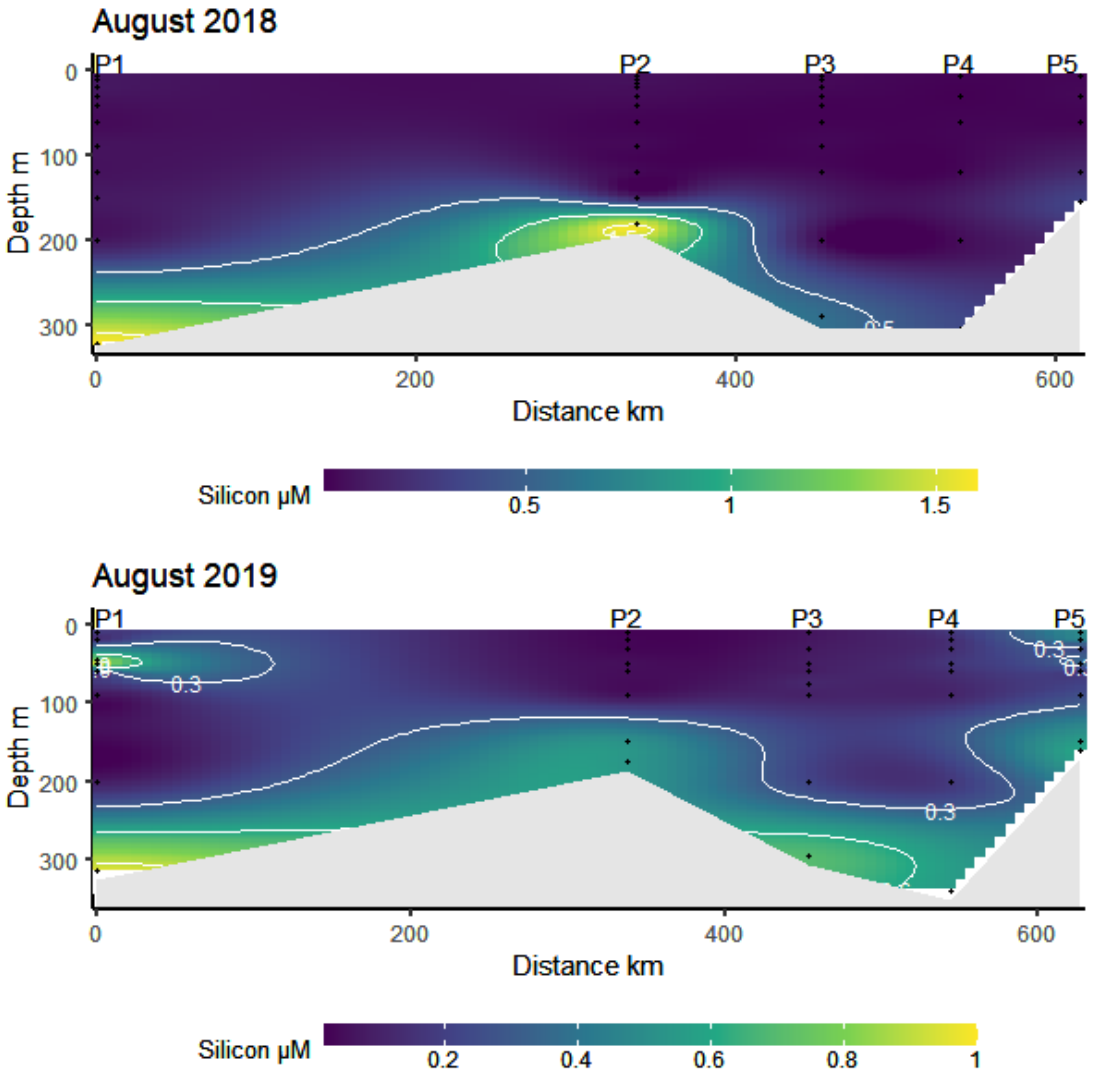

Figure 14. Distribution of particulate Si in µM during August 2018 (top), and August 2019 (down) for all five stations (depicted as vertical dotted lines) of the Nansen Legacy Transect from 76°N to 80.3°N (left to right). Notice the different scales for each year at the bottom of each plot.

Iron

The highest values for particulate Fe through the whole transect for both years were documented in the deepest samples (below 100m the concentration of particulate Fe was one order of magnitude higher compared to the concentration in the top 100m in all stations in both years). The concentration fluctuated from 0.002±0.000 µM to 0.334±0.024 µM (P2-181m) in 2018 and from 0.003±0.002 µM to 0.223±0.009 µM (P1-315m) in 2019. Interestingly, in 2019 particulate Fe marked a descending trend in a northward direction (Figure 15).

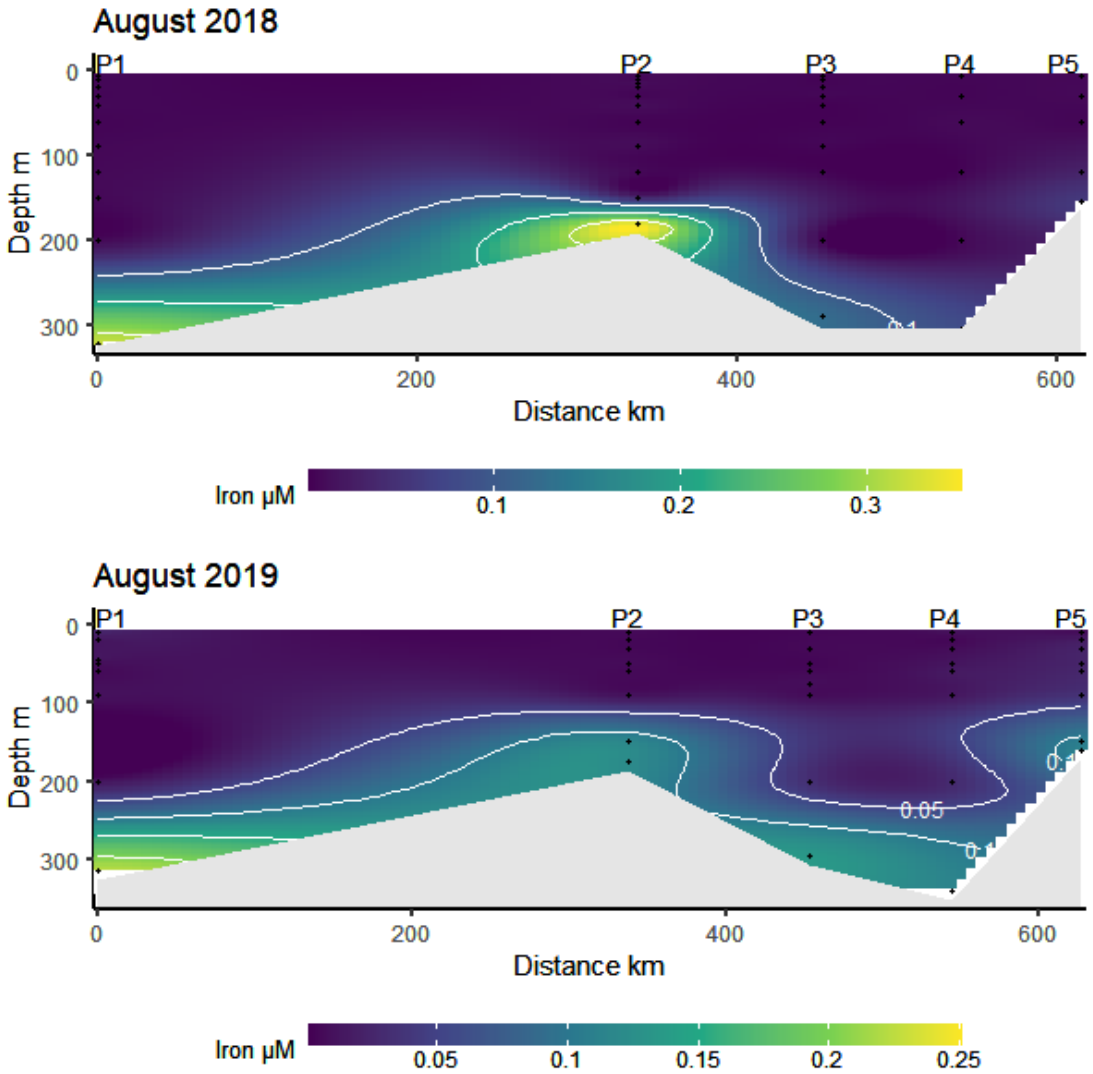

Figure 15. Distribution of particulate Fe in µM during August 2018 (top), and August 2019 (down) for all five stations (depicted as vertical dotted lines) of the Nansen Legacy Transect from 76°N to 80.3°N (left to right). Notice the different scales for each year at the bottom of each plot.

Manganese

Mn was detected mainly in deep samples (Figure 16) especially the first study period (2018: <60m) with maximum value found near the bottom of the P4 station (304m: 0.054±0.005 µM). A slightly different distribution of particulate Mn was illustrated in 2019 where the highest concentration was documented at P2-150m (0.064±0.002 µM) and Mn was detected even up to 10m depth (0.001 µM).

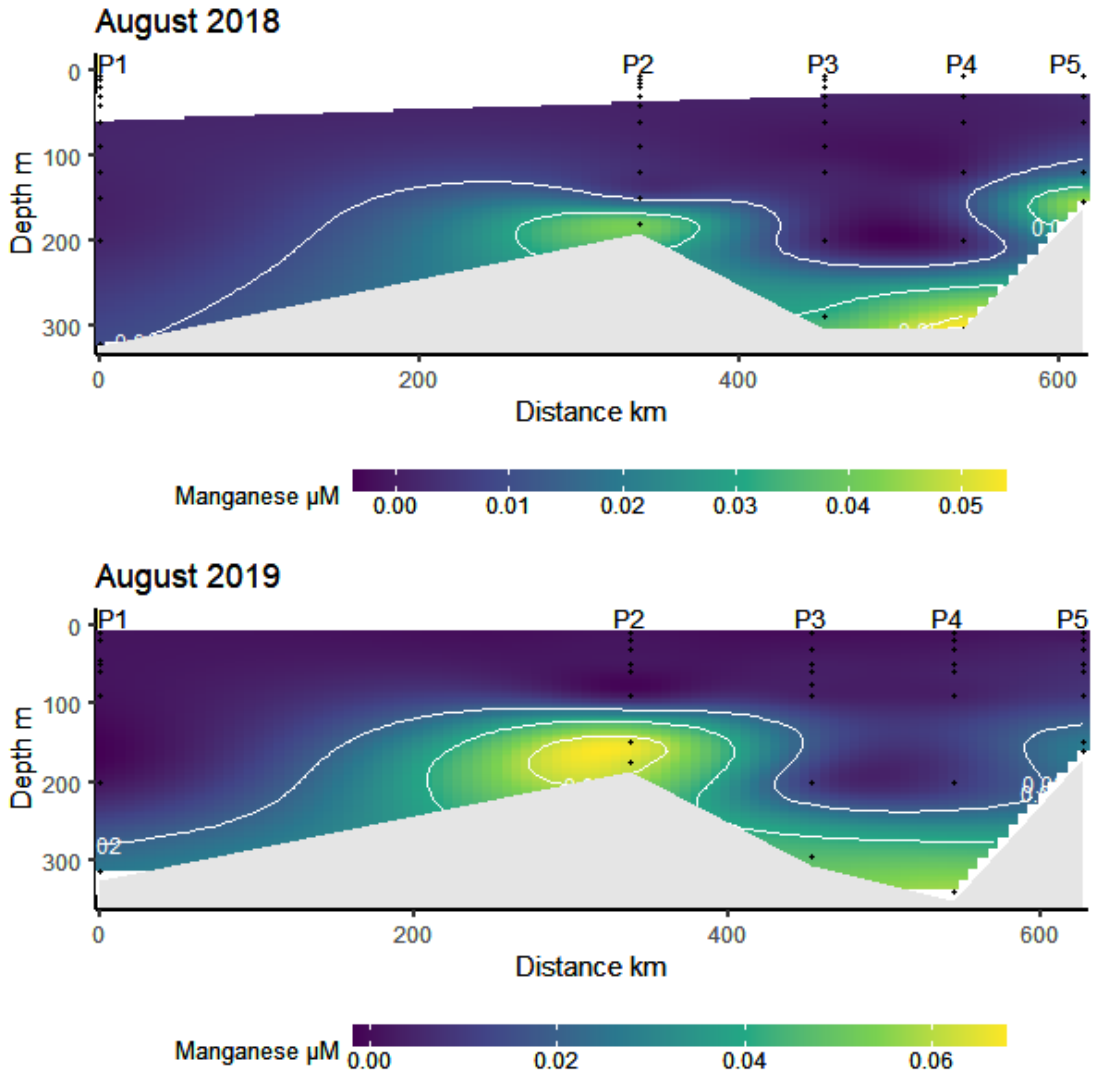

Figure 16. Distribution of particulate Mn in µM during August 2018 (top), and August 2019 (down) for all five stations (depicted as vertical dotted lines) of the Nansen Legacy Transect from 76°N to 80.3°N (left to right). Notice the different scale for each year at the right side of each plot.

Copper, Zinc

Out of all samples in approximately 91.7% and 89.5% of the particulate Cu or Zn was under the detection limits of the instrument. Precisely, Zn was only recorded in less than 15 samples from August 2018. Therefore, it is hard to describe the distribution of these two trace metals. For that reason, Cu and Zn will not be analyzed further. In general values ranged between 0.001 µM – 0.003 µM and 0.001 µM – 0.007 µM for Cu and Zn respectively.

3.3. Elemental correlations and stoichiometry

A series of Pearson's correlation tests revealed highly significant elemental relationships. In 2018 the strongest correlations were found between Si-Fe, Si-K, Fe-K, Mg-K, O-K, O-Si, O-Mg, Si-Mg, O-Fe, Fe-Mg, P-S, Na-Cl, Ca-S, Mn-K in descending order of the correlation coefficient (Appendix 6.2, Table 6). Of all elements that were counted, O, Si, Fe, Mn, K, and Mg were the only ones that correlated positively with the depth that year, Ca, P, and S correlated with temperature while only the two latter ones showed a significant positive relationship with chlorophyll a (Appendix 6.2, Table 4). In 2019, contrariwise, the significant correlations registered between elements were O-Si, Na-Cl, Fe-K, Na-S, O-K, Si-K, Fe-Mn, Na-Mg, P-S, S-Cl, O-Fe, Mg-Cl, Fe-Si, Mn-Si, Mn-K, Mn-O, Mg-S, Mg-K, Na-P, Mg-Ca, Ca-K, P-Mg, O-Mg, O-Ca (Appendix 6.2, Table 9). Interestingly, that year it was P,S, Na, Mg and Cl that correlated positively with chlorophyll a (Appendix 6.2, Table 8). P normalized quotas are widely applied by marine researchers because they provide a convenient comparison of plankton samples irrespective of cell volumes. The average elemental ratios measured for both years are presented in Figure 17 expressed as P quotas (mol/mol). Based on average values of the elements, the following stoichiometric relationship was obtained for the two years, by normalizing to P concentration:

- August 2018: $O_{4.9}Si_{2.99}Cl_{6.76}P_1Na_{1.47}Ca_{1.16}Mg_{0.69}Fe_{0.51}K_{0.33}S_{0.32}Mn_{0.38}$
- August 2019: $O_{8.84}Si_{5.9}Cl_{9.51}P_1Na_{4.37}Ca_{0.72}Mg_{1.31}Fe_{0.84}K_{0.64}S_{0.41}Mn_{0.38}$

In general, all elemental quotas were higher in 2019 with the exception of Ca:P, however only S, O, Na, K, Mg, and Si quotas were found to be statistically higher in 2019 than in 2018. More elemental quotas are available at Appendix 6.3.

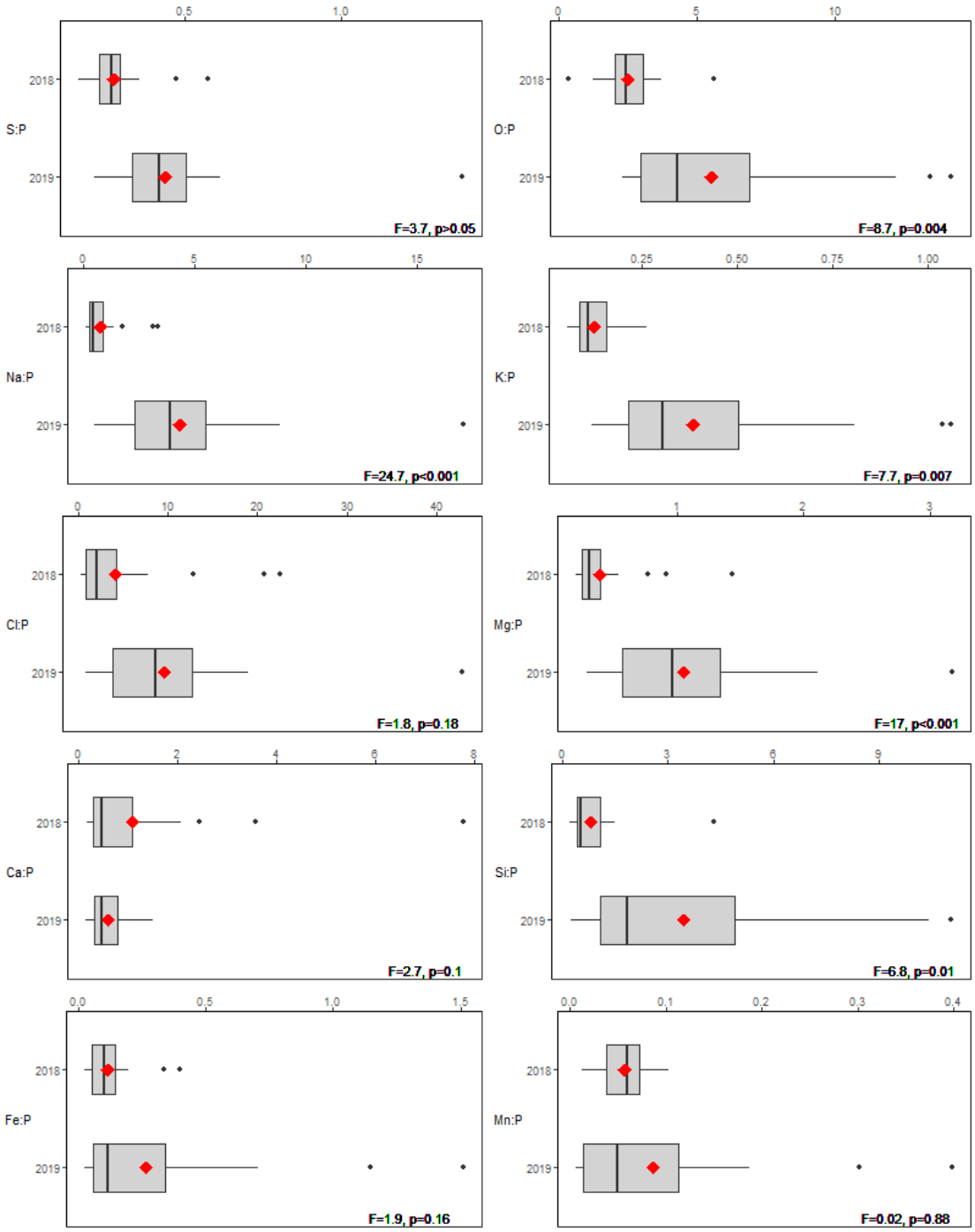

Figure 17. Box and whisker graphs of individual elemental quotas from all samples per year. All quotas are normalized to P concentration and the units are mol/mol. The two ends of each box represent the 25th and 75th percentiles of all data points. The solid lines in each box represent the medians and the red diamonds correspond to the mean of each group. The two ends of each bar represent the 10th and 90th percentiles for all data points. Outliers are plotted as black dots. In each plot, the results of Welch's ANOVA are presented in the bottom right part (F statistic and p-value), which compares the mean quotas per year.

3.4. Chlorophyll *a* and microbial abundances

Chlorophyll *a* concentrations were significantly higher in August 2019 (0.025 µg L^{-1} – 2.573 µg L^{-1}) compared to 2018 (0.003 µg L^{-1} – 0.419 µg L^{-1}) (Welch's ANOVA: F=17.4, p<0.001) (Figure 18). The first year chla maxima were recorded between 5 and 40 m depth with the highest at the first station at 5m (P1-5m: 0.419 µg L^{-1}; P2-40m: 0.380 µg L^{-1}; P3-30m: 0.26 µg L^{-1}; P4-30m: 0.034 µg L^{-1}; P5-30m: 0.214 µg L^{-1}) and the second year between 20 and 60 m depth with the highest at 20m of P5 station (P1-45m: 1.218 µg L^{-1}; P2-50m: 1.178 µg L^{-1}; P3-60m: 0.582 µg L^{-1}; P4-30m: 1.366 µg L^{-1}; P5-20m: 2.573 µg L^{-1})(Figure 15).

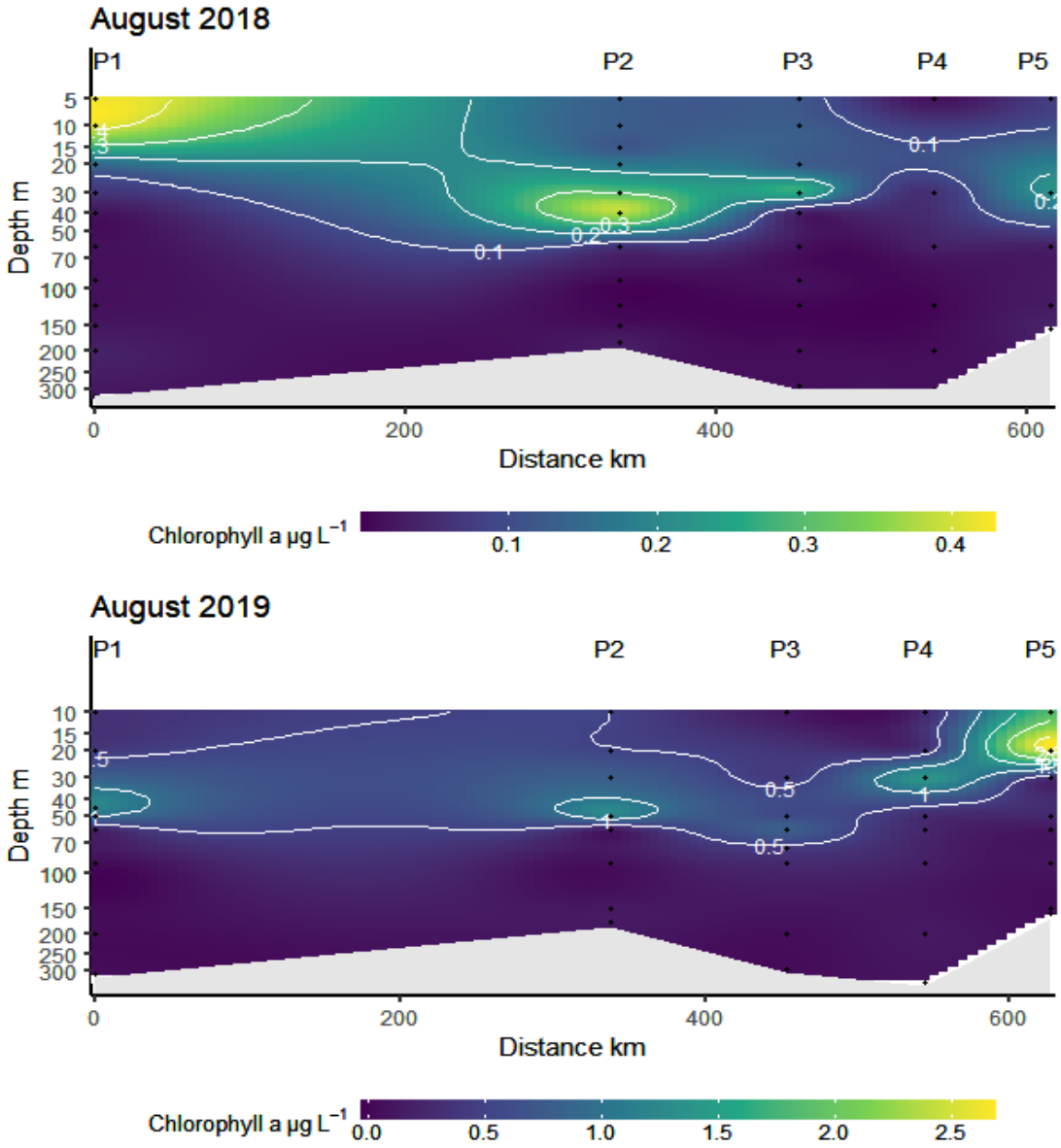

Figure 18. Distribution of chlorophyll a in µg·L^{-1} during August 2018 and August 2019 for all five stations of the Nansen Legacy Transect from 76°N to 80.3°N (left to right). Black dots correspond to sampling points. Depth axis in log scale. Notice the different scale for each year at the bottom of each plot.

Nanophytoplankton abundance was significantly higher in 2019 (2018: 1-2812 cells mL $^{-1}$; 2019: 17-3162 cells mL $^{-1}$; Welch's ANOVA: F=11.4, p=0.001). Greater abundances were in general found above 60 m depth in all stations both years, and the peaks in abundance were located at the same localities with the chlorophyll *a* maxima +/- 10m (Figure 19). This fact is additionally supported by the strong correlation between these two variables (a=0.707, p<0.001).

The abundance of picophytoplankton illustrated also in Figure 19, followed very interesting patterns along the study transect. Comparing between the two study periods, their abundance was slight higher in August 2018 and correlated with chlorophyll *a* (a=0.31, p<0.05). That same year (2018) their abunance varied between 0-12409 cells mL $^{-1}$, and the highest ones were located at stations P4-5m (12409 cells mL $^{-1}$), P4-30m (11410 cells mL $^{-1}$) and P5-30m (10443 cells mL $^{-1}$). The next year (2019), their abundance ranged between 0-7660 cells mL $^{-1}$, and the greater values were located at P3-10m (7600 cells mL $^{-1}$) and P4-10m (7433 cells mL $^{-1}$).

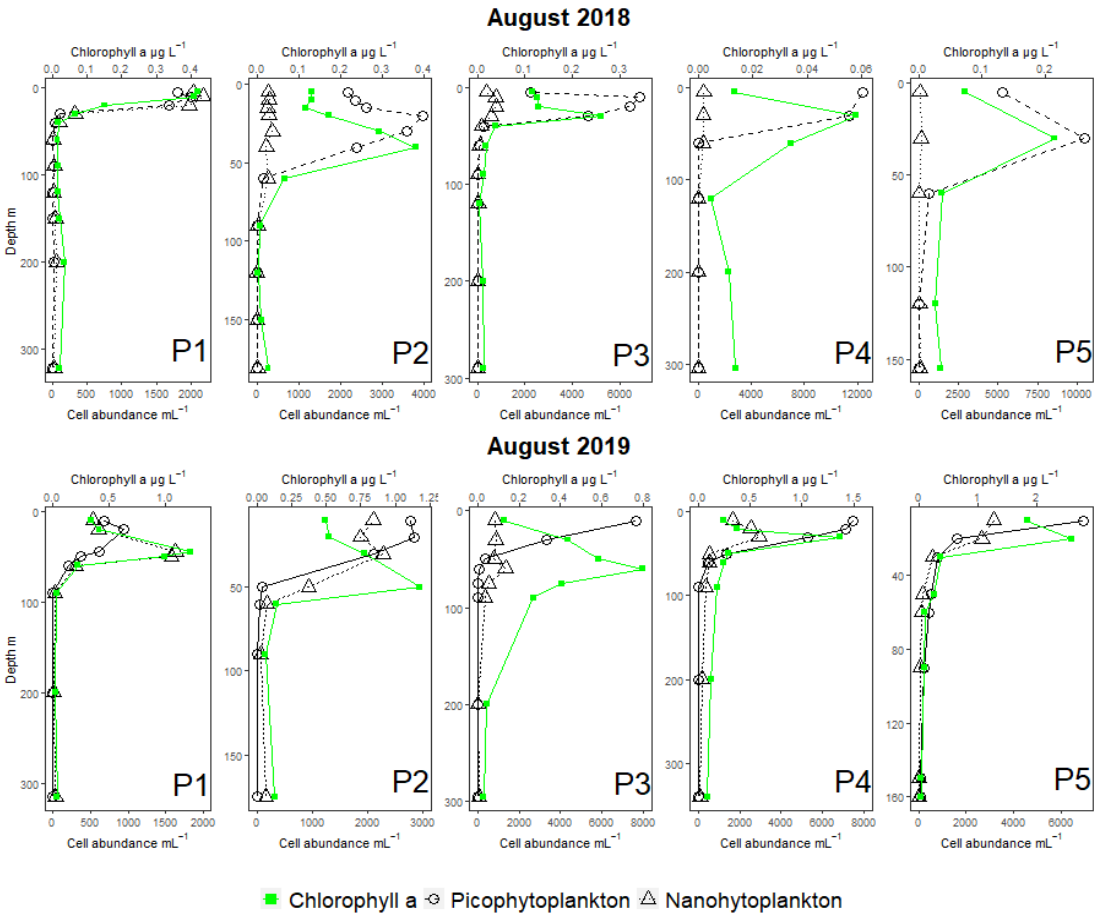

Figure 19. Depth profiles of cell abundances (cells per mL) of Picophytoplankton and Nanophytoplankton plotted together with chlorophyll a (green) profiles, per station per year. Notice the different scales both for the abundances and the chlorophyll a concentration (µg L^{+1}).

Heterotrophic nanoflagellate abundance fluctuated between 23-1377 cells mL $^{-1}$ and 69-1121 cells mL $^{-1}$ in 2018 and 2019 respectively. Bacterial abundance, was significantly higher in 2019 (2018: 60388 -801505 cells mL $^{-1}$; 2019: 156840-2249348 cells mL $^{-1}$; Welch's ANOVA: F=12.8, p=0.001). Higher bacterial abundances were observed generally above 100m depth but in some exceptions there were high abundances observed also in deeper parts of the study area (e.g. at P2 (2018) and at P1 (2019), Figure 20).

Pearson's correlation tests revealed strong positively correlations between Nanophytoplankton and O, P, S, Si, K, and Mg and some correlation between Bacteria and P, S, Na and Mg in 2018 (Appendix 6.2, Table 5). Noteworthy were also the significant correlations registered between all microbial groups and P, S, Mg and Na in 2019 (Appendix 6.2, Table 8).

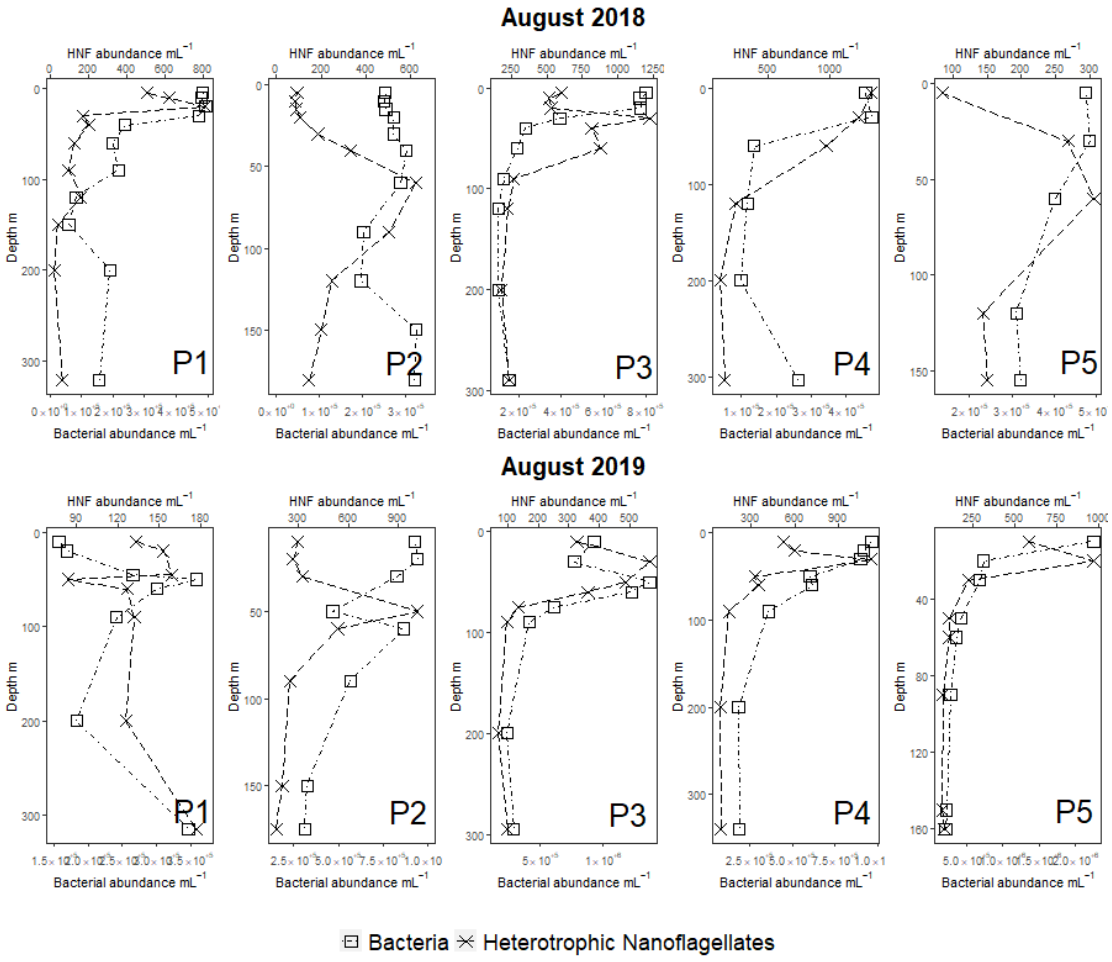

Figure 20. Depth profiles of cell abundances (cells per mL) of Heterotrophic Nanoflagellates and Bacteria per station per year. Notice the different scales for each group on each plot.

3.5. Canonical correspondence analysis

The canonical correspondence analysis (CCA) was carried out to assess the degree to which the microbial community abundances were associated with the concentrations of elements in the PM during the two summers with different ice coverage. The results of CCA highlighted a different patterns throughout the study area between the August 2018 and August 2019 (Figure 21)(Appendix 6.2, Table 10 - Table 19). For both years, however, there is a clear grouping of deeper and shallower samples, in the left and right part of the first CCA axes, respectively.

For August 2018, the first two axes (ANOVA, $p<0.05$) of the CCA accounted for 83.94% of the variability within the dataset. Axis 1 (Eigenvalue: 0.04, proportion explained 69.96%, ANOVA: $p<0.001$) opposed Nanophytoplankton, Picophytoplankton and chlorophyll *a* by a dominance of mainly P and S and in a lesser degree Temperature, O, Ca, and Mg mostly in lower depths to HNF and Bacteria who were projected on the other side of Axis 1. Axis 2 (Eigenvalue: 0.004, proportion explained 8.49%, ANOVA: $p<0.05$), generally opposed surface from bottom samples with a strong projection of bottom samples near the concentrations of Fe, Si and Mn which is very distinctive in the lower right part of the top plot in Figure 21. On Axis 2 additionally, chlorophyll a was projected nearer to Picophytoplankton in the samples of August 2018.

Contrariwise, for August 2019 the total explained variance of the data by the model was ~73.54%, with Axis 1 (Eigenvalue: 0.018, ANOVA: $p<0.001$) accounted for 61.13% of that explained variance and Axis 2 (Eigenvalue: 0.003, ANOVA: p=-0.196) 9.87%, however only Axis 1 was proven statistically significant to describe the variance of the data. On this case, only the terms P, S, Ca, Mg, and Sal were found significant for the model, however all parameters are illustrated in the biplot as it is biologically sensible to include them in the model. Nanophytoplankton and chlorophyll *a* were closely projected to one another on Axis 1 together with Picophytoplankton by dominance of P and S in surface samples compared to HNF and Bacteria found on the opposite side of Axis 1 together with Sal, Mg and Ca (Figure 21, bottom plot).

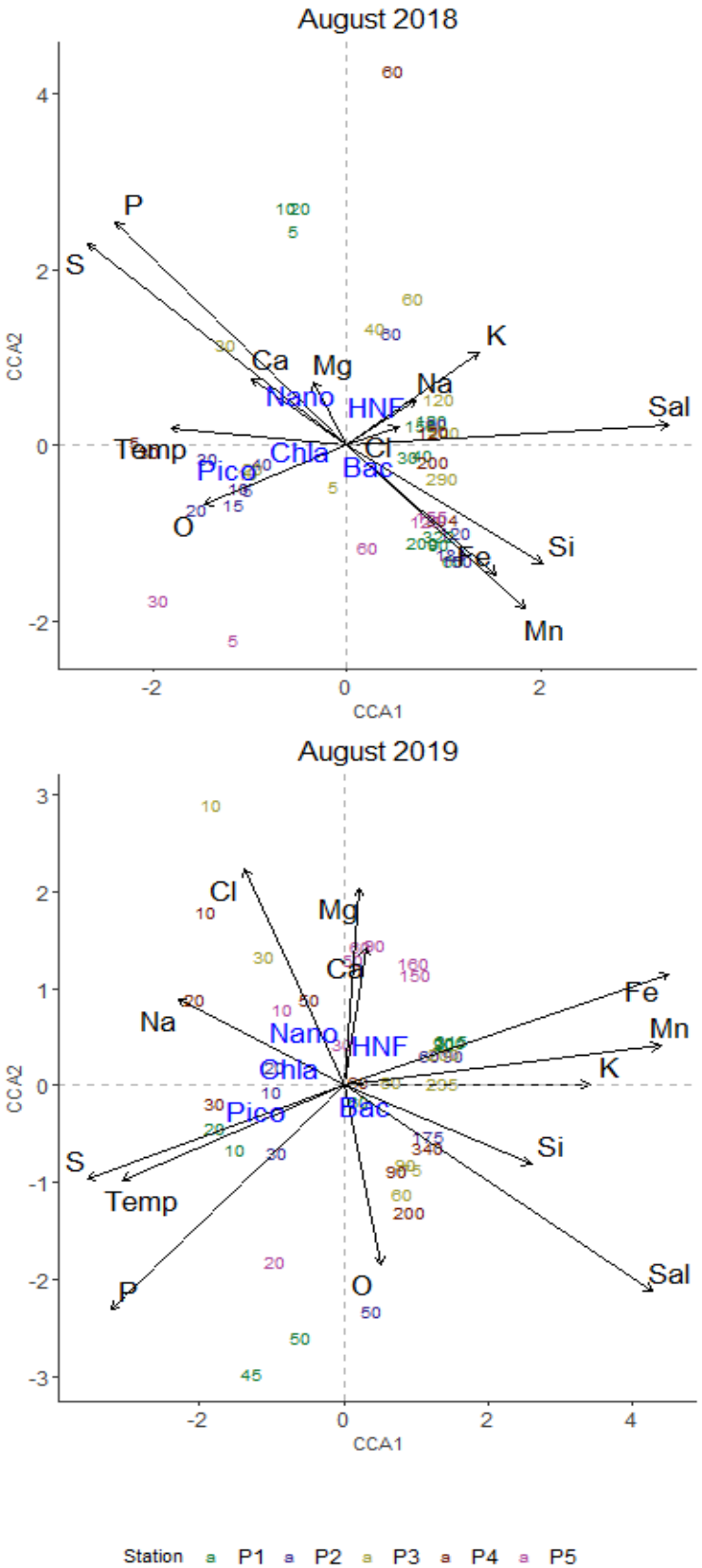

Figure 21. Projection of samples, main microbial groups (Chla=chlorophyll a, Nano=Nanophytoplankton, Pico=Picophytoplankton, HNF=Heterothrophic Nanoflagellates, Bac=Bacteria) and biogeochemical factors (particulate elemental concentrations, Temp=Temperature and Sal=Salinity) on the first two axes of the canonical correspondence analysis (CCA) for each year. Vectors point in the direction of an increase in the magnitude of the respective element concentration. Numbers indicate the sampling depth, and each color corresponds to each sampling station.

3.6. Identification of microbial organisms

Upon describing the distribution of particulate elemental concentrations and observing the profiles of chlorophyll *a* and microbial abundances, a total of 12 samples were observed under the Scanning Electron Microscope as an effort to document the types of particles of biogenic and/or lithogenic sources in an effort to uncover the differences between the two years with contrasting environmental conditions and the origins of these particles. A list with the samples is available in Table 1.

Table 1. List of samples chosen for observation under the Scanning Electron Microscope.

August 2018		August 2019	
Station	Sampling Depth	Station	Sampling Depth
P1	10m	P1	50m
P1	30m	P1	315m
P1	322m	P2	10m
P2	40m	P2	181m
P2	181m	P3	20 m
P5	30m	P5	15 m

The sample at station P1 10 m depth was chosen due to the high concentrations of P, S , Ca and O recorded in combination to maximum abundances of Nanophytoplankton, Picophytoplankton, Bacteria and high picophytoplankton abundance. Additionally, that locality had remarkably high temperature and salinity values. As depicted in Figure 22, a couple of small diatom species were present in that area e.g., *Thalassiosira* sp. P.T. Cleve, 1873 emend. Hasle, 1973 and *Nitzschia longissima* (Bréb. in Kütz.) Ralfs in A.Pritch. In the group of coccolithophores, *Emiliania huxleyi* (Lohmann) Hay & Mohler and *Coccolithus pelagicus* (Wallich) J.Schiller, 1930 were documented. Finally, among other groups (Figure 23), the presence of the species *Phalacroma rotundatum* (Claparéde & Lachmann) Kofoid & J.R.Michener, 1911 and *Dinophysis norvegica* Claparède & Lachmann, 1859 belonging to the dinoflagellate group was also recorded.

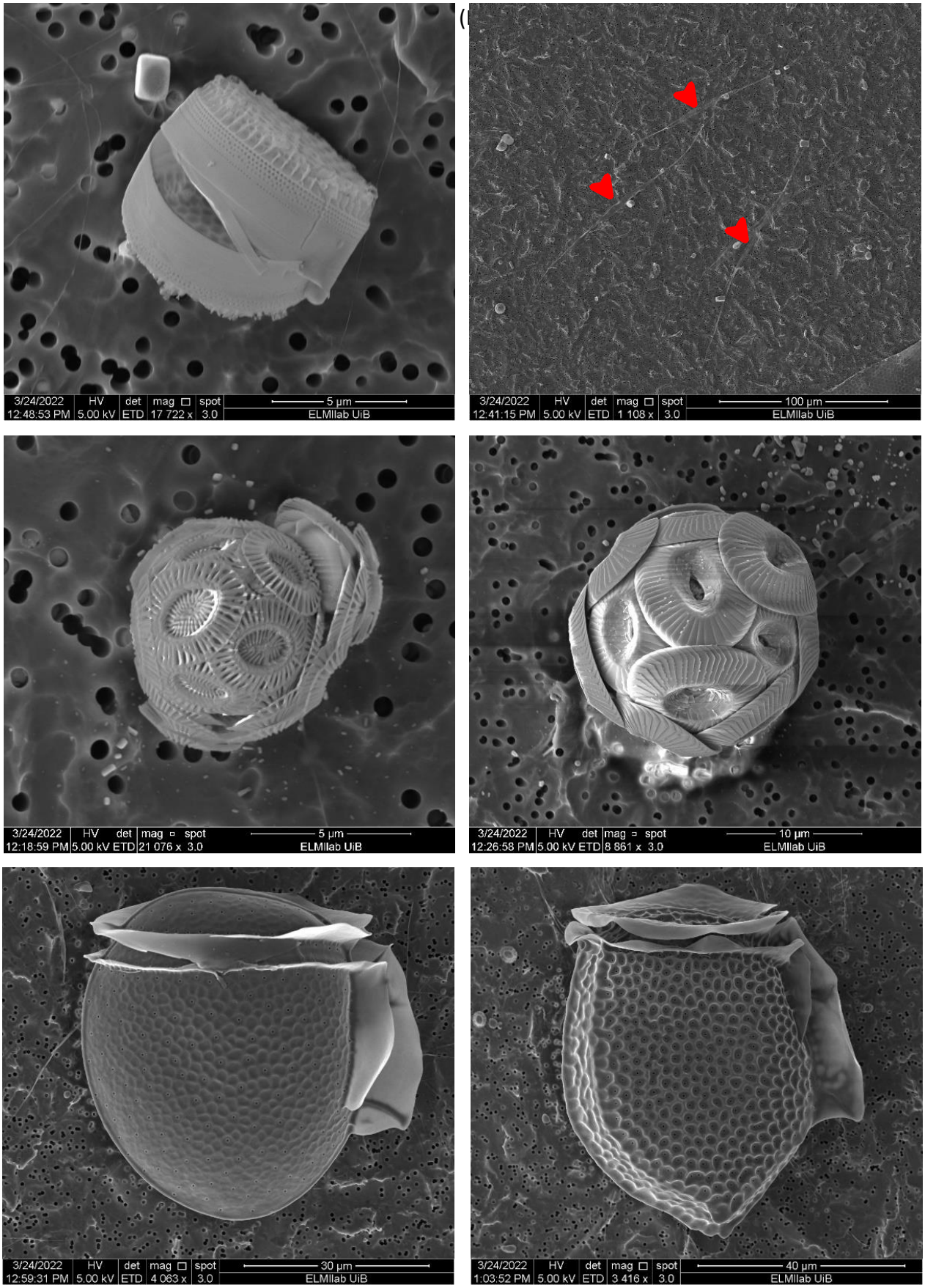

Figure 22. Images from SEM of the sample at P1 depth 10m in August 2018. Top-left: Thalassiosira sp., Top-right: Nitzschia longissima (red arrows pointing at cells), Middle-left: Emiliania huxleyi, Middle-right: Coccolithus pelagicus, Bottom-left: Phalacroma rotundatum, Bottom-right: Dinophysis norvegica.

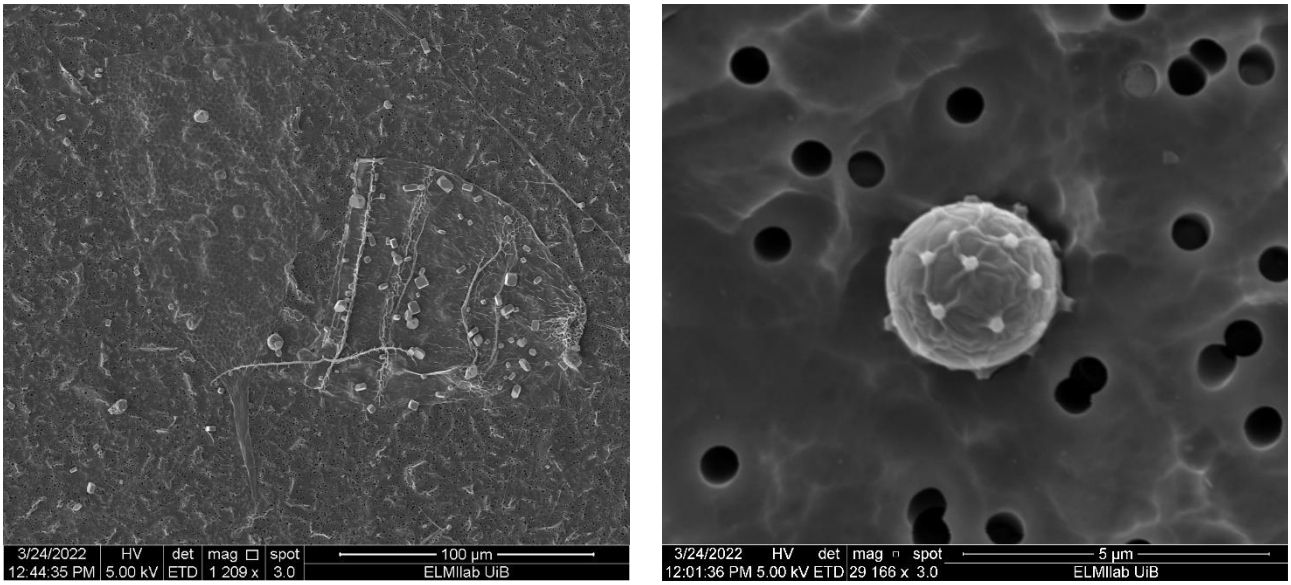

Figure 23. P1 – 10 m, Left: Tintinnids, right: Chrysophyceae stomatocyst.

Because of the high concentration of Ca, P and S at 30 m deep at P1 station this sample was selected as well for observation. Indeed, high number of E. huxleyi were present often forming aggregates, while species like *Thalassiosira* sp., *Chaetoceros* sp. Ehrenberg (1844), and *Protoperidinium* sp. Bergh, 1881 were also found there (Figure 24, Figure 25). At the bottom of station P1 where Si, Fe, Mg, K, and O marked elevated concentrations, mostly diatoms and debris from cell structures were captured. Among the diatoms were, *Rhizosolenia hebetata f. semispina* (Hensen) Gran, 1908 and Thalassiosira sp., and the remains of *Actiniscus pentasterias*, a

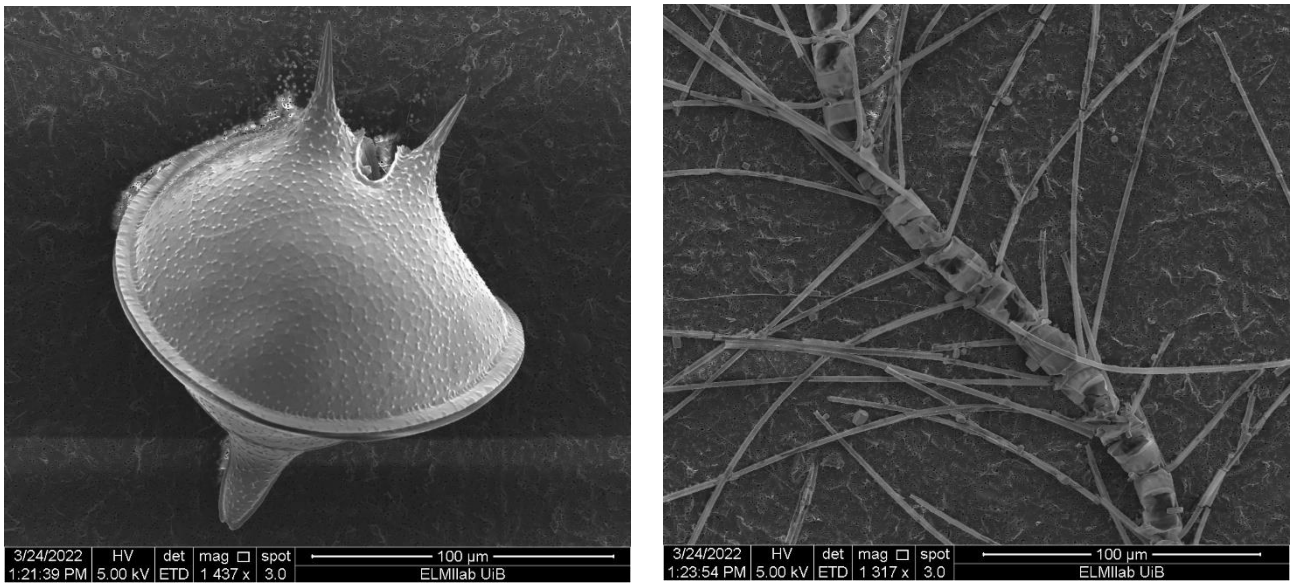

Figure 24. P1 – 30 m, Left: Protoperidinium sp., Right: Chaetoceros sp.

dinoflagellate with siliceous internal skeleton formed of two star-like bodies was also detected in the sample. However, most prominent were aggregates of biological material (e.g., coccoliths and diatom frustules)(Figure 26).

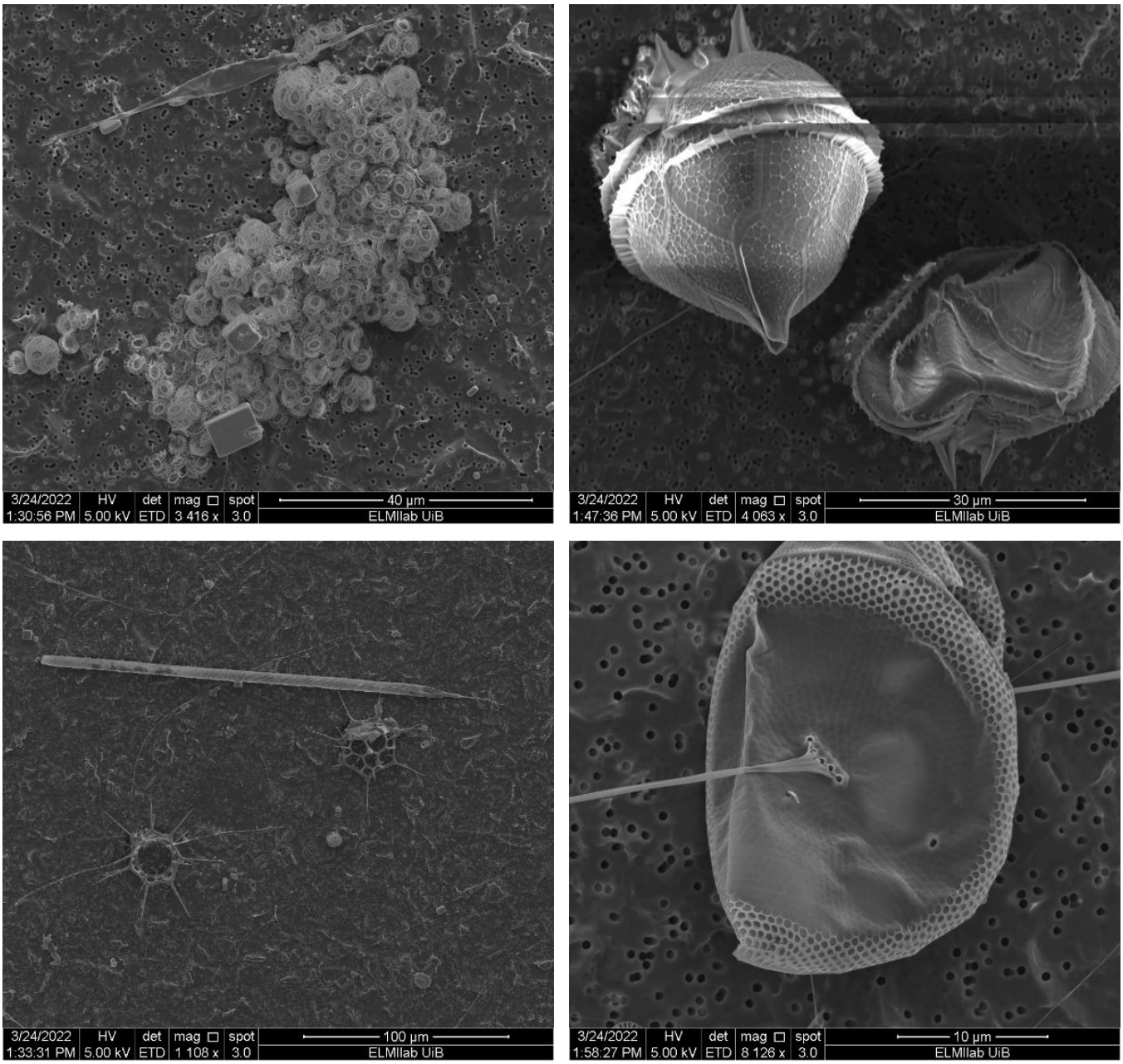

Figure 25. Images from SEM of the sample at P1 depth 30m in August 2018. Top-left: Emiliania huxleyi and Cylindrotheca closterium, Top-right: Protoperidinium sp., Bottom-left: Octactis speculum and Rhizosolenia sp. Bottom-right: Thalassiosira sp.

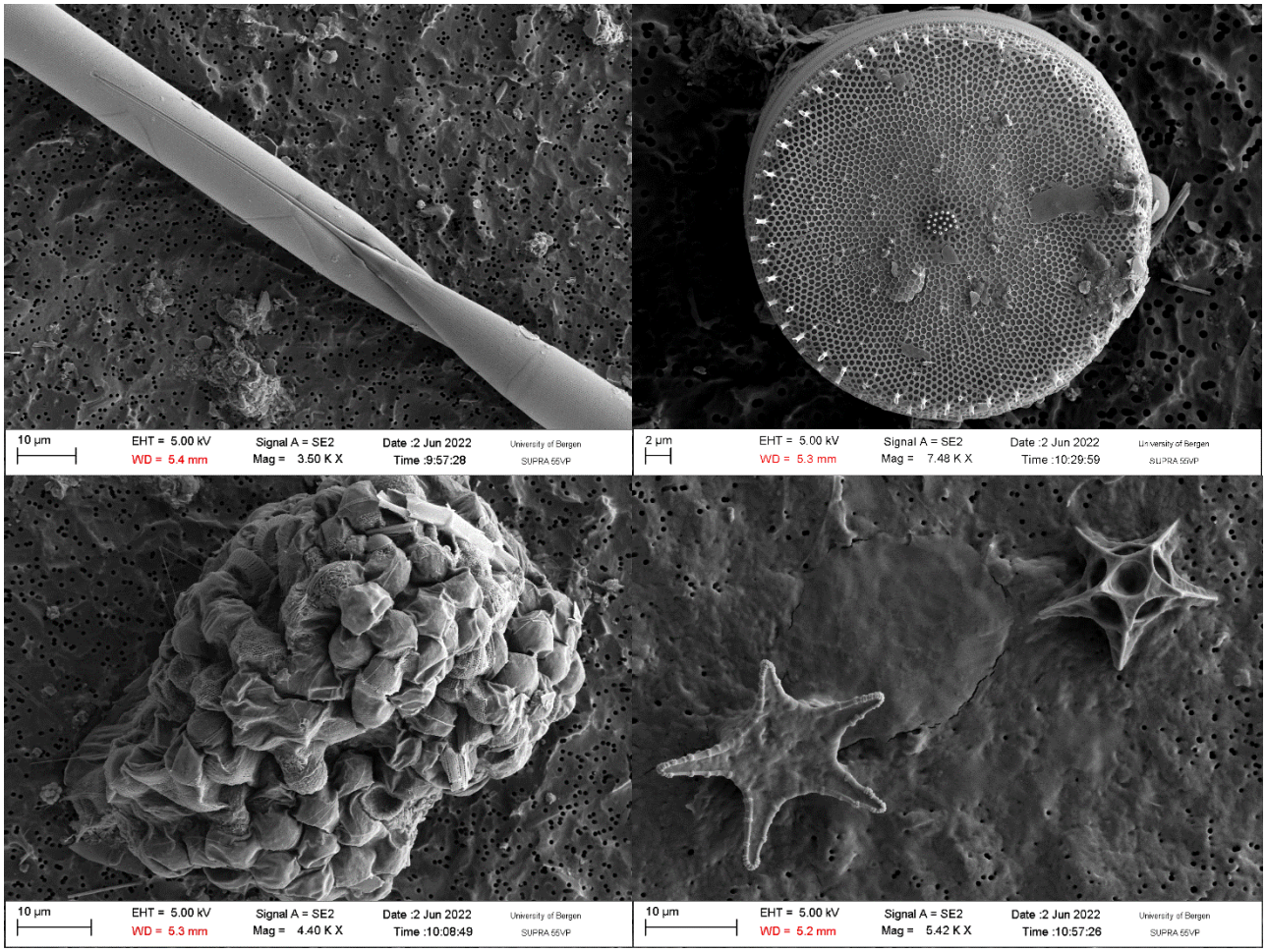

Figure 26. Images from SEM of the sample at P1 depth 322m in August 2018. Top-left: Rhizosolenia hebetata f. semispina, Top-right: Thalassiosira sp., Bottom-left: Mass of biological debris. Bottom-right: Actiniscus pentasterias.

The sample at 40 m P2 stations was chosen due to the high S concentration that coincided with High bacterial abundance and a chlorophyll maximum. The sample had very few specimens on as depicted in Figure 26. The last two samples from that year were from Stations P2 and P5 at 181m and 30m respectively (Figure 27 & Figure 29). The former one was characterized by high Fe, Si, P, O, K, Mg, Mn and the latter one by high Ca, chlorophyll *a* and picophytoplankton. Interestingly, in both samples various Tintinnid ciliate species were found (e.g., *Acanthostomella norvegica* (Daday, 1887), *Parafavella gigantea* (Brandt), Kofoid & Campbell, 1929 , *Parafavella acuta* (Jörgensen, 1901)), with the sample at P2 station having additionally some diatom and dinoflagellate species (*Phalacroma rotundatum*)(Dolan et al., 2017; Jensen & Winding Hansen, 2000; Kršinić, 2018).

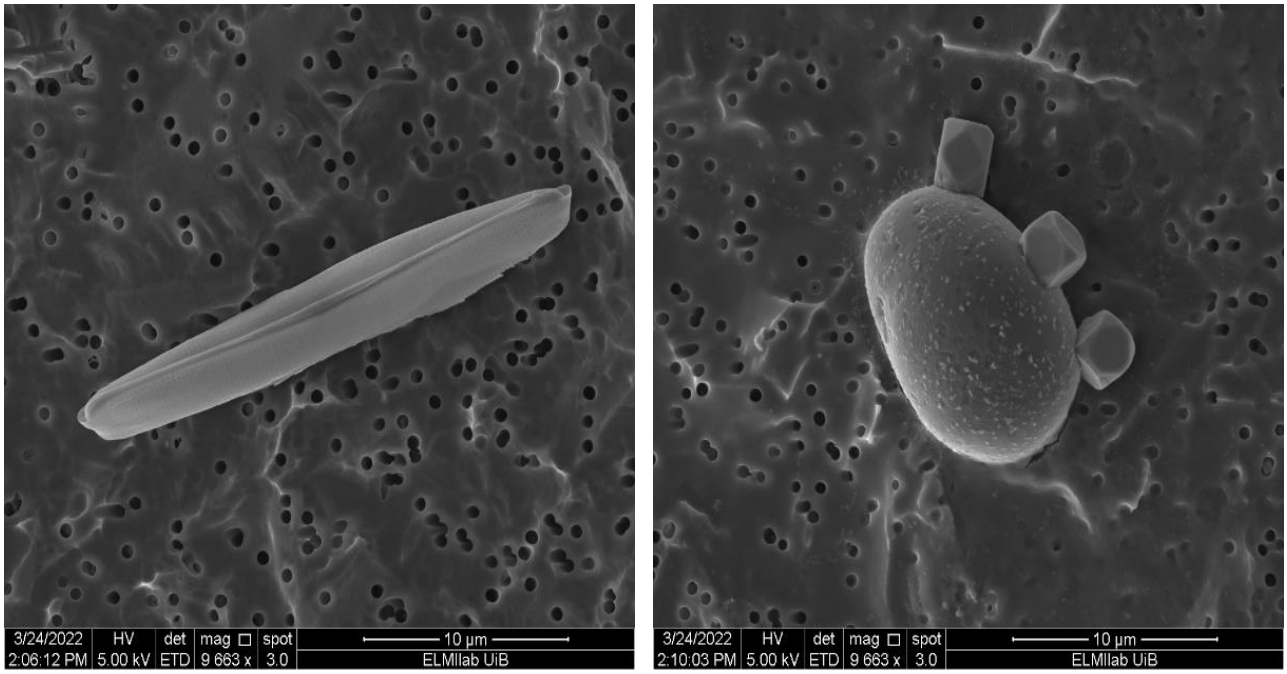

Figure 28. Images from SEM of the sample at P2 depth 40m in August 2018. Left: Pennate diatom, right: Unknown.

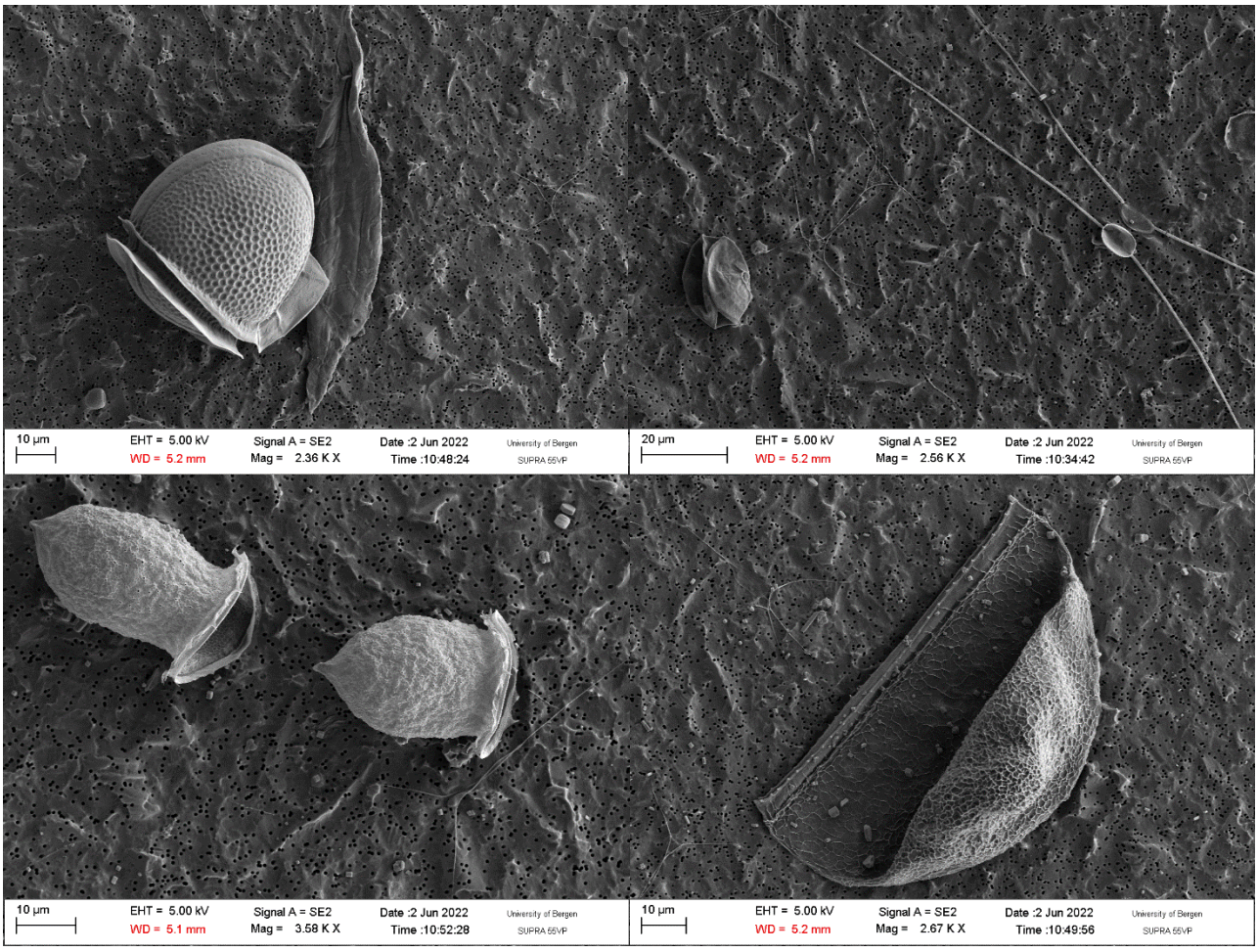

Figure 27. Images from SEM of the sample at P2 depth 181m in August 2018. Top-left: Dinophysis acuminata and pennate diatom, Top-right: Chaetoceros sp., Bottom-left: Acanthostomella norvegica -like, Bottom-right: Unknown tintinnid.

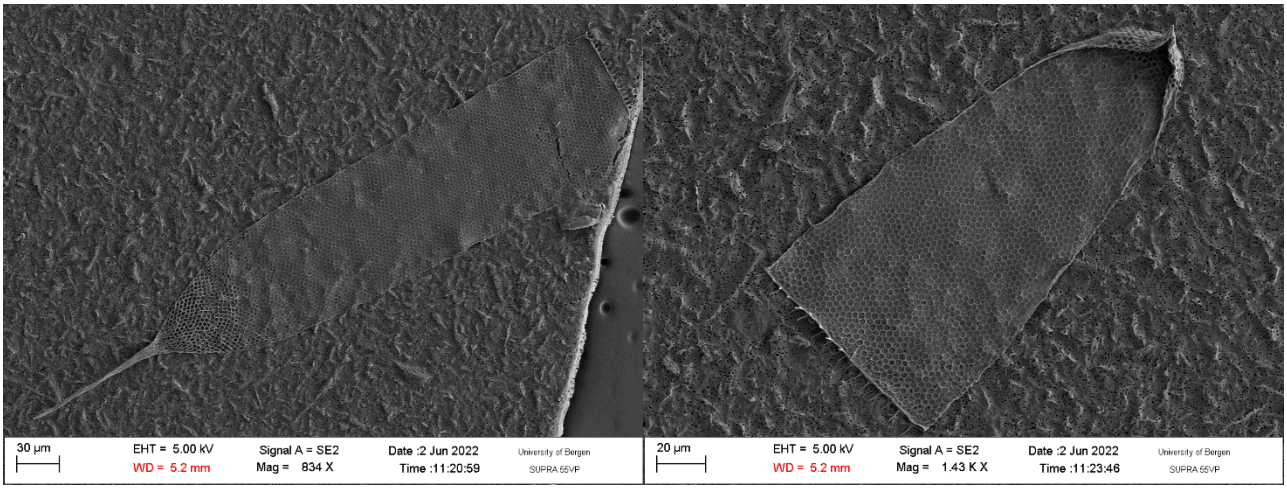

Figure 29. Images from SEM of the sample at P5 depth 30m in August 2018. Left: Parafavella gigantea, right: Parafavella acuta.

The first sample chosen from August 2019 was from station P1 at 50m depth. As mentioned previously in that location, Si and O marked a peak. The SEM results revealed an incredible diversity and abundance of resting stages known as stomatocysts that belong to an algal group called Chrysophyceae. At least 12 distinct stomatocyst types were recorded from that location. Stomatocysts are structures made up of silicate and until today their classification is a challenging task. Additionally, the species *Papposphaera sagitifera* Manton, Sutherland and McCully 1976, *Meringosphaera mediterranea*, and *Tetraparma catinifera* were also present in the sample (Figure 30)(Konno et al., 2007), as well as *Thalassiosira gravida* Cleve, 1896 , *Rhizosolenia imbricata* Brightwell, 1858 , *Chaetoceros* sp., Lauder, 1864 and *Arcocellulus cornucervis* G.R.Hasle, H.A.von Stosch & E.E.Syvertsen, 1983 (Figure 31).

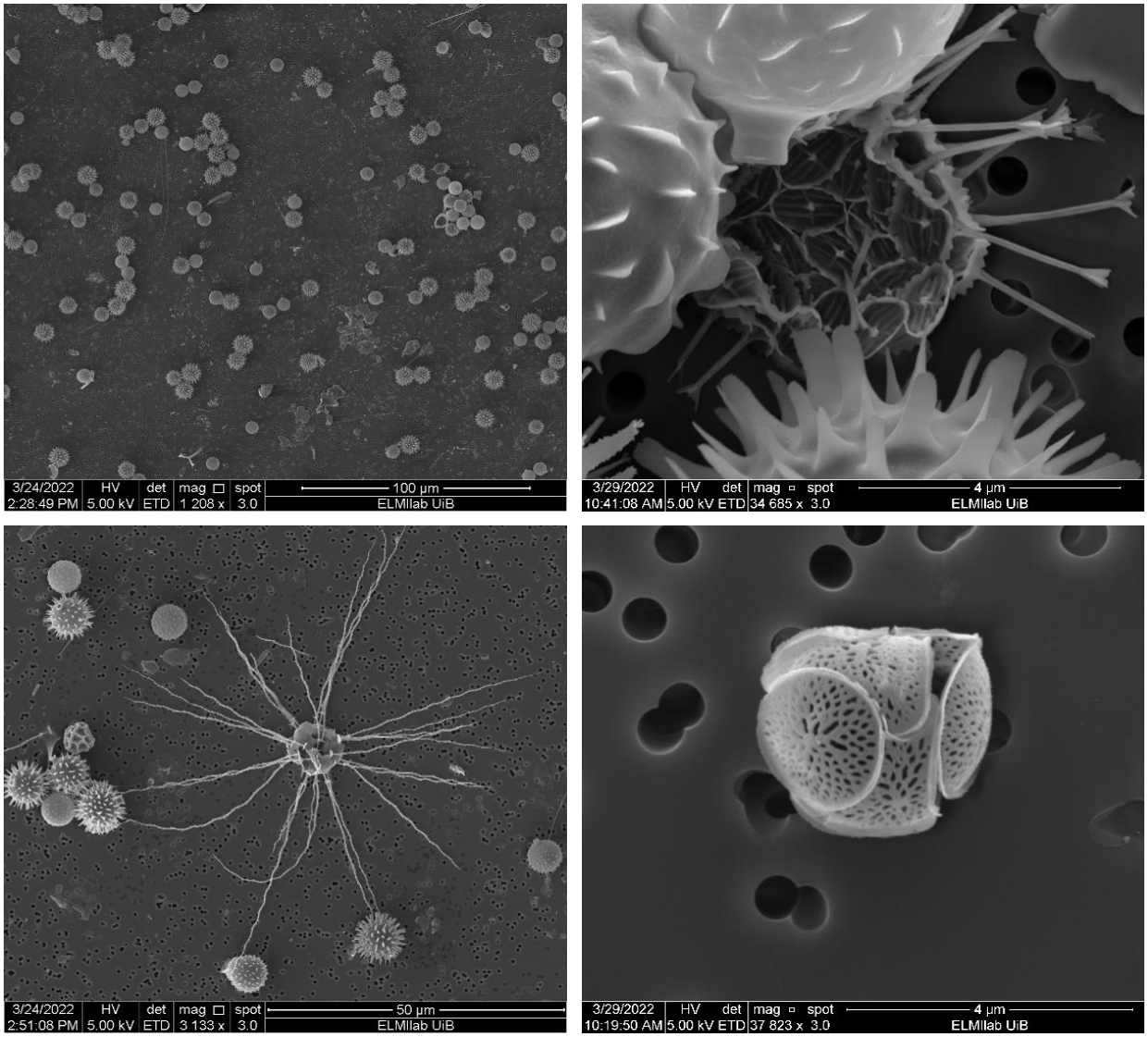

Figure 30. Images from SEM of the sample at P1 depth 50m in August 2019. Top-left: Overview of filter with Chrysophyceae stomatocysts, Top-right: Papposphaera sagitifera., Bottom-left: Meringosphaera mediterranea, Bottom-right: Tetraparma catinifera

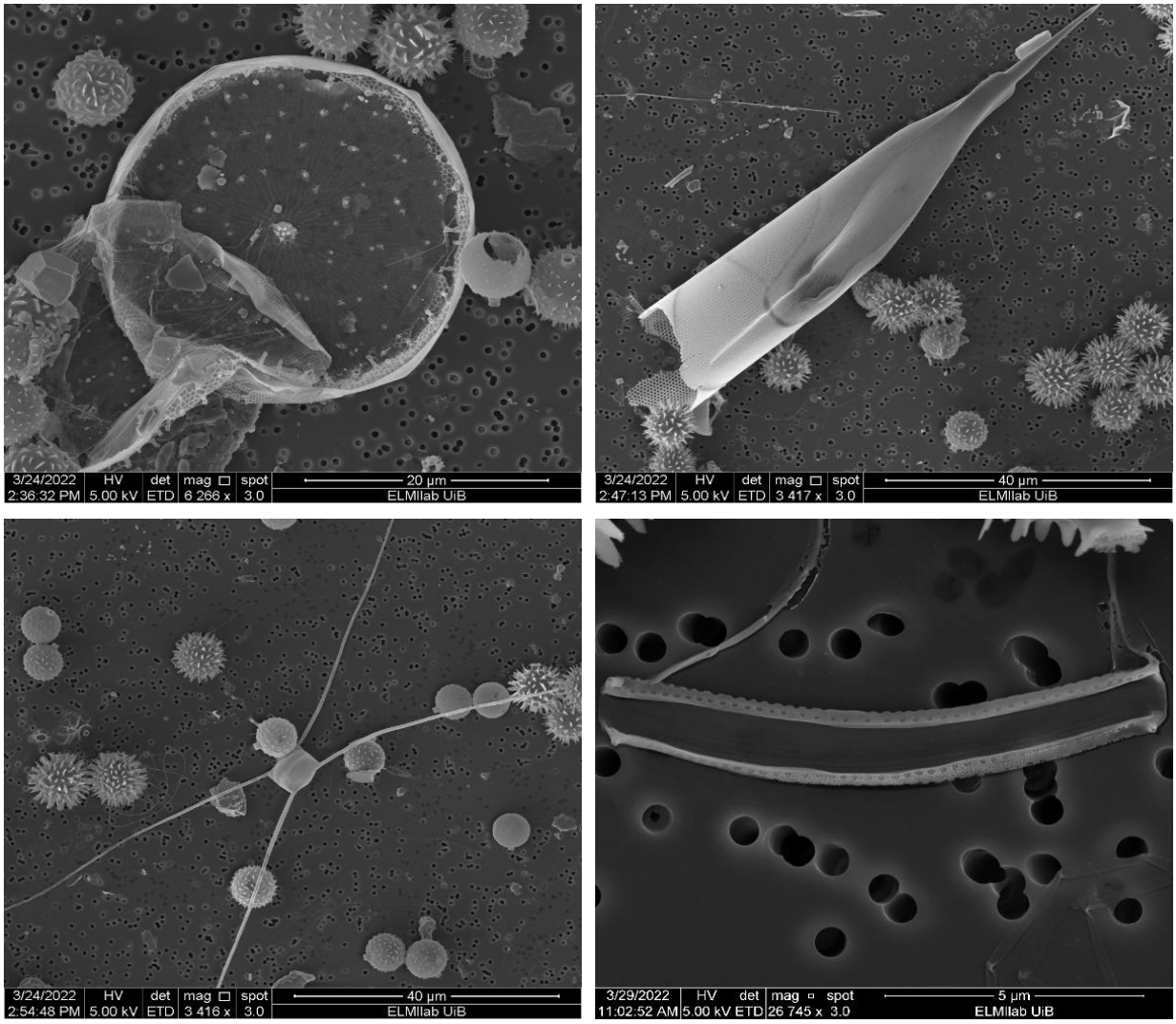

Figure 31. Images from SEM of the sample at P1 depth 50m in August 2019. Top-left: Thalassiosira gravida, Top-right: Rhizosolenia imbricata, Bottom-left: Chaetoceros sp., Bottom-right: Arcocellulus cornucervis

The examination of the sample from 315 m depth at P1 station due to high Si, Fe, Ca, O, K, Mg, revealed that this area was abundant with diatom frustules and Fe-Mn rings which also coincided with the high abundance of bacteria from the flowcytometry data. The most abundant diatoms belonged to *Thalassiosira, Navicula, Fragillariopsis*, and *Nitzschia* genuses Figure 32. At the surface of P2 station where high Ca, S, Na, Cl a Tintinnid species was identified (*Ptychocylis obtusa* Brandt, 1906) while many clusters of biogenic particles were present (Figure 32).

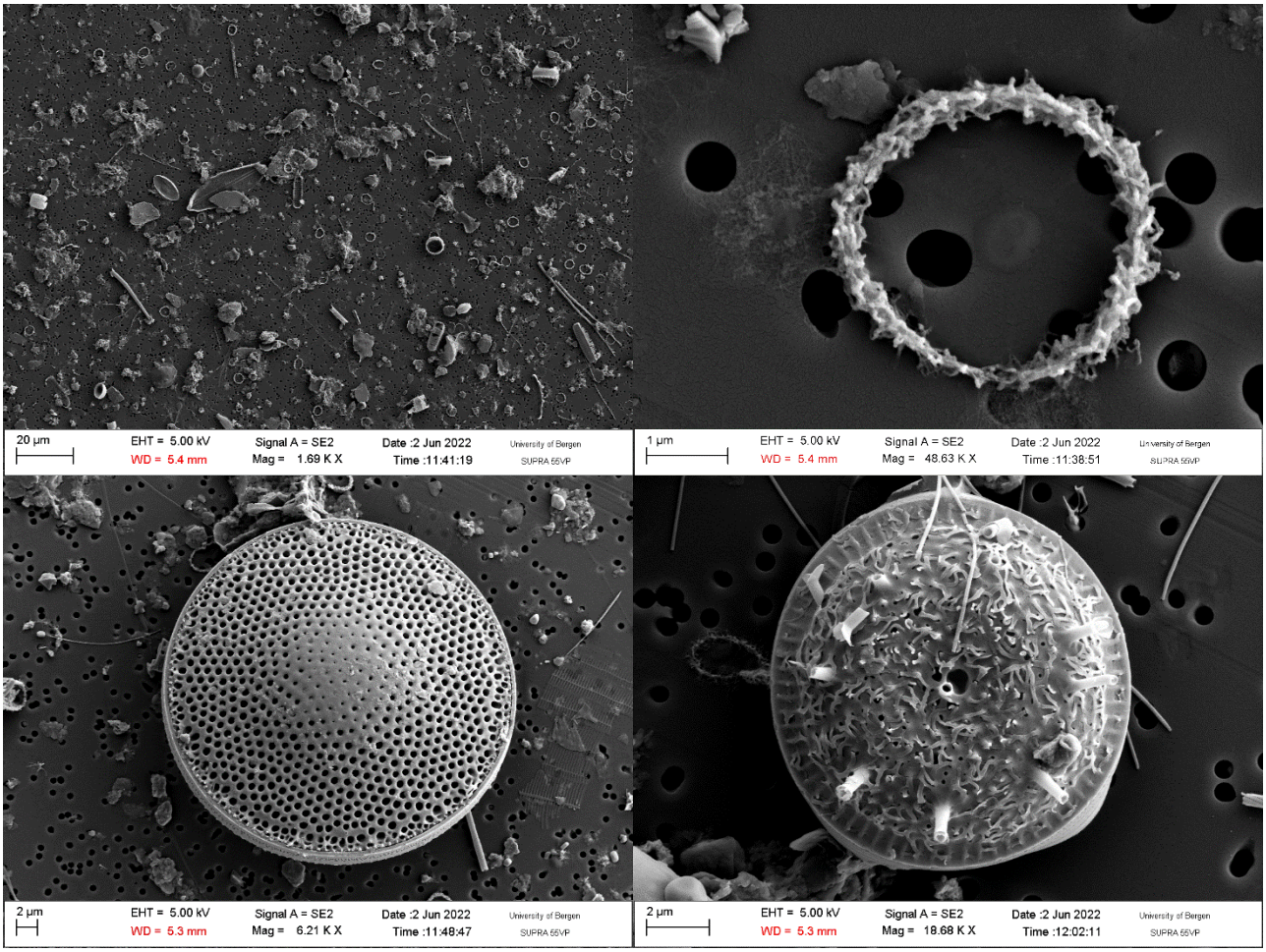

Figure 33. Images from SEM of the sample at P1 depth 315m in August 2019. Top-left: Overview of filter with broken diatom frustules and iron-manganese rings, Top-right: iron-manganese ring with what appears used to be a bacterial cell in the middle., Bottom-left: Thalassiosira sp., Bottom-right: Thalassiosira sp.

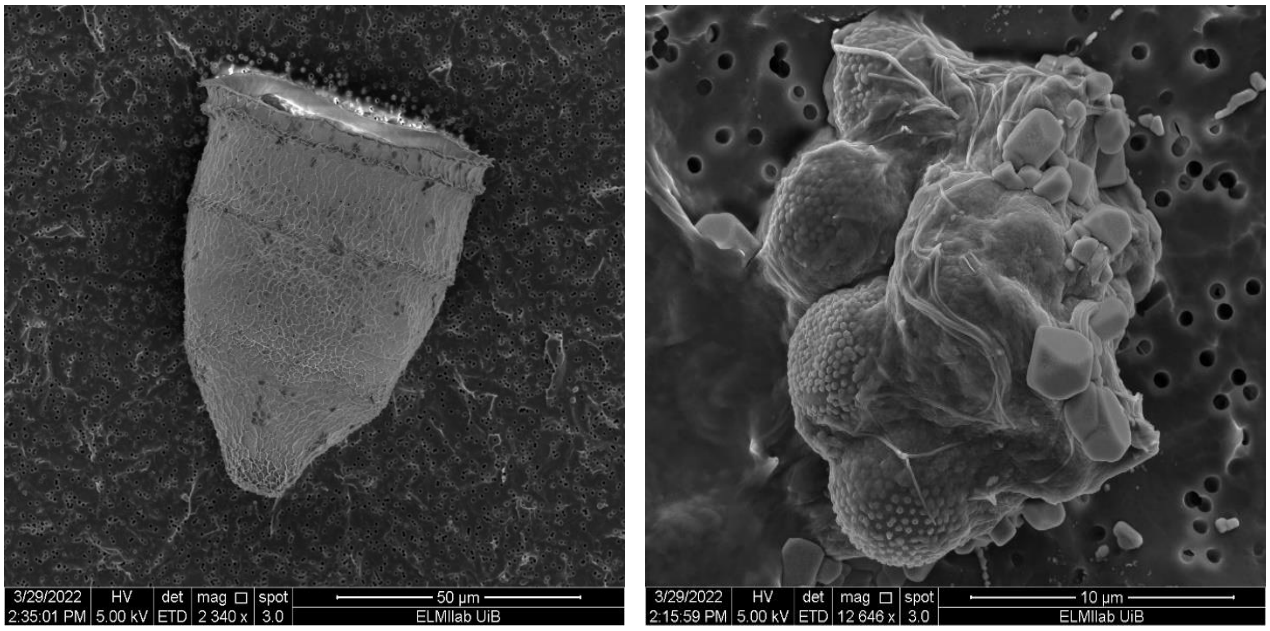

Figure 32. Images from SEM of the sample at P2 depth 10m in August 2019. Left: Ptychocylis obtusa, right: Aggregate with stomatocysts and debris.

The SEM images in Figure 34 from the bottom of P2 station where a maximum of Mn was registered, showed great abundance of Fe-Mn structures made by bacteria among debris from diatom and choanoflagellate skeletons. The location of the chlorophyll *a* max and Ca peak at P3 station – 30 m was dominated by choanoflagellate skeletons, the protist *Meringosphaera mediterranea*, the Tintinnid *Parafavella acuta* and colonies of unidentified circular cells (Figure 35). Moreover, the dinoflagellate *Dinophysis acuminata* Claparède & Lachmann, 1859 was also documented in that sample. Finally, the images from the last sample at station P5 – 15 m depth, depict the great abundance and diversity of diatoms especially of the genus *Thalassiosira* (Figure 36). At that locality, the highest amount of chlorophyll *a* was recorded from the whole study area in both years in combination with the high P, S, Si, O, Na, Cl, K, and Mg.

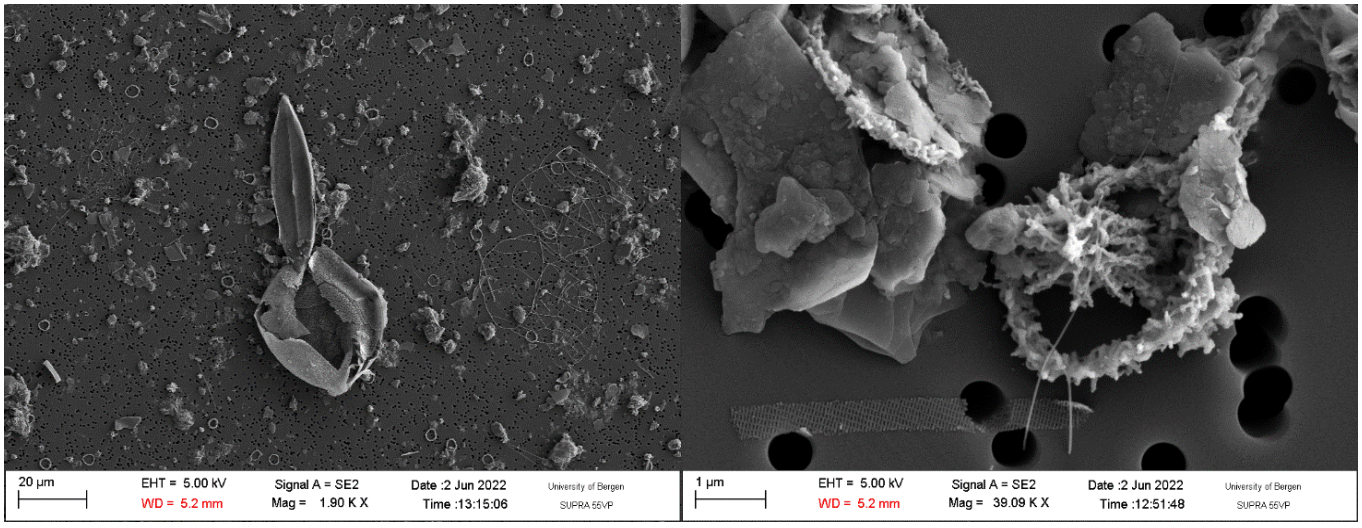

Figure 34. Images from SEM of the sample at P2 depth 185m in August 2019. Left: overview of the filter depicting destroyed diatom frustules, choanoflagellate skeletons and iron-manganese rings. Right: Fe-Mn arm-like network inside a ring.

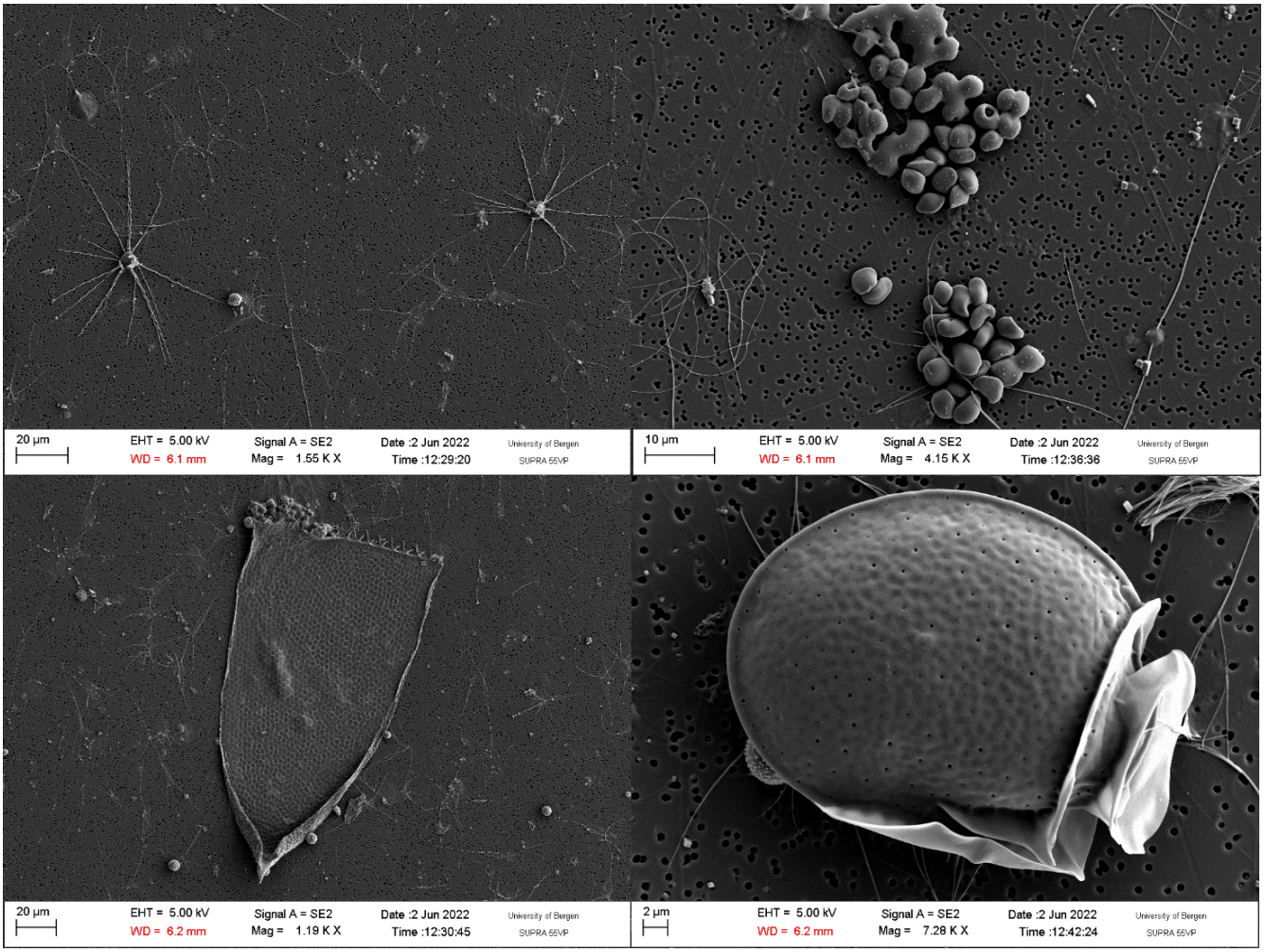

Figure 35. Images from SEM of the sample at P3 depth 30m in August 2019. Top-left: Overview of filter with Meringosphaera mediterranea and choanoglagellate skeletons, Top-right: colony of cells of unknown species., Bottom-left: Parafavella acuta, Bottom-right: Dinophysis acuminata.

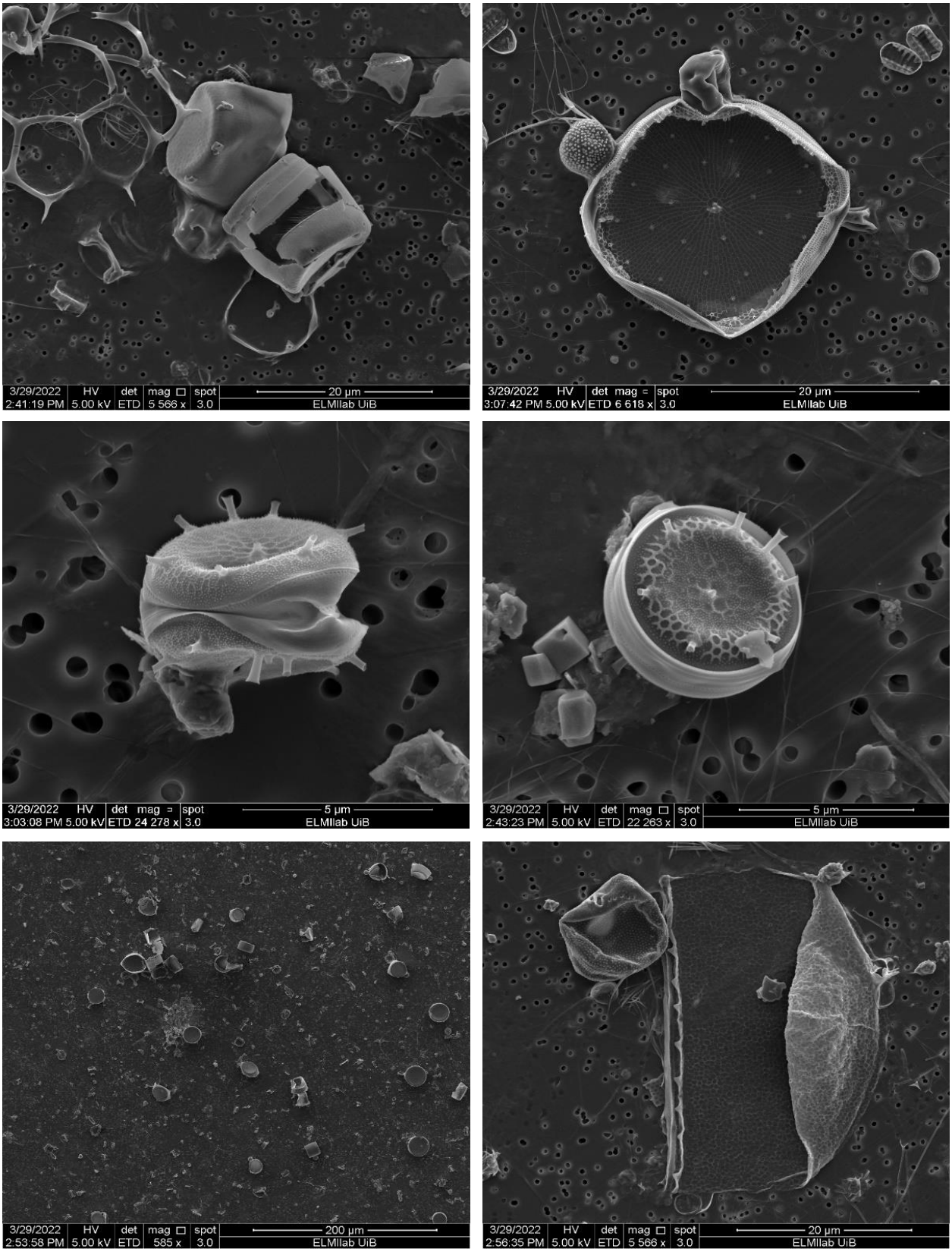

Figure 36. Images from SEM of the sample at P5 depth 15m in August 2019. Top-left: Thalassiosira sp., Top-right: Thalassiosira gravida, Middle-left: Thalassiosira sp., Middle-right: Thalassiosira sp., Bottom-left: Overview of Thalassiosira gravida chain, Bottom-right: Tintinnid ciliate.

4. Discussion

The scope of this thesis was to study the element composition of PM in the North-West BS, during two summers with contrasting sea ice conditions. The results presented here have addressed the three important aspects of this aim. Firstly, the concentration and distribution of different elements in the study area, secondly the link between the elements and finally the potential interactions/associations between them and among other biotic and hydrographical factors. All the findings highlight the uncertainty on how the fast changes in the seasonally ice-covered areas will affect the elemental availability keeping in mind that the element cycles are regulated by and regulate complex climatic and biotic processes.

4.1. Atlantic influence in the water masses

One of the questions in this study sought to determine how the contrasting environmental conditions might have influenced the elemental concentrations in the particulate pool. In the study area during August 2018, the most dominant water mass, especially in the southernmost stations, was a mixture of AW and mAW water with temperature between 0-6°C and salinity above 34.5 PSU. This is in accordance with previous results by (Aagaard & Woodgate, 2001) who demonstrated that the incoming AW coming from the south onto the north BS gets cooler (up to about 4°C) and slightly fresher (ca 0.2 PSU). In addition to that, a warm surface layer (<20 m depth) was clearly distinct throughout the transect, which could be attributed to the prolonged exposure to sun radiation, as a repercussion of prolonged sea ice absence. This kind of comparison presented here in a seasonally ice covered area is very crucial as it allows an insight to the future where less to no sea ice coverage is expected in the study area (Lind et al., 2018).

An important finding was that during August 2019 the conditions on the study transect pointed toward a colder and more stratified water column conditions and there was clear distinction of a fresher surface layer and a cold ArW mass dominating more than half of the study area compared to the year prior. This also accords to earlier observations and characterizations of the study area (Oziel et al., 2016). In the reviewing literature, the North part of BS is characterized by stronger stratification and a mixed shallow layer crossing the continental slope towards the Arctic Ocean

(Haug et al., 2017). Nevertheless, this stratification is expected to weaken with the intrusion of warm AW masses and enhanced wind exposure due to less sea ice. According to Hegseth & Sundfjord (2008), the AW mass found in the NW BS is originating from the west of Spitsbergen current that enters the Arctic and circumflows Kvitøya rather than the South of the BS. In the present thesis more information is needed to address that question of whether the AW mass came from the west of Spitsbergen or from the South BS, however, the location, the elevated temperatures and salinity as well as with the presence of Atlantic species like *Emiliania huxleyi* are indicators that this strong AW mass was advected from the south.

Overall, from this comparison the strong Atlantic influence was confirmed during the low ice coverage summer (August 2018). Several reports have shown that this documented Atlantification will result in increased productivity (Ingvaldsen et al., 2021; Neukermans et al., 2018; Oziel et al., 2020), however, this argument alone underestimates the effects on species composition and fundamental element cycling and energy transfer.

4.2. Particulate elemental composition

It is well known that the increase of photosynthetic organic matter explains changes in the surface water's chemical composition (Arrigo, 2005). This was very clear in the particulate P concentration which marked a distribution similar to that of chlorophyll *a* and detected in high amounts above 100 m depth, which is where most photosynthetic organisms are. However, we see that at the same time of the year, higher P concentrations were registered particularly under the ice at the ice covered station P5 compared to the P1 station in 2018 with the strongest Atlantic Influence. This, challenges many aspects of the observation that loss of sea ice will indeed contribute to elevated productivity. The slightly elevated concentrations of P below 200 m can be associated to sunken marine snow from the photic zone as supported by the SEM results as well. However, the values between 100-200 m depth where very low P concentrations were measured could be explained by rapid sinking rates of organic matter from the photic zone to the benthos. For comparative purposes, Bazzano et al.(2014) who measured the particulate concentration of trace metals in Kongsfjorden, Svalbard, during the summer and autumn season, measured an average of particulate P 0.046 µM for September and 0.061 µM for June which is generally less

than what was documented here in the BS for both years. Together with P, sulfur is another element linked with biologically derived organic matter and was mostly distributed in the upper part of the water column. This would explain the concentration of S also fluctuating accordingly to the microorganisms' abundances and chlorophyll *a* since it corresponds mainly to the cell content of glutathione, cysteine, and other basic cell constituents (Frausto da Silva & Williams, 2001). All the above suggest that the measured particulate S was of biogenic origin in both years.

It is interesting to note however, that the correlation and SEM results could suggest that the S measured in 2018 was probably from increased DMSP explained by the correlation between P-S-Ca-Nanophytoplankton and the presence of *E. huxleyi* in the study transect. These results were confirmed by CCA analysis which placed these parameters together in the same quartile of the biplot. For Ca that was the only significant correlation in 2018 while in 2019 it correlated with Mg, K, and O and was closer to bacterial abundance which indicates that the biogeochemical cycling of this element was drastically different between the two years. This is consistent with studies who showed that particulate Ca and especially $CaCO_3$ found in coccoliths is strongly enriched by Atlantic inflow and that in its inorganic form is closely linked to bacterial complexes (Erga et al., 2017). Equally, intriguing is the Ca peak in 2019 explained by the presence of the coccolithophore *Meringosphaera mediterranea* which has been documented previously in the BS and other polar areas (Georgiev et al., 2021).

Another interesting- finding was the significant correlations between the elements Mg -K -Si -Fe in 2018, which wasn't observed in 2019. Instead, Mg and K correlated more and had a similar distribution with P and S the second year. This is consistent with what has been found on Raunefjord by Erga et al. (2017) who interpreted this based on the partition of Mg and K in enzymes essential for photosynthesis and respiration. The P quotas of Mg and K tie well with earlier studies by Ho et al (2003) even though their results are based on measurements from individual cells. In accordance with their findings, diatoms contain high Mg cellular quotas, which corresponds to the present results from 2019 where we see high Mg concentration in the same localities of diatom dominance (P5, 5-20m). This could be true in this case as well as this suggestion is supported by the close placement of Mg

and Nanophytoplankton abundance in the CCA for both years. An explanation for the differences between the two years regarding the correlations mentioned in the beginning could lie to the fact that in 2018, very few diatoms were found in the water column compared to the sediments where, plenty of marine snow with diatom detritus was observed.

The findings from CCA analysis results revealed clearer patterns in particulate chemistry that allow us to interpret why the two years had a clear differentiation. The results demonstrate two things. Firstly, despite the strong correlation between the elements Si-Fe-Mg-O-K-Mn in 2018, Fe-Si-Mn were grouped closely together with deep samples as illustrated in CCA biplot. This implies that Fe-Si-Mn elements are possibly associated with matter from the bottom or that sunk to the bottom and was resuspended. Secondly, the correlation with Mg-K could mean that there was an underlying link between those elements and that were contained in non-living biological matter that sunk to deeper layers. However, the most important conclusion out of this finding is the clearly different patterns illustrated in 2018 and 2019, which does seem to prove the idea that the contrasting sea ice conditions, resulted in contrasting elemental patterns. More detailed, in 2019 we see again a pattern of Fe-Mn close together in deep samples exactly opposite from P and S in surface samples just like in 2018 nonetheless this time we see Si-O placed in between these two groups of samples (shallow-deep) mainly due to the higher abundance of diatoms in 2019. Overall, these findings at least point that there is a close link between the cycles and origin of these elements, as also proposed by Erga et al (2017).

4.3. Deep water pools of particulate matter

Particulate Si distribution in August 2018 and August 2019 corresponded closely with the particulate O distribution which is also supported by their strong positive correlation. This is expected as the overwhelming majority of Si is combined with O forming silicate (SiO_4)(Greenwood & Earnshaw, 2012). Si becomes available for diatoms after it is brought up to the photic zone by water column mixing at the end of the winter season, giving them a competitive advantage for the take-up of limiting nutrients like N and P (Egge & Aksnes, 1992; Larsen et al., 2015; Thingstad et al., 2005). Recent research indicates that glaciers and ice sheets are substantial contributors to the flux of nutrients such as Fe and Si (Hawkings et al., 2017). This

could explain the strong correlations between these elements in the study area for both years. If that is the case, this interaction may play a definitive role in the Si cycle in the future (Hátún et al., 2017; Rey, 2012). For comparative reasons only (Anderson & Dryssen, 1981) calculated the mean silica budget for the arctic ocean in the Svalbard area to be around 5.34 µM at a 200-500 m depth and increasing as it goes deeper and they hypothesized that shifts in the concentration of nutrients in the euphotic zone is heavily controlled by photosynthetic organic matter. They also suggested lower concentrations in AW masses that inflow to the Arctic Ocean on the west of Spitsbergen. This is in line with the results here despite the lower concentration range recorded in this thesis for both years. On another study, Hátún et al. (2017) reported the mean Si concentrations of Silicate-Rich-Arctic-Water in the Baffin Bay and Labrador Sea to be approximately 22 µM and in the Arctic Ocean 11 µM which is about 10 times higher than mean concentrations reported here. Overall, here is a clear relationship with increasing depth and silicate concentration in 2018 and a clear association with chlorophyll *a* above 100 m in 2019. This highlights the biogenic origin of Si whether that is sequestered in non-living matter originating from the water column but found in the sediments (2018), or is it is associated with the cell structures of silicifying sea-ice microorganisms in the upper parts of the water column (2019).

In this investigation both Fe and Mn were mainly observed in deep water and 50-100m above seafloor. Nonetheless, in this case it is unlikely that Fe in the particulate pool is of lithogenic sources exclusively. Bioavailable Fe occurs in extremely low concentrations in seawater due to its low solubility which causes it to precipitate rapidly and attach strongly to organic particles. In the deep, concentrations are governed mainly, by sinking particles, resuspension of material and scavenging during remineralization (Barrett et al., 2012; Breitbarth et al., 2010). One of the interesting findings from the CCA, is the placement of bacterial abundance and Fe in the same quartile for both years. This is directly in line with previous findings on the role of bacteria especially those found in detritus on the biogeochemical cycle of Fe (Barrett et al., 2012; Heldal et al., 1996; Sunda & Huntsman, 1995; Tortell et al., 1999; Twining & Baines, 2013). As previous studies suggest, Fe in the Arctic Ocean is replenished by river discharge and glacial runoff and then is distributed through the transpolar drift (Bazzano et al., 2014; Charette et al., 2020; Rijkenberg et al., 2018). Fe can also enter

the ocean via meltwater from sediment released from the base of glaciers and icebergs. Ice sheets at the poles hold substantial amounts of Fe accumulated from dust in snow over many millennia (Breitbarth et al., 2010). This variability in sources together with seasonal fluctuations might explain the great discrepancies in the concentrations recorded from other studies in other areas of the world (the values of Fe and Mn here exceed at least one order of magnitude the concentrations from other studies (Appendix 6.2, Table 22). Consequently, the particulate Fe in this thesis was most likely associated with a mix of biogenic material that has earlier sunk to the sediment and together with lithogenic sources, it was resuspended in the deepest parts of the transect.

In a recent publication, Kohler et al. (2022), reported for the current study area high Mn content near the sediment and within the concentration range reported in this thesis as well as high dissolved Mn near the shelf. They also suggested that the dissolved Mn originates from suboxic reducing in the shelf sediments which then is distributed by resuspension to upper layers which then later will sink again in various forms of precipitates and aggregates (Kohler et al., 2022). This notion was supported from much earlier studies which argued that the majority of Mn found near the seabed is the residue of resuspended PM (Price & Skei, 1975). However, the presence of Fe and Mn sequestering bacteria in some of the deep samples for both years suggests these microorganisms are of quantitative importance for the cycling of these elements in these locations (Heldal et al., 1996).

In general, the greatest discrepancies between the current thesis and other studies were in metal quotas for two main reasons. Firstly, because these types of data are mostly available and secondly because of the difference in studied area and technique applied. When comparing the current results to those of the older studies, there is a noticeable difference in the stoichiometries depending on the place (various locations and field vs lab), as well as with the technique and/or specific sample type (i.e., bulk, certain phylogenetic group, singular cells). For example, the Si, Mg, S, K quotas from both years were highly in agreement with the values measured by Erga et al. (2017) while Ca was slightly higher in their results and Fe quotas were slightly lower with no considerable differences. However, the results on Fe and Mn quotas

presented here exceed two and sometimes three orders of magnitude estimated quotas from other studies (Appendix 6.2, Table 20).

Twining and Baines (2013) concluded that the quotas obtained from nutrient replete cultures by Ho et al (2003) are not necessarily representative of oceanic phytoplankton, however, their results on K Mg and Ca seem to agree with the average quotas calculated here for the corresponding elements. They also, showed that diatoms in several regions of the Pacific have the highest metal quotas in comparison to other photosynthetic groups, which could possibly explain the higher quotas documented in 2019 where diatom abundance was much higher compared to the year prior. Traditionally, cell element quotas have been shown to fluctuate in response to ambient growth conditions, revealing nutrient limitations in a specific area. Although in this thesis elemental quotas come from bulk samples of PM, it could be argued that the generally higher quotas observed in 2019 evince a higher ambient nutrient availability. Aside from intraregional variability in the availability of elements, different functional groups/species display considerable differences in their chemistry and shifts in the balance of living vs non-living matter can all determine the observed elemental patterns at a given moment (Quigg et al., 2003; Twining & Baines, 2013). Consequently, at this stage of understanding, there are no entirely clear and cohesive explanations to these discrepancies in elemental quotas in ths region due to their complexity.

4.4. The strong link between particulate matter and marine microbes

It is widely known that marine microorganisms play a key role in the cycling of elements in the particulate pool. A summary of the role of microorganisms in the cycling of organic matter is depicted in Figure 37. The transport of POM to bottom waters was thought to be largely confined to large, rapidly sinking fecal pellets made up of digested phytoplankton cells (Tamelander et al., 2012). However, there is compiling evidence on the contribution picoplankton, heterotrophic bacteria, viruses and organic aggregates formed by diatoms and other microalgae (see summary of studies by Volkman & Tanoue (2002)) to the PM pool which is exported from the photic zone to deeper layers (Berdjeb et al., 2018; Buchan et al., 2014). As it is

demonstrated from the observation of the SEM samples, these aggregates occur very often and can reach the size of hundreds of µm. Numerous studies have shown that phytoplankton species show variation in their elemental composition (Bratbak & Thingstad, 1985; Egge & Aksnes, 1992; González-Dávila, 1995; Klausmeier et al., 2004; Lomas et al., 2019; Quigg et al., 2003; Sakshaug et al., 1983; Twining & Baines, 2013). This variation in composition influences both the stoichiometry of phytoplankton-derived POM and DOM (Finkel et al., 2006; Klausmeier et al., 2004; Rembauville et al., 2016; Sterner & Elser, 2008). This in turn influences the fate of microbially recycled organic matter by heterotrophic bacteria in the microbial loop (Azam et al., 1983;

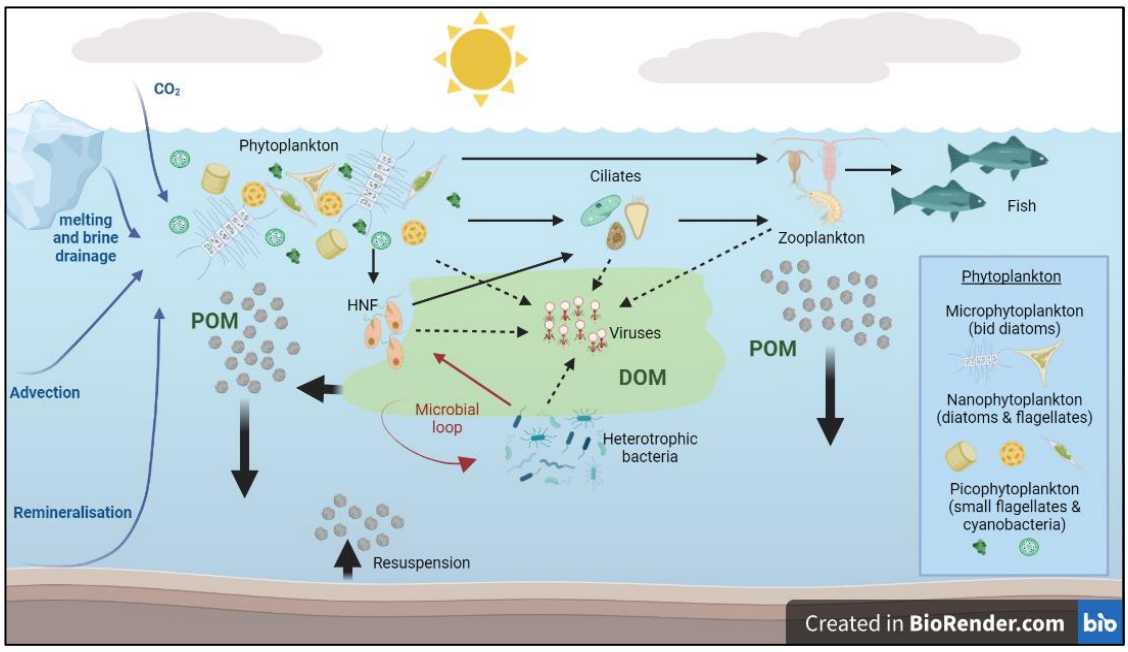

Figure 37. Marine microbial organisms are key players in the cycles of elements in the ocean. Inorganic matter from various sources depicted as blue arrows is taken up by photosynthetic phytoplankton species belonging to all size categories and converted into organic matter. Both POM and DOM are released from phytoplankton but can also originate from sediment resuspension, aerial deposition, terrestrial input, etc. The biological pump refers to the export of phytoplankton-derived POM (e.g., marine snow) from the euphotic zone to deeper depths via sinking. Another key process is the grazing of phytoplankton by zooplankton, (HNF) and ciliates which results in energy transfer through the food web and release of POM (fecal pellets, aggregates) and DOM. Recycling of organic matter takes place in the water column and is mediated by heterotrophic bacteria. Additionally, a fraction of the heterotrophic bacteria is consumed by heterotrophic flagellates, and the elements are further distributed in the food web. Bacteria also participate in the remineralization of organic nutrients to inorganic forms, which are then available for take up by phytoplankton. Finally, the viral shunt describes the contributions of viral-mediated cell lysis to the release of dissolved and PM from all the microbial pools.

Buchan et al., 2014; Enke et al., 2018).

It is widely discussed that a serious repercussion of sea ice loss is the timing of the phytoplankton blooms (Oziel et al., 2017), since the synchrony between trophic levels is essential for a productive ecosystem (Dalpadado et al., 2020; Edwards & Richardson, 2004). Another aftermath of the receding Arctic sea ice is the

development of a second, fall bloom as a result of wind-driven vertical mixing due to increased exposure of the sea surface without the ice presence (Ardyna et al., 2014). All these changes indicate that the Arctic Ocean might be transitioning to temperate conditions, which is likely to shift the spatial and temporal distribution of Arctic and sub-Arctic species with a stronger prevalence of temperate algae (Dalpadado et al., 2020; Kortsch et al., 2015; Oziel et al., 2020). For some species this might mean successful expansion (Makarevich et al., 2021) and for others inevitable extinction (Wassmann et al., 2015). In some cases, the fate of some microbial groups lies on the changing nutrient concentrations phytoplankton (Egge & Aksnes, 1992; Hátún et al., 2017; Krumhardt et al., 2017; Oziel et al., 2020; Rey, 2012). A similar conclusion was reached by Paulsen et al. (2016) who observed dominance of picophytoplankton typically from low latitudes (*Synechococcus*) in areas of the Arctic that was previously dominated by larger species adapted to low temperatures. In a typical BS summer, large algal-bacterial aggregates form as a result the sea ice melting is (Rapp et al., 2018). Consequently, the water column gets dominated by typically smaller sized organisms adapted to oligotrophic conditions and increased bacterial production (Kirchman, 1994). Later as autumn enters and ice formation starts taking place, some algae mainly pennate diatoms and small flagellates dominate as long as light and nutrients are available (Marquardt et al., 2016; Thomas & Dieckmann, 2008; Vader et al., 2015).

A possible explanation for August 2018 leans towards the invasion from a south water mass which brought along or favored the prevalence of temperate species like *Emiliania huxleyi* as discussed previously. Moreover, in 2018 picophytoplankton were the dominant group of photosynthetic organisms, at the same time numerous dinoflagellate and ciliate species were also found in considerable numbers. This, in combination with the high bacterial numbers would signify less predation on heterotrophic bacteria. All of the above suggest that the conditions during August 2018 could be characterized late post-bloom. Contrarily, in August 2019 due to the noticeable presence of ArW in the northern part of study area where sea ice was present higher abundance and diversity of diatoms were documented, which point to an earlier post-bloom state. These differences between the years, are a great opportunity to study what can happen in the elemental pools if the microbial food

web shifts from the classical biological pump towards the microbial loop. However, it is important to remember that these are complex processes and should be interpreted with caution.

It is beyond any doubt that among the findings shown in this thesis, the most intriguing is the Chrysophyceae stomatocysts found at 50 m depth P1 station in 2019 (Figure 38). Nonetheless, several questions are still unanswered as there is great uncertainty on the reason that can explain their presence in that location. The recorded diversity and abundance of these stomatocysts was something that hasn't been reported at least to that degree in any other study from the area. Chrysophytes are mainly freshwater species and their stomatocysts are usually found in lake sediments as well as in meltponds and in connection with ice. Some species of *Dinobryon* sp. however, are commonly found in brackish waters in high latitudes (Piątek et al., 2020). However, their taxonomic identification can be extremely challenging as it requires observations of both the vegetative and resting cells (Wilkinson et al., 2001).

Regarding the limitations of this thesis, it could be argued that more data from different seasons are needed to build a better picture about the marine PM composition and its fate in the future BS, as particulate elemental composition can be highly variable between seasons. For that reason, it must be highlighted that the results presented here cannot supply a prediction of how the system of BS will respond to future climate change, but simply a comparison of two different cases and an effort to describe the repercussions of sea ice loss for the elemental pools. An apparent limitation in the method naturally involves the issue of the equipment low sensitivity to trace element concentration, which can potentially be resolved by filtering greater amounts of seawater. Despite that, it is an overall, ingenious and practical method for bulk measurements of particulate elemental concentrations, that provides fast and reliable results (Paulino et al., 2018). Another limitation in the results involves the issue that high values recorded due to sediment resuspension can possibly "mask" the euphotic zone values. The CCA displayed a limited capacity for the 2019 dataset. This indicates that other factors might be relevant in explaining the observed patterns such as microplankton abundances or even a species diversity data. Lastly, the mechanisms behind the hypothesized sediment resuspension that could

explain the high elemental concentrations in the samples above the seafloor is certainly an area that needs more supporting information.

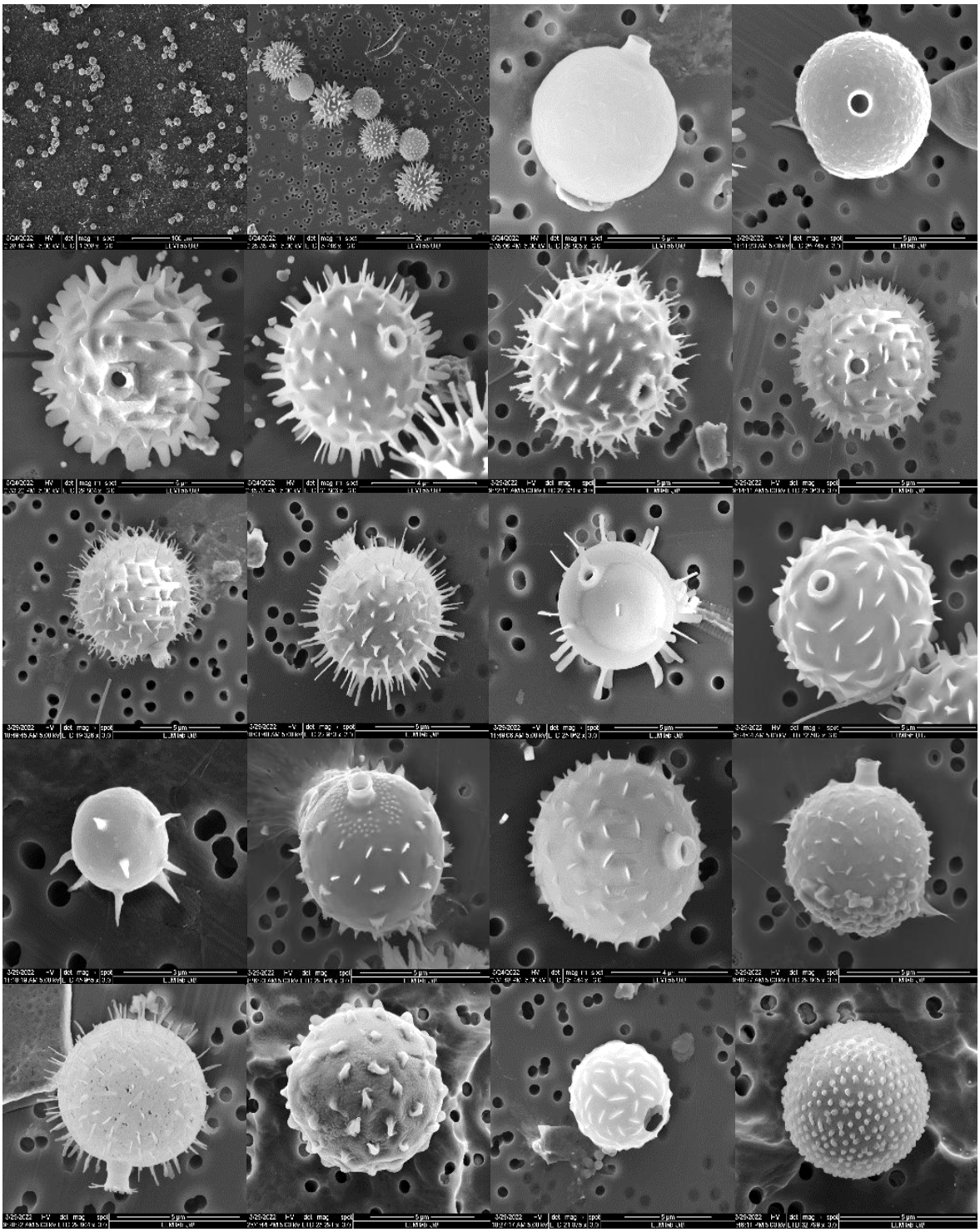

Figure 38. P1 - 50 m, Chrysophyceae stomatocysts.

4.5. Conclusions

The purpose of this thesis was to investigate the particulate elemental composition of the North-West BS during two years with different sea ice conditions, to further understand the mechanisms behind element cycling and the repercussions of future sea ice loss on the BS ecosystem. This study clearly illustrated the difference in the elemental composition of PM between August 2018 and August 2019, revealing that the Atlantic influence in 2018 and the sea ice presence in 2019 created conditions for a different elemental distribution as well as microbial community. Based on the present findings from CCA and SEM, it can be concluded that for the upper layers of the study area in 2018 the elements P, S, Mg, K, Ca were primarily associated with living biological material from the euphotic zone. The high elemental concentrations of Si, O, Fe and Mn found in the in deepest samples manifest a strong link between resuspended non-living biogenic and lithogenic matter in these elemental pools. On the contrary, in 2019 the distribution of elements and especially that of Si in the photic zone was strongly linked to the diatom dominated community. Finally, it was confirmed by SEM images that high elemental content of some samples corresponded to the plankton groups most commonly associated with them i.e., Ca - coccolithophores, Si - diatoms, Chrysophyceae stomatocysts and Tintinnids, Fe & Mn - bacteria.

Overall, the results successfully cast new light on the particulate elemental composition in the North-West BS, nonetheless, there is still so much left to uncover due to the limitations discussed and high variability in several regions and even between individual cells. For that reason, future research should aim to replicate results in several areas to make comparisons easier and the interpretation of elemental patterns more credible. Another interesting topic for future work is species specific elemental composition from natural samples that can be used as an indicator of elemental availability in their environment. In conclusion, this thesis opens new avenues of investigation on the effects of sea ice loss on elemental pools and biological productivity. The findings of this thesis have brought up new knowledge and insight that warrant future research.

5. References

Aagaard, K., & Woodgate, R. A. (2001). Some thoughts on the freezing and melting of sea ice and their effects on the ocean. *Ocean Modelling*, *3*(1-2), 127-135. https://doi.org/10.1016/s1463-5003(01)00005-1

Anderson, L., & Dryssen, D. (1981). Chemical-constituents of the arctic ocean in the Svalbard area. *Oceanologica Acta*, *4*(3), 305-311.

Ardyna, M., Babin, M., Gosselin, M., Devred, E., Rainville, L., & Tremblay, J.-É. (2014). Recent Arctic Ocean sea ice loss triggers novel fall phytoplankton blooms. *Geophysical Research Letters*, *41*(17), 6207-6212. https://doi.org/10.1002/2014gl061047

Armstrong, R. A. (2014). When to use the Bonferroni correction. *Ophthalmic and Physiological Optics*, *34*(5), 502-508. https://doi.org/10.1111/opo.12131

Arrigo, K. R. (2005). Marine microorganisms and global nutrient cycles. *Nature*, *437*(7057), 349-355. https://doi.org/10.1038/nature04159

Azam, F., Fenchel, T., Field, J., Gray, J., Meyer-Reil, L., & Thingstad, F. (1983). The ecological role of water-column microbes in the sea. *Marine Ecology Progress Series*, *10*, 257-263. https://doi.org/10.3354/meps010257

Barrett, P. M., Resing, J. A., Buck, N. J., Buck, C. S., Landing, W. M., & Measures, C. I. (2012). The trace element composition of suspended particulate matter in the upper 1000m of the eastern North Atlantic Ocean: A16N. *Marine Chemistry*, *142-144*, 41-53. https://doi.org/10.1016/j.marchem.2012.07.006

Bazzano, A., Rivaro, P., Soggia, F., Ardini, F., & Grotti, M. (2014). Anthropogenic and natural sources of particulate trace elements in the coastal marine environment of Kongsfjorden, Svalbard. *Marine Chemistry*, *163*, 28-35. https://doi.org/10.1016/j.marchem.2014.04.001

Behrenfeld, M. J., Bale, A. J., Kolber, Z. S., Aiken, J., & Falkowski, P. G. (1996). Confirmation of iron limitation of phytoplankton photosynthesis in the equatorial Pacific Ocean. *Nature*, *383*(6600), 508-511. https://doi.org/10.1038/383508a0

Berdjeb, L., Parada, A., Needham, D. M., & Fuhrman, J. A. (2018). Short-term dynamics and interactions of marine protist communities during the spring–

summer transition. *The ISME Journal*, *12*(8), 1907-1917. https://doi.org/10.1038/s41396-018-0097-x

Blanchet, G. F., Legendre, P., & Borcard, D. (2008). Forward selection of explanatory variables. *Ecology*, *89*(9), 2623-2632. https://doi.org/10.1890/07-0986.1

Borowitzka, M. A., Beardall, J., & Raven, J. A. (2016). *The physiology of microalgae* (Vol. 6). Springer.

Bratbak, G., Jacquet, S., Larsen, A., Pettersson, L. H., Sazhin, A. F., & Thyrhaug, R. (2011). The plankton community in Norwegian coastal waters—abundance, composition, spatial distribution and diel variation. *Continental Shelf Research*, *31*(14), 1500-1514. https://doi.org/10.1016/j.csr.2011.06.014

Bratbak, G., & Thingstad, T. F. (1985). Phytoplankton-bacteria interactions: an apparent paradox? Analysis of a model system with both competition and commensalism. *Marine ecology progress series. Oldendorf*, *25*(1), 23-30.

Breitbarth, E., Achterberg, E. P., Ardelan, M. V., Baker, A. R., Bucciarelli, E., Chever, F., . . . Ye, Y. (2010). Iron biogeochemistry across marine systems – progress from the past decade. *Biogeosciences*, *7*(3), 1075-1097. https://doi.org/10.5194/bg-7-1075-2010

Buchan, A., Lecleir, G. R., Gulvik, C. A., & González, J. M. (2014). Master recyclers: features and functions of bacteria associated with phytoplankton blooms. *Nature Reviews Microbiology*, *12*(10), 686-698. https://doi.org/10.1038/nrmicro3326

Charette, M. A., Kipp, L. E., Jensen, L. T., Dabrowski, J. S., Whitmore, L. M., Fitzsimmons, J. N., . . . Zhang, R. (2020). The transpolar drift as a source of riverine and shelf-derived trace elements to the central arctic Ocean. *Journal of Geophysical Research: Oceans*, *125*(5), e2019JC015920. https://doi.org/10.1029/2019jc015920

Charlson, R. J., Lovelock, J. E., Andreae, M. O., & Warren, S. G. (1987). Oceanic phytoplankton, atmospheric sulphur, cloud albedo and climate. *Nature*, *326*(6114), 655-661. https://doi.org/10.1038/326655a0

Collier, R., & Edmond, J. (1984). The trace element geochemistry of marine biogenic particulate matter. *Progress in Oceanography*, *13*(2), 113-199. https://doi.org/10.1016/0079-6611(84)90008-9

Dalpadado, P., Arrigo, K. R., Van Dijken, G. L., Skjoldal, H. R., Bagøien, E., Dolgov, A. V., . . . Sperfeld, E. (2020). Climate effects on temporal and spatial dynamics of phytoplankton and zooplankton in the Barents Sea. *Progress in Oceanography*, *185*, 102320. https://doi.org/10.1016/j.pocean.2020.102320

Dalpadado, P., Ingvaldsen, R. B., Stige, L. C., Bogstad, B., Knutsen, T., Ottersen, G., & Ellertsen, B. (2012). Climate effects on Barents Sea ecosystem dynamics. *ICES Journal of Marine Science*, *69*(7), 1303-1316. https://doi.org/10.1093/icesjms/fss063

Dolan, J. R., Pierce, R. W., & Yang, E. J. (2017). Tintinnid ciliates of the marine microzooplankton in Arctic Seas: a compilation and analysis of species records. *Polar Biology*, *40*(6), 1247-1260. https://doi.org/10.1007/s00300-016-2049-0

Edwards, M., & Richardson, A. J. (2004). Impact of climate change on marine pelagic phenology and trophic mismatch. *Nature*, *430*(7002), 881-884. https://doi.org/10.1038/nature02808

Egge, J., & Aksnes, D. (1992). Silicate as regulating nutrient in phytoplankton competition. *Marine Ecology Progress Series*, *83*, 281-289. https://doi.org/10.3354/meps083281

Enke, T. N., Leventhal, G. E., Metzger, M., Saavedra, J. T., & Cordero, O. X. (2018). Microscale ecology regulates particulate organic matter turnover in model marine microbial communities. *Nature Communications*, *9*(1). https://doi.org/10.1038/s41467-018-05159-8

Erga, S. R., Haugen, S. B., Bratbak, G., Egge, J. K., Heldal, M., Mork, K. A., & Norland, S. (2017). Seasonal variations in C:N:Si:Ca:P:Mg:S:K:Fe relationships of seston from Norwegian coastal water: Impact of extreme offshore forcing during winter-spring 2010. *Marine Chemistry*, *196*, 1-12. https://doi.org/10.1016/j.marchem.2017.07.001

Fagerbakke, K. M., Heldal, M., Norland, S., Heimdal, B. R., & Båtvik, H. (1994). Emiliania huxleyi. Chemical composition and size of coccoliths from enclosure experiments and a Norwegian fjord. *Sarsia*, *79*(4), 349-355. https://doi.org/10.1080/00364827.1994.10413566

Finkel, Z. V., Quigg, A., Raven, J. A., Reinfelder, J. R., Schofield, O. E., & Falkowski, P. G. (2006). Irradiance and the elemental stoichiometry of marine phytoplankton. *Limnology and Oceanography*, *51*(6), 2690-2701. https://doi.org/10.4319/lo.2006.51.6.2690

Frausto da Silva, J., & Williams, R. (2001). *The biological chemistry of the elements: the inorganic chemistry of life*. Oxford University Press.

Frigstad, H., Andersen, T., Hessen, D. O., Naustvoll, L. J., Johnsen, T. M., & Bellerby, R. G. J. (2011). Seasonal variation in marine C:N:P stoichiometry: can the composition of seston explain stable Redfield ratios? *Biogeosciences*, *8*(10), 2917-2933. https://doi.org/10.5194/bg-8-2917-2011

Gamela, R. R., Costa, V. C., Sperança, M. A., & Pereira-Filho, E. R. (2020). Laser-induced breakdown spectroscopy (LIBS) and wavelength dispersive X-ray fluorescence (WDXRF) data fusion to predict the concentration of K, Mg and P in bean seed samples. *Food Research International*, *132*, 109037. https://doi.org/10.1016/j.foodres.2020.109037

Geider, R., & La Roche, J. (2002). Redfield revisited: variability of C:N:P in marine microalgae and its biochemical basis. *European Journal of Phycology*, *37*(1), 1-17. https://doi.org/10.1017/S0967026201003456

Georgiev, A. A., Georgieva, M. L., & Gololobova, M. A. (2021). New observations of Meringosphaera mediterranea from russion arctic seas, including a review of global disrtibution. *Новости систематики низших растений*, *55*(22), 19.

González-Dávila, M. (1995). The role of phytoplankton cells on the control of heavy metal concentration in seawater. *Marine Chemistry*, *48*(3-4), 215-236. https://doi.org/10.1016/0304-4203(94)00045-f

Greenwood, N. N., & Earnshaw, A. (2012). *Chemistry of the elements*. Elsevier.

Grossart, H., Kiørboe, T., Tang, K., Allgaier, M., Yam, E., & Ploug, H. (2006). Interactions between marine snow and heterotrophic bacteria: aggregate formation and microbial dynamics. *Aquatic Microbial Ecology*, *42*, 19-26. https://doi.org/10.3354/ame042019

Haug, T., Bogstad, B., Chierici, M., Gjøsæter, H., Hallfredsson, E. H., Høines, Å. S., . . . Sunnanå, K. (2017). Future harvest of living resources in the Arctic Ocean north of the Nordic and Barents Seas: A review of possibilities and

constraints. *Fisheries Research*, *188*, 38-57. https://doi.org/10.1016/j.fishres.2016.12.002

Hawkings, J. R., Wadham, J. L., Benning, L. G., Hendry, K. R., Tranter, M., Tedstone, A., . . . Raiswell, R. (2017). Ice sheets as a missing source of silica to the polar oceans. *Nature Communications*, *8*(1), 14198. https://doi.org/10.1038/ncomms14198

Hegseth, E. N., & Sundfjord, A. (2008). Intrusion and blooming of Atlantic phytoplankton species in the high Arctic. *Journal of Marine Systems*, *74*(1-2), 108-119. https://doi.org/10.1016/j.jmarsys.2007.11.011

Heldal, M., Fagerbakke, K. M., Tuomi, P., & Bratbak, G. (1996). Abundant populations of iron and manganese sequestering bacteria in coastal water. *Aquatic Microbial Ecology*, *11*, 127-133. https://doi.org/10.3354/ame011127

Heldal, M., Norland, S., Erichsen, E. S., Sandaa, R.-A., Larsen, A., Thingstad, F., & Bratbak, G. (2012). Mg2+ as an indicator of nutritional status in marine bacteria. *The ISME Journal*, *6*(3), 524-530. https://doi.org/10.1038/ismej.2011.130

Ho, T.-Y., Quigg, A., Finkel, Z. V., Milligan, A. J., Wyman, K., Falkowski, P. G., & Morel, F. M. M. (2003). The elemental composition of some marine phytoplankton. *Journal of Phycology*, *39*(6), 1145-1159. https://doi.org/10.1111/j.0022-3646.2003.03-090.x

Hátún, H., Azetsu-Scott, K., Somavilla, R., Rey, F., Johnson, C., Mathis, M., . . . Ólafsson, J. (2017). The subpolar gyre regulates silicate concentrations in the North Atlantic. *Scientific Reports*, *7*(1). https://doi.org/10.1038/s41598-017-14837-4

Ingvaldsen, R. B., Assmann, K. M., Primicerio, R., Fossheim, M., Polyakov, I. V., & Dolgov, A. V. (2021). Physical manifestations and ecological implications of Arctic Atlantification. *Nature Reviews Earth & Environment*, *2*(12), 874-889. https://doi.org/10.1038/s43017-021-00228-x

Jensen, F., & Winding Hansen, B. (2000). Ciliates and heterotrophic dinoflagellates in the marginal ice zone of the central Barents Sea during spring. *Journal of the Marine Biological Association of the United Kingdom*, *80*(1), 45-54. https://doi.org/10.1017/s0025315499001551

Kay, A. D., & Vrede, T. (2008). Evolutionary and Biochemical Aspects. In (pp. 1472-1481). Elsevier. https://doi.org/10.1016/b978-008045405-4.00305-0

Kirchman, D. L. (1994). The uptake of inorganic nutrients by heterotrophic bacteria. *Microbial Ecology*, *28*(2), 255-271. https://doi.org/10.1007/bf00166816

Klausmeier, C. A., Litchman, E., Daufresne, T., & Levin, S. A. (2004). Optimal nitrogen-to-phosphorus stoichiometry of phytoplankton. *Nature*, *429*(6988), 171-174. https://doi.org/10.1038/nature02454

Kohler, S. G., Heimbürger-Boavida, L.-E., Petrova, M. V., Digernes, M. G., Sanchez, N., Dufour, A., . . . Ardelan, M. V. (2022). Arctic Ocean's wintertime mercury concentrations limited by seasonal loss on the shelf. *Nature Geoscience*. https://doi.org/10.1038/s41561-022-00986-3

Konno, S., Ohira, R., Komuro, C., Harada, N., & Jordan, R. W. (2007). Six new taxa of subarctic Parmales (Chrysophyceae). *Journal of Nannoplankton Research*, *29*(2), 108-128.

Kortsch, S., Primicerio, R., Fossheim, M., Dolgov, A. V., & Aschan, M. (2015). Climate change alters the structure of arctic marine food webs due to poleward shifts of boreal generalists. *Proceedings of the Royal Society B: Biological Sciences*, *282*(1814), 20151546. https://doi.org/10.1098/rspb.2015.1546

Krumhardt, K. M., Lovenduski, N. S., Iglesias-Rodriguez, M. D., & Kleypas, J. A. (2017). Coccolithophore growth and calcification in a changing ocean. *Progress in Oceanography*, *159*, 276-295. https://doi.org/10.1016/j.pocean.2017.10.007

Kršinić, F. (2018). Fauna of tintinnids (Tintinnida, Ciliata) during an Arctic-Antarctic cruise, with the S/V "Croatian Tern". *Zootaxa*, *4399*(3), 301. https://doi.org/10.11646/zootaxa.4399.3.1

Langer, M. R. (2008). Assessing the contribution of foraminiferan protists to global ocean carbonate production. *Journal of Eukaryotic Microbiology*, *55*(3), 163-169. https://doi.org/10.1111/j.1550-7408.2008.00321.x

Larsen, A., Egge, J. K., Nejstgaard, J. C., Di Capua, I., Thyrhaug, R., Bratbak, G., & Thingstad, T. F. (2015). Contrasting response to nutrient manipulation in A rctic mesocosms are reproduced by a minimum microbial food web model. *Limnology and Oceanography*, *60*(2), 360-374. https://doi.org/10.1002/lno.10025

Lee, S., Wolberg, G., & Shin, S. Y. (1997). Scattered data interpolation with multilevel B-splines. *IEEE Transactions on Visualization and Computer Graphics,*, *3*(3), 16. https://doi.org/10.1109/2945.620490

Legacy, T. N. (2020a). Sampling Protocols Version 1. *The Nansen Legacy Report Series*(9). https://doi.org/10.7557/nlrs.5715

Legacy, T. N. (2020b). Sampling Protocols Version 4.2. *The Nansen Legacy Report Series*(12). https://doi.org/10.7557/nlrs.5718

Legacy, T. N. (2020c). Sampling Protocols Version 5. *The Nansen Legacy Report Series*(13). https://doi.org/10.7557/nlrs.5719

Lind, S., Ingvaldsen, R. B., & Furevik, T. (2018). Arctic warming hotspot in the northern Barents Sea linked to declining sea-ice import. *Nature Climate Change*, *8*(7), 634-639. https://doi.org/10.1038/s41558-018-0205-y

Loeng, H. (1991). Features of the physical oceanographic conditions of the Barents Sea. *Polar Research*, *10*(1), 5-18. https://doi.org/10.3402/polar.v10i1.6723

Loeng, H., & Drinkwater, K. (2007). An overview of the ecosystems of the Barents and Norwegian Seas and their response to climate variability. *Deep Sea Research Part II: Topical Studies in Oceanography*, *54*(23-26), 2478-2500. https://doi.org/10.1016/j.dsr2.2007.08.013

Lomas, M. W., Baer, S. E., Acton, S., & Krause, J. W. (2019). Pumped Up by the Cold: Elemental Quotas and Stoichiometry of Cold-Water Diatoms [Original Research]. *Frontiers in Marine Science*, *6*. https://doi.org/10.3389/fmars.2019.00286

Makarevich, P. R., Larionov, V. V., Vodopyanova, V. V., Bulavina, A. S., Ishkulova, T. G., Venger, M. P., . . . Vashchenko, A. V. (2021). Phytoplankton of the Barents Sea at the Polar Front in Spring. *Oceanology*, *61*(6), 930-943. https://doi.org/10.1134/s0001437021060084

Marie, D., Partensky, F., Vaulot, D., & Brussaard, C. (1999). Enumeration of phytoplankton, bacteria, and viruses in marine samples. *Current protocols in cytometry*, *10*(1), 11.11. 11-11.11. 15.

Marquardt, M., Vader, A., Stübner, E. I., Reigstad, M., Gabrielsen, T. M., & Stams, A. J. M. (2016). Strong Seasonality of Marine Microbial Eukaryotes in a High-Arctic Fjord (Isfjorden, in West Spitsbergen, Norway). *Applied and*

Environmental Microbiology, *82*(6), 1868-1880. https://doi.org/doi:10.1128/AEM.03208-15

Marshall, H. G. (2002). Autotrophic picoplankton: Their presence and significance in marine and freshwater ecosystems. *Virginia Journal of Science*, *53*(1), 20.

Martin, J. H., & Knauer, G. A. (1973). The elemental composition of plankton. *Geochimica et Cosmochimica Acta*, *37*(7), 1639-1653. https://doi.org/10.1016/0016-7037(73)90154-3

Martiny, A. C., Pham, C. T. A., Primeau, F. W., Vrugt, J. A., Moore, J. K., Levin, S. A., & Lomas, M. W. (2013). Strong latitudinal patterns in the elemental ratios of marine plankton and organic matter. *Nature Geoscience*, *6*(4), 279-283. https://doi.org/10.1038/ngeo1757

Moder, K. (2016). How to keep the Type I Error Rate in ANOVA if Variances are Heteroscedastic. *Austrian Journal of Statistics*, *36*(3). https://doi.org/10.17713/ajs.v36i3.329

Morel, F. M. M., Milligan, A. J., & Saito, M. A. (2003). Marine bioinorganic chemistry: The role of trace metals in the oceanic cycles of major nutrients. *Treatise on Geochemistry*, *6*, 625. https://doi.org/10.1016/b0-08-043751-6/06108-9

Munn, C. B. (2019). *Marine microbiology: ecology & applications*. CRC Press.

Neukermans, G., Oziel, L., & Babin, M. (2018). Increased intrusion of warming Atlantic water leads to rapid expansion of temperate phytoplankton in the Arctic. *Global Change Biology*, *24*(6), 2545-2553. https://doi.org/10.1111/gcb.14075

Oziel, L., Baudena, A., Ardyna, M., Massicotte, P., Randelhoff, A., Sallée, J. B., . . . Babin, M. (2020). Faster Atlantic currents drive poleward expansion of temperate phytoplankton in the Arctic Ocean. *Nature Communications*, *11*(1). https://doi.org/10.1038/s41467-020-15485-5

Oziel, L., Neukermans, G., Ardyna, M., Lancelot, C., Tison, J. L., Wassmann, P., . . . Gascard, J. C. (2017). Role for Atlantic inflows and sea ice loss on shifting phytoplankton blooms in the Barents Sea. *Journal of Geophysical Research: Oceans*, *122*(6), 5121-5139. https://doi.org/10.1002/2016jc012582

Oziel, L., Sirven, J., & Gascard, J. C. (2016). The Barents Sea frontal zones and water masses variability (1980–2011). *Ocean Science*, *12*(1), 169-184. https://doi.org/10.5194/os-12-169-2016

Paulino, A. I., Heldal, M., Norland, S., & Egge, J. K. (2013). Elemental stoichiometry of marine particulate matter measured by wavelength dispersive X-ray fluorescence (WDXRF) spectroscopy. *Journal of the Marine Biological Association of the United Kingdom*, *93*(8), 2003-2014. https://doi.org/10.1017/s0025315413000635

Paulino, A. I., Larsen, A., Bratbak, G., Evens, D., Erga, S. R., Bye-Ingebrigtsen, E., & Egge, J. K. (2018). Seasonal and annual variability in the phytoplankton community of the Raunefjord, west coast of Norway from 2001–2006. *Marine Biology Research*, *14*(5), 421-435. https://doi.org/10.1080/17451000.2018.1426863

Paulsen, M. L., Dore, H., Garczarek, L., Seuthe, L., Muller, O., Sandaa, R. A., . . . Larsen, A. (2016). Synechococcus in the Atlantic gateway to the Arctic Ocean [Article]. *Frontiers in Marine Science*, *3*, 14, Article 191. https://doi.org/10.3389/fmars.2016.00191

Petsch, S. T. (2014). The global oxygen cycle. In H. D. Holland & K. K. Turekian (Eds.), *Treatise on Geochemistry* (2 ed., pp. 437-473). Elsevier. https://doi.org/https://doi.org/10.1016/B978-0-08-095975-7.00811-1

Piątek, J., Lenarczyk, J., & Piątek, M. (2020). Assessing morphological congruence in Dinobryon species and their stomatocysts, including a newly established Dinobryon pediforme–stomatocyst connection. *Scientific Reports*, *10*(1). https://doi.org/10.1038/s41598-020-65997-9

Price, N. B., & Skei, J. M. (1975). Areal and seasonal variations in the chemistry of suspended particulate matter in a deep water fjord. *Estuarine and Coastal Marine Science*, *3*(3), 349-369. https://doi.org/10.1016/0302-3524(75)90034-1

Quigg, A. (2008). Trace elements. In (pp. 3564-3573). Elsevier. https://doi.org/10.1016/b978-008045405-4.00311-6

Quigg, A., Finkel, Z. V., Irwin, A. J., Rosenthal, Y., Ho, T.-Y., Reinfelder, J. R., . . . Falkowski, P. G. (2003). The evolutionary inheritance of elemental stoichiometry in marine phytoplankton. *Nature*, *425*(6955), 291-294.

R Core Team. (2017). *R: A language and environment for statistical computing*. In R Foundation for Statistical Computing. https://www.R-project.org/

Rapp, J. Z., Fernández-Méndez, M., Bienhold, C., & Boetius, A. (2018). Effects of Ice-Algal Aggregate Export on the Connectivity of Bacterial Communities in the Central Arctic Ocean [Original Research]. *Frontiers in Microbiology*, *9*. https://doi.org/10.3389/fmicb.2018.01035

Redfield, A. C. (1934). On the proportions of organic derivatives in sea water and their relation to the composition of plankton. *James Johnstone memorial volume*, 16.

Rembauville, M., Blain, S., Caparros, J., & Salter, I. (2016). Particulate matter stoichiometry driven by microplankton community structure in summer in the Indian sector of the Southern Ocean. *Limnology and Oceanography*, *61*(4), 1301-1321. https://doi.org/10.1002/lno.10291

Rey, F. (2012). Declining silicate concentrations in the Norwegian and Barents Seas. *ICES Journal of Marine Science*, *69*(2), 208-212. https://doi.org/10.1093/icesjms/fss007

Rijkenberg, M. J. A., Slagter, H. A., Rutgers van der Loeff, M., van Ooijen, J., & Gerringa, L. J. A. (2018). Dissolved Fe in the deep and upper Arctic Ocean with a focus on Fe limitation in the Nansen Basin [Original Research]. *Frontiers in Marine Science*, *5*. https://doi.org/10.3389/fmars.2018.00088

Rosario Lorenzo, M., Iñiguez, C., Egge, J. K., Larsen, A., Berger, S. A., García-Gómez, C., & Segovia, M. (2018). Increased CO2 and iron availability effects on carbon assimilation and calcification on the formation of Emiliania huxleyi blooms in a coastal phytoplankton community. *Environmental and Experimental Botany*, *148*, 47-58. https://doi.org/10.1016/j.envexpbot.2017.12.003

Sakshaug, E., Andresen, K., Myklestad, S., & Olsen, Y. (1983). Nutrient status of phytoplankton communities in Norwegian waters (marine, brackish, and fresh) as revealed by their chemical composition. *Journal of Plankton Research*, *5*(2), 175-196. https://doi.org/10.1093/plankt/5.2.175

Sakshaug, E., Bjørge, A., Gulliksen, B., Loeng, H., & Mehlum, F. (1992). Økosystem Barentshavet.(The Barents Sea ecosystem). *Norges Allmennvitenskapelige Forskmingsrasd*.

Sakshaug, E., Johnsen, G. H., & Kovacs, K. M. (2009). *Ecosystem Barents Sea*. Tapir Academic Press.

Sanchez, N., Brown, E. A., Olsen, Y., Vadstein, O., Iriarte, J. L., Gonzalez, H. E., & Ardelan, M. V. (2018). Effect of Siderophore on Iron Availability in a Diatom and a Dinoflagellate Species: Contrasting Response in Associated Bacteria. *Frontiers in Marine Science*, *5*. https://doi.org/10.3389/fmars.2018.00118

Screen, J. A., & Simmonds, I. (2010). Increasing fall-winter energy loss from the Arctic Ocean and its role in Arctic temperature amplification. *Geophysical Research Letters*, *37*(16), n/a-n/a. https://doi.org/10.1029/2010gl044136

Sterner, R. W., & Elser, J. J. (2008). Ecological Stoichiometry: Overview. In (pp. 1101-1116). Elsevier. https://doi.org/10.1016/b978-008045405-4.00309-8

Sunda, W. G., & Huntsman, S. A. (1995). Iron uptake and growth limitation in oceanic and coastal phytoplankton. *Marine Chemistry*, *50*(1-4), 189-206. https://doi.org/10.1016/0304-4203(95)00035-p

Tamelander, T., Aubert, A., & Wexels Riser, C. (2012). Export stoichiometry and contribution of copepod faecal pellets to vertical flux of particulate organic carbon, nitrogen and phosphorus. *Marine Ecology Progress Series*, *459*, 17-28. https://doi.org/10.3354/meps09733

Ter Braak, C. J. F., & Verdonschot, P. F. M. (1995). Canonical correspondence analysis and related multivariate methods in aquatic ecology. *Aquatic Sciences*, *57*(3), 255-289. https://doi.org/10.1007/bf00877430

Thingstad, F. T., Skjoldal, E. F., & Bohne, R. A. (1993). Phosphorus cycling and algal-bacterial competition in Sandsfjord, western Norway. *Marine Ecology Progress Series*, *99*(3), 20. https://doi.org/10.2307/24837986

Thingstad, T. F., Øvreås, L., Egge, J. K., Løvdal, T., & Heldal, M. (2005). Use of non-limiting substrates to increase size; a generic strategy to simultaneously optimize uptake and minimize predation in pelagic osmotrophs? *Ecology Letters*, *8*(7), 675-682. https://doi.org/10.1111/j.1461-0248.2005.00768.x

Thomas, D. N., & Dieckmann, G. S. (2008). Sea ice: an introduction to its physics, chemistry, biology and geology.

Tortell, P. D., Maldonado, M. T., Granger, J., & Price, N. M. (1999). Marine bacteria and biogeochemical cycling of iron in the oceans. *FEMS Microbiology Ecology*, *29*(1), 1-11.

Trivedi, C. B., Lau, G. E., Grasby, S. E., Templeton, A. S., & Spear, J. R. (2018). Low-Temperature Sulfidic-Ice Microbial Communities, Borup Fiord Pass, Canadian High Arctic [Original Research]. *Frontiers in Microbiology*, *9*(1622). https://doi.org/10.3389/fmicb.2018.01622

Tréguer, P. J., & De La Rocha, C. L. (2013). The world ocean silica cycle. *Annual Review of Marine Science*, *5*(1), 477-501. https://doi.org/10.1146/annurev-marine-121211-172346

Twining, B. S., & Baines, S. B. (2013). The trace metal composition of marine phytoplankton. *Annual review of marine science*, *5*, 191-215.

Vader, A., Marquardt, M., Meshram, A. R., & Gabrielsen, T. M. (2015). Key Arctic phototrophs are widespread in the polar night. *Polar Biology*, *38*(1), 13-21. https://doi.org/10.1007/s00300-014-1570-2

Verdugo, P., Alldredge, A., Azam, F., Kirchman, D., Passow, U., & P, S. (2004). The oceanic gel phase: a bridge in the DOM-POM continuum. *Marine chemistry*, *92*(1/4, Spec. Iss.), 18.

Vihtakari, M. (2020). *PlotSvalbard: PlotSvalbard - Plot research data from Svalbard on maps*. In (Version R package version 0.9.2) https://github.com/MikkoVihtakari/PlotSvalbard

Volkman, J. K., & Tanoue, E. (2002). Chemical and biological studies of particulate organic matter in the ocean. *Journal of Oceanography*, *58*(2), 265-279. https://doi.org/10.1023/a:1015809708632

Vrede, T., & Kay, A. D. (2008). Organismal Ecophysiology. In (pp. 2587-2596). Elsevier. https://doi.org/10.1016/b978-008045405-4.00306-2

Wassmann, P., Kosobokova, K. N., Slagstad, D., Drinkwater, K. F., Hopcroft, R. R., Moore, S. E., . . . Berge, J. (2015). The contiguous domains of Arctic Ocean advection: Trails of life and death. *Progress in Oceanography*, *139*, 42-65. https://doi.org/10.1016/j.pocean.2015.06.011

White, A., & Dyhrman, S. (2013). The marine phosphorus cycle [Editorial]. *Frontiers in Microbiology*, *4*. https://doi.org/10.3389/fmicb.2013.00105

Wickam, H. (2016). *ggplot2: Elegant Graphics for Data Analysis* (2 ed.). Springer-Verlag New York.

Wilkinson, A. N., Zeeb, B. A., & Smol, J. P. (2001). Atlas of Chrysophycean Cysts. Developments in Hydrobiology,

Winter, A., Henderiks, J., Beaufort, L., Rickaby, R. E. M., & Brown, C. W. (2014). Poleward expansion of the coccolithophore Emiliania huxleyi. *Journal of Plankton Research*, *36*(2), 316-325. https://doi.org/10.1093/plankt/fbt110

Yoch, D. C. (2002). Dimethylsulfoniopropionate: Its sources, role in the marine food web, and biological degradation to dimethylsulfide. *Applied and Environmental Microbiology*, *68*(12), 5804-5815. https://doi.org/10.1128/aem.68.12.5804-5815.2002

Zubkov, M. V., Burkill, P. H., & Topping, J. N. (2006). Flow cytometric enumeration of DNA-stained oceanic planktonic protists. *Journal of Plankton Research*, *29*(1), 79-86. https://doi.org/10.1093/plankt/fbl059

Årthun, M., Eldevik, T., Smedsrud, L. H., Skagseth, Ø., & Ingvaldsen, R. B. (2012). Quantifying the Influence of Atlantic Heat on Barents Sea Ice Variability and Retreat*. *Journal of Climate*, *25*(13), 4736-4743. https://doi.org/10.1175/jcli-d-11-00466.1

6. Appendices

6.1. Supplementary methods

WDXRF

Equation 1. Formula and parameters used for the calculation of the particulate element concentration with WDXRF spectroscopy (Paulino et al., 2013).

$$Concentration = \frac{[\,(Count_s - Count_b) \times Filter\ Area \times (1000^2\ /\ Volume) \times Calibration\ Constant \times Drift\ Ratio\,]}{Molar\ Weight}$$

Where:

C : Concentration in µM

$Count_s$: Intensity count kC/s from the sample

$Count_b$: Intensity count kC/s from the blank filter

Filter Area : 9.078935

Volume : Volume of filtered sample

Element	Calibration Constant	Molar Weight	Detection Limits	Drift Ratio
O	0.0025	16	0.0613	1.097674419
Na	0.000146	22.99	0.0014	1
Mg	0.00008	24.31	0.0005	1.002502433
Si	0.000116	28.09	0.0035	0.921142857
P	0.00053186	30.97	0.0006	0.889416984
S	0.000055	32.06	0.0002	0.889416984
Cl	0.000255	35.45	0.0048	0.889416984
K	0.00020299	39.1	0.0012	1.002231036
Ca	0.000295	40.08	0.0015	1.005437056
Mn	0.000495	54.94	0.0011	1.039370079
Fe	0.000258	55.85	0.0015	1.02688172
Cu	0.000142	63.55	0.0014	1
Zn	0.000155	65.37	0.0014	1

Chlorophyll *a* concentration

Samples for chlorophyll *a* were acquired by Miriam Marquardt (UiT, Miriam.marquardt@uit.no). The methodology described here is available in The Nansen Legacy Protocols and method responsible are Rolf Gradinger (UiT, rolf.gradinger@uit.no), Anna Vader (UNIS, anna.vader@unis.no) and Miriam Marquardt (UiT, Miriam.marquardt@uit.no. Samples were collected from the Niskin bottles from standard depths ((5), 10, 20, 30, 40, 50, 60, 90, 120, (150), 200, chlorophyll-a-maximum and bottom (~15m from the seafloor)) and stored in clean

plastic bottles. The bottles were cleaned with distilled water and rinsed with sample water prior to filling. Light exposure of the samples during the sampling process was avoided by covering the bottles with black plastics bags and storing them in dark and cold location until filtration. Prior to filtration the water bottles were gently mixed. Filtration took place under dark conditions using 50-1000 ml from each depth through 25 mm GF/F filters and 10 µm Polycarbonate filters with low vacuum pressure (about -30 kPa). The filtration funnels were covered with tin foils during the process and, were rinsed with filtered sea water once the samples were through. Afterwards, the filters were placed in 10 ml labelled Polypropylene (PP) tubes. Five ml of ethanol was added to each tube and left for 24 hours at 4 degrees in the dark for extraction. After extraction, samples were left to reach room temperature for 30 minutes. A TURNER 10-AU fluorometer was used for measurement of chlorophyll and phaeopigments took place under darkness. A blank sample (methanol only) was used to calibrate the reading at zero before measuring the samples, in between sample measurements. Samples were transferred in clean (borosilicate) cuvettes and Rb fluorescence was noted. Ra fluorescence was measured after 90 seconds after the addition of 2 drops of 5% HCl. Chlorophyll α concentration was calculated using Equation 2.

Equation 2. Formulas for the calculation of algal photosynthetic pigments (chlorophyll α and phaeopigments), measured by fluorometric acidification.

For chlorophyll *a* concentration (C, µg/L):

$$C = F\ s\ (r/(r-1))(R\ b\ - R\ a\ )V\ ex\ /V\ sam$$

Where:

Fs : response factor for the sensitivity setting S,

r : the before-to-after acidification ratio of a pure chlorophyll *a* solution, Rb : fluorescence of sample extract before acidification,

Ra : fluorescence of sample extract after acidification,

Vex : extraction volume (L, 0.005L suggested),

Vsam : volume filtered sample (L).

Abundance of bacteria and small protists

The samples for flowcytometry were analysed by Elzbieta Anna Petelenz (University of Bergen, Elzbieta.Kurdziel@uib.no) and Maria Rigstad Langvad (University of Bergen, Maria.Langvad@uib.no). The method responsible are Aud Larsen (Uni Research/Norce, aula@norceresearch.no) and Gunnar Bratbak (UIB, Gunnar.Bratbak@uib.no) and a detailed explanation is included in The Nansen

Legacy Protocols. The methodology for determination of the characteristic microbial groups in the water samples was adapted based on the protocols of (Marie et al., 1999) and (Zubkov et al., 2006). Thirty eight µl of 25% glutaraldehyde was added in labeled cryovials (3 vials per sampling depth) under the fume hood. Water samples from the standard depths (5, 10, 25, 50, 75, 100, 200, chlorophyll-a-maximum and bottom (~15m from the seafloor)) were collected from the Niskin bottles into 20 ml scintillation vials. Then, 1.8 ml of each sample was added into the corresponding cryovials and were left for 2 hours in a fridge to complete the fixation. Finally, the cryovials were snap-freezed in liquid N and stored in dry ice at -80°C until further processing. Prior to analysis the water samples were thawed. The samples for HNF and bacteria were stained with SYBR Green I (Molecular Probes, Eugene, Oregon, USA) for ~1 hour, while the samples for the rest of the groups were counted directly. Enumeration of cell abundances was done on an Attune® Acoustic Focusing Flow Cytometer (Applied Biosystems by Life technologies) with a syringe-based fluidic system and a 20 mW 488 nm (blue) laser.

6.2. Tables

Table 2. Results of the Shapiro Wilk normality test for the assessment of the distribution of the dataset.

Shapiro Wilk normality test	Statistic	p-value
Temperature (°C)	0.880515	3.38E-08***
Salinity (PSU)	0.834989	4.70E-10***
Chlorophyll *a* (µg L-1)	0.51799	6.90E-18***
PartO (µM)	0.689204	1.61E-22***
PartP (µM)	0.730411	1.63E-23***
PartS (µM)	0.799597	1.77E-19***
PartCa (µM)	0.547222	3.54E-29***
PartSi (µM)	0.586954	3.98E-28***
PartFe (µM)	0.478719	3.25E-30***
PartCu (µM)	0.912812	0.020126*
PartMn (µM)	0.674551	5.02E-20***
PartK (µM)	0.634037	1.45E-26***
PartNa (µM)	0.649167	1.80E-25***
PartCl (µM)	0.656414	1.35E-24***
PartMg (µM)	0.778396	1.53E-21***
PartZn (µM)	0.850436	0.000161***
Picophytoplankton (mL^{-1})	0.657118	1.27E-12***
Nanophytoplankton (mL^{-1})	0.712795	1.89E-11***
Heterotrophic Nanoflagellates (mL^{-1})	0.790361	1.60E-09***
Bacteria (mL^{-1})	0.715362	9.32E-14***

*,P<0.05;**,P<0.01;***,P<0.001

Table 3. Welch's ANOVA results for the comparison between the August 2018 and August 2019.

One-way analysis of means (Not assuming equal variances)	Degrees of freedom	F statistic	p-value
Temperature (°C)	80.88375	26.34134	1.93E-06***
Salinity (PSU)	58.29764	3.29165	0.07478
Chlorophyll *a* (µg L-1)	40.92893	16.41452	0.000222***
PartO (µM)	185.8705	9.216147	0.002743***
PartP (µM)	234.1259	2.058183	0.152725
PartS (µM)	206.4523	21.11143	7.54E-06***
PartCa (µM)	153.3302	4.665291	0.032332*
PartSi (µM)	238.2124	11.02445	0.00104**
PartFe (µM)	218.5882	0.405219	0.525072
PartMn (µM)	89.43773	0.083868	0.772793
PartK (µM)	224.5615	12.81064	0.000422***
PartNa (µM)	150.8606	87.55012	1.08E-16***
PartCl (µM)	223.6484	29.15283	1.70E-07***
PartMg (µM)	242.0329	61.59622	1.36E-13***
Picophytoplankton (mL^{-1})	75.93356	0.922868	0.339772
Nanophytoplankton (mL^{-1})	61.00357	9.694687	0.002813**
Heterotrophic Nanoflagellates (mL^{-1})	78.09385	1.25161	0.266675
Bacteria (mL^{-1})	52.49023	13.86374	0.000481***

*,P<0.05;**,P<0.01;***,P<0.001

Table 4. Pearson's correlation test results between elemental concentrations and microbial abundances against depth, temperature salinity and chlorophyll a for August 2018.

Statistical Correlation	Depth (m)	Temperature (°C)	Salinity (PSU)	Chlorophyll *a* (µg L^{-1})
PartO (µM)	0.507**	-0.03	0.323*	0.014
PartP (µM)	-0.378*	0.515***	-0.088	0.717***
PartS (µM)	-0.480**	0.647***	-0.058	0.726***
PartCa (µM)	-0.246	0.570***	0.247	0.157
PartSi (µM)	0.607***	-0.136	0.328*	-0.163
PartFe (µM)	0.598***	-0.181	0.29	-0.178
PartMn (µM)	0.521*	-0.479	0.065	-0.194
PartK (µM)	0.573***	-0.134	0.314*	-0.118
PartNa (µM)	0.092	0.104	0.209	-0.095
PartCl (µM)	-0.084	0.146	0.134	-0.116
PartMg (µM)	0.512***	0.007	0.325*	-0.021
Picophytoplankton (mL^{-1})	-0.490***	0.288	-0.697***	0.310*
Nanophytoplankton (mL^{-1})	-0.444**	0.577***	-0.069	0.707***
Heterotrophic Nanoflagellates (mL^{-1})	-0.416**	-0.088	-0.444**	0.18
Bacteria (mL^{-1})	-0.532***	0.385*	-0.521***	0.425**

*,P<0.05;**,P<0.01;***,P<0.001

Table 5. Pearson's correlation test results between elemental concentrations against microbial abundances above 100m depth for August *2018*.

Statistical Correlation	Picophytoplankton (mL^{-1})	Nanophytoplankton (mL^{-1})	Heterotrophic Nanoflagellates (mL^{-1})	Bacteria (mL^{-1})
PartO (µM)	-0.166	0.892***	-0.034	0.282
PartP (µM)	-0.01	0.871***	0.184	0.419*
PartS (µM)	0.045	0.858***	0.079	0.446*
PartCa (µM)	-0.148	0.147	-0.239	0.099
PartSi (µM)	-0.288	0.627***	-0.401*	0.088
PartFe (µM)	-0.038	0.01	-0.298	-0.136
PartMn (µM)	0.626	-0.334	-0.408	0.663
PartK (µM)	-0.212	0.630***	0.158	0.124
PartNa (µM)	0.091	0.054	0.115	0.376*
PartCl (µM)	0.068	-0.13	-0.022	0.121
PartMg (µM)	0.044	0.693***	0.011	0.449*

*,P<0.05;**,P<0.01;***,P<0.001

Table 6. Pearson's correlation test results between elemental concentrations for August 2018.

Statistical Correlation	PartMg (µM)	PartCl (µM)	PartNa (µM)	PartK (µM)	PartMn (µM)	PartFe (µM)	PartSi (µM)	PartCa (µM)	PartS (µM)	PartP (µM)	PartO (µM)
PartO (µM)	0.957***	-0.282	0.014	0.965***	0.449	0.945***	0.959***	0.085	0.058	0.353*	1
PartP (µM)	0.305*	-0.137	0.025	0.231	0.237	0.109	0.136	0.379*	0.874***	1	
PartS (µM)	0.12	0.228	0.330*	-0.037	-0.223	-0.171	-0.136	0.426**	1		
PartCa (µM)	0.17	0.383*	0.246	0.061	-0.196	0.003	0.034	1			
PartSi (µM)	0.950***	-0.193	0.072	0.988***	0.472	0.996***	1				
PartFe (µM)	0.935***	-0.201	0.059	0.983***	0.491*	1					
PartMn (µM)	0.438	-0.517*	-0.015	0.487*	1						
PartK (µM)	0.967***	-0.156	0.131	1							
PartNa (µM)	0.303*	0.867***	1								
PartCl (µM)	0.02	1									
PartMg (µM)	1										

*,P<0.05;**,P<0.01;***,P<0.001

Table 7. Pearson's correlation test results between elemental concentrations and microbial abundances against depth, temperature salinity and chlorophyll a for August 2019.

Statistical Correlation	Depth (m)	Temperature (°C)	Salinity (PSU)	Chlorophyll *a* (µg L^{-1})
PartO (µM)	0.466**	0.083	0.077	0.218
PartP (µM)	-0.401*	0.032	-0.686***	0.924***
PartS (µM)	-0.568***	0.036	-0.713***	0.767***
PartCa (µM)	0.058	0.187	-0.144	0.13
PartSi (µM)	0.507***	0.066	0.179	0.124
PartFe (µM)	0.798***	-0.101	0.345*	-0.321*
PartMn (µM)	0.695***	-0.071	0.393*	-0.351
PartK (µM)	0.612***	-0.051	0.127	0.028
PartNa (µM)	-0.425**	-0.136	-0.685***	0.592***
PartCl (µM)	-0.415**	-0.059	-0.547***	0.374*
PartMg (µM)	0.056	-0.163	-0.479**	0.420**
Picophytoplankton (mL^{-1})	-0.479**	0.121	-0.825***	0.297
Nanophytoplankton (mL^{-1})	-0.573***	0.09	-0.766***	0.793***
Heterotrophic Nanoflagellates (mL^{-1})	-0.436**	-0.218	-0.552***	0.686***
Bacteria (mL^{-1})	-0.497**	-0.245	-0.792***	0.497**

*,P<0.05;**,P<0.01;***,P<0.001

Table 8. Pearson's correlation test results between elemental concentrations and microbial abundances above 100m depth for August *2019*.

Statistical Correlation	Picophytoplankton (mL^{-1})	Nanophytoplankton (mL^{-1})	Heterotrophic Nanoflagellates (mL^{-1})	Bacteria (mL^{-1})
PartO (µM)	0.054	0.465*	0.069	0.063
PartP (µM)	0.359	0.763***	0.637***	0.492**
PartS (µM)	0.444*	0.835***	0.584***	0.517**
PartCa (µM)	0.195	0.274	0.221	0.17
PartSi (µM)	-0.047	0.252	-0.132	-0.091
PartFe (µM)	-0.339	-0.396*	-0.347	-0.471**
PartMn (µM)	-0.445*	-0.590**	-0.476*	-0.392
PartK (µM)	0.052	0.456*	0.194	0.024
PartNa (µM)	0.464**	0.717***	0.416*	0.576***
PartCl (µM)	0.389*	0.508**	0.259	0.438*
PartMg (µM)	0.460*	0.735***	0.443*	0.544**

*,P<0.05;**,P<0.01;***,P<0.001

Table 9. Pearson's correlation test results between elemental concentrations for August 2019

Statistical Correlation	PartMg (µM)	PartCl (µM)	PartNa (µM)	PartK (µM)	PartMn (µM)	PartFe (µM)	PartSi (µM)	PartCa (µM)	PartS (µM)	PartP (µM)	PartO (µM)
PartO (µM)	0.441**	-0.154	-0.053	0.856***	0.673***	0.724***	0.958***	0.410**	-0.034	0.29	1
PartP (µM)	0.489**	0.331*	0.568***	0.133	-0.262	-0.186	0.136	0.302	0.776***	1	
PartS (µM)	0.659***	0.739***	0.865***	-0.046	-0.426*	-0.376*	-0.197	0.312*	1		
PartCa (µM)	0.561***	0.303	0.257	0.532***	0.165	0.387*	0.273	1			
PartSi (µM)	0.326*	-0.201	-0.136	0.807***	0.705***	0.713***	1				
PartFe (µM)	0.349*	-0.281	-0.274	0.888***	0.799***	1					
PartMn (µM)	0.279	-0.387*	-0.332	0.695***	1						
PartK (µM)	0.615***	-0.002	0.043	1							
PartNa (µM)	0.784***	0.939***	1								
PartCl (µM)	0.718***	1									
PartMg (µM)	1										

*,P<0.05;**,P<0.01;***,P<0.001

Table 10. Canonical Correspondence Analysis model summary for August 2018.

Model: cca(formula = celldata ~ P + O + S + Si + Ca + Na + Mg + K + Cl + Fe + Mn + Sal + Temp)		
	Inertia	Proportion
Total	0.058177	1
Constrained	0.048487	0.8334
Unconstrained	0.009689	0.1666

Table 11. Eigenvalues and proportion of variance explained by each axis for CCA model August 2018.

Accumulated Constrained Eigenvalues				
	CCA1	CCA2	CCA3	CCA4
Eigenvalue	0.0407	0.004944	0.002834	7.422e-06
Proportion Explained	0.8394	0.101971	0.058450	1.531e-04
Cumulative Proportion	0.8394	0.941397	0.999847	1

Table 12. Results of the permutation test for the CCA model August 2018. Number of permutations:999.

	Df	ChiSquare	F	Pr(>F)
Model	13	0.048487	11.163	0.001***
Residual	29	0.009689		

,P<0.05;,P<0.01;***,P<0.001*

Table 13. Results of the permutation test for the CCA axes August 2018. Number of permutations:999

	Df	ChiSquare	F	Pr(>F)
CCA1	1	0.040701	159.624	0.001***
CCA2	1	0.004944	19.3906	0.006**
CCA3	1	0.002834	11.1148	0.107
CCA4	1	0.000007	0.0291	1
Residual	38	0.009689		

,P<0.05;,P<0.01;***,P<0.001*

.

Table 14. Results of the permutation test for the CCA model terms added sequentially from first to last, August 2018. Number of permutations:999.

	Df	ChiSquare	F	Pr(>F)
PartP	1	0.016202	48.4919	0.001***
PartO	1	0.005184	15.5143	0.001***
PartS	1	0.004764	14.2575	0.001***
PartSi	1	0.003246	9.7153	0.002**
PartCa	1	0.000428	1.2816	0.249
PartNa	1	0.002221	6.6474	0.007**
PartMg	1	0.002246	6.7218	0.009**
PartK	1	0.003692	11.0485	0.001***
PartCl	1	0.000374	1.1193	0.314
PartFe	1	0.002183	6.532	0.006**
PartMn	1	0.00011	0.3282	0.727
Sal	1	0.005615	16.8041	0.001***
Temp	1	0.002225	6.6591	0.008**
Residual	29	0.009689		

,P<0.05;,P<0.01;***,P<0.001*

Table 15. Canonical Correspondence Analysis model summary for August 2019.

Model: cca(formula = celldata2 ~ P + O + S + Si + Ca + Na + Mg + K + Cl + Fe + Mn+ Sal + Temp)		
	Inertia	Proportion
Total	0.030791	1
Constrained	0. 022643	0.7354
Unconstrained	0. 008148	0.2646

Table 16. Eigenvalues and proportion of variance explained by each axis for CCA model August 2019

	CCA1	CCA2	CCA3	CCA4
Eigenvalue	0.01883	0.003039	0.0007624	1.63E-05
Proportion Explained	0.83139	0.134226	0.0336712	7.12E-04
Cumulative Proportion	0.83139	0.965616	0.9992877	1

Table 17. Results of the permutation test for the CCA model August 2019. Number of permutations:999.

	Df	ChiSquare	F	Pr(>F)
Model	13	0.022643	5.3442	0.001***
Residual	25	0.008148		

,P<0.05;,P<0.01;***,P<0.001*

Table 18. Results of the permutation test for the CCA axes August 2019. Number of permutations:999.

	Df	ChiSquare	F	Pr(>F)
CCA1	1	0.018825	78.5546	0.001***
CCA2	1	0.003039	12.6825	0.196
CCA3	1	0.000762	3.1815	0.992
CCA4	1	1.61E-05	0.0673	1
Residual	34	0.008148		

,P<0.05;,P<0.01;***,P<0.001*

Table 19. Results of the permutation test for the CCA model terms added sequentially from first to last, August 2019. Number of permutations:999.

	Df	ChiSquare	F	Pr(>F)
PartP	1	0.005793	17.7734	0.001***
PartO	1	0.000367	1.1247	0.314
PartS	1	0.001516	4.6528	0.025*
PartSi	1	9.55E-05	0.2931	0.733
PartCa	1	0.001781	5.4643	0.018*
PartNa	1	0.000176	0.5413	0.514
PartMg	1	0.004158	12.7579	0.001***
PartK	1	0.000255	0.7819	0.43
PartCl	1	0.000495	1.5178	0.222
PartFe	1	0.000998	3.0631	0.074
PartMn	1	0.001043	3.1995	0.061
Sal	1	0.005084	15.5992	0.001***
Temp	1	0.000882	2.7059	0.102
Residual	25	0.008148		

,P<0.05;,P<0.01;***,P<0.001*

Table 20. Elemental quotas in planktonic or suspended PM in field studies and culture experiments as calculated by Ho et al 2003.

Element quota to P mol/mol	**Collier and Edmond 1984 North Pacific Ocean**	**Kuss and Kremling 1999 Atlantic Ocean**	**Ho et al. 2003 Nutrient replete cultures**	**This study 2018 North-West Barents Sea**	**This study 2019 North-West Barents Sea**
K	NA	NA	1.7 (1.4)	0.12(0.07)	0.38(0.26)
Mg	NA	NA	0.56 (0.58)	0.39(0.33)	1.05(0.71)
Ca	5.1(0.1)	5.4 (2.1)	0.52 (0.51)	1.1(2.4)	0.6(0.4)
Fe	0.0046 (0.00066)	0.0046 (0.0013)	0.0075 (0.0053)	0.11(0.09)	0.27(0.34)
Mn	0.00034 (0.00004)	0.0016 (0.00018)	0.0038 (0.0024)	0.05(0.02)	0.09(0.1)

6.3. Elemental quotas

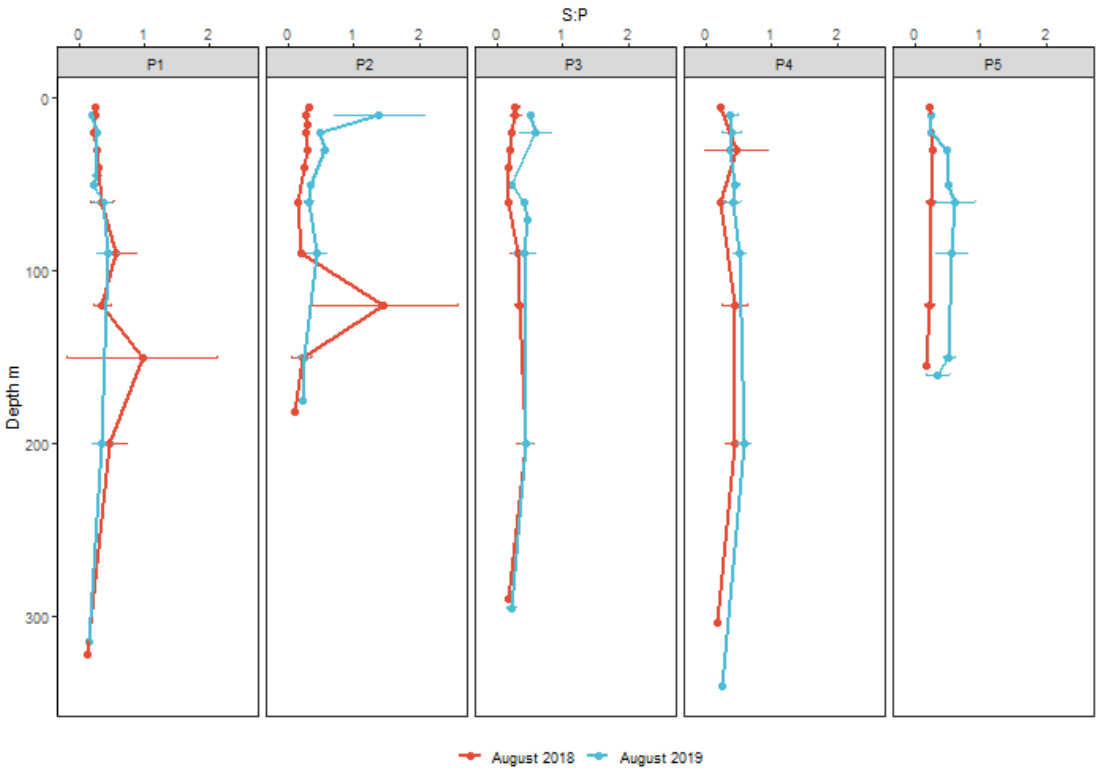

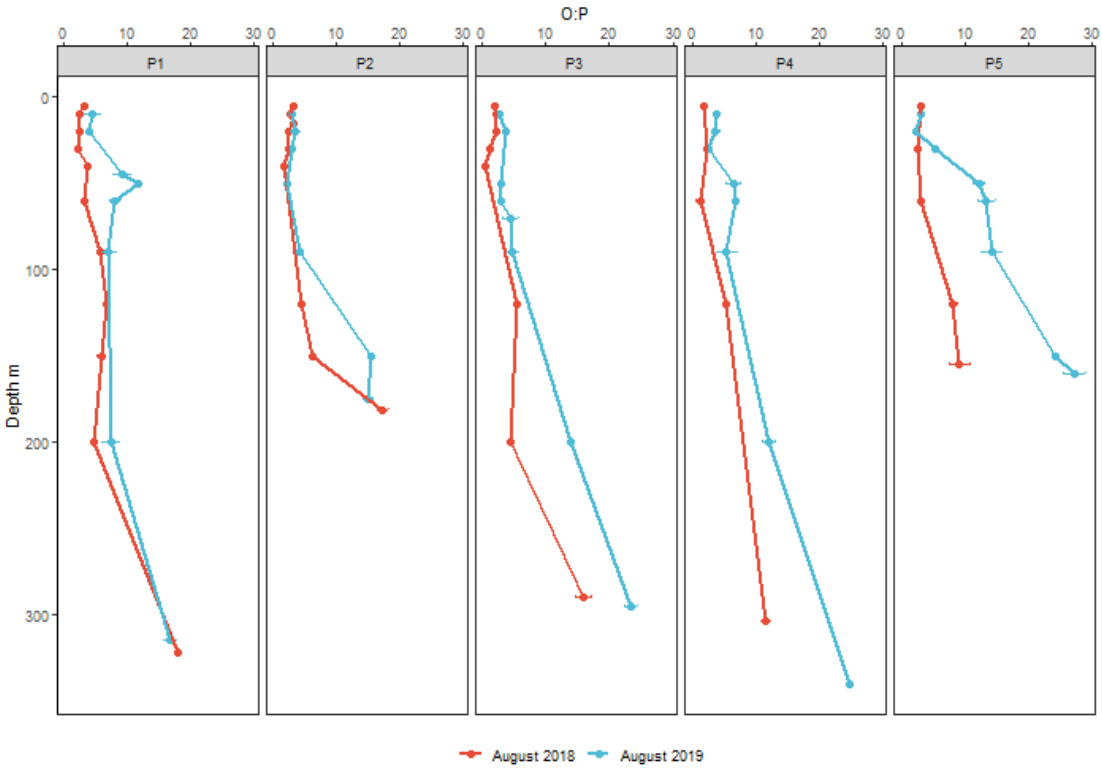

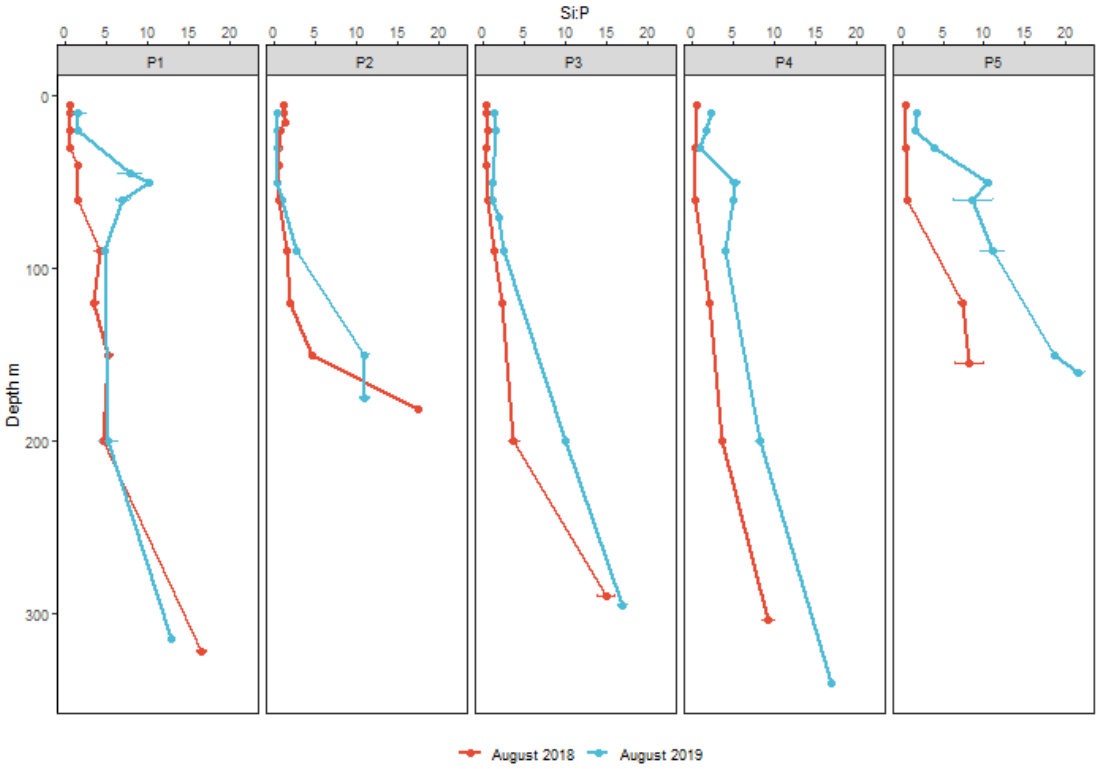
Si:P
P1
P2
P3
P4
P5
Depth m
0
100
200
300
0 5 10 15 20
August 2018
August 2019

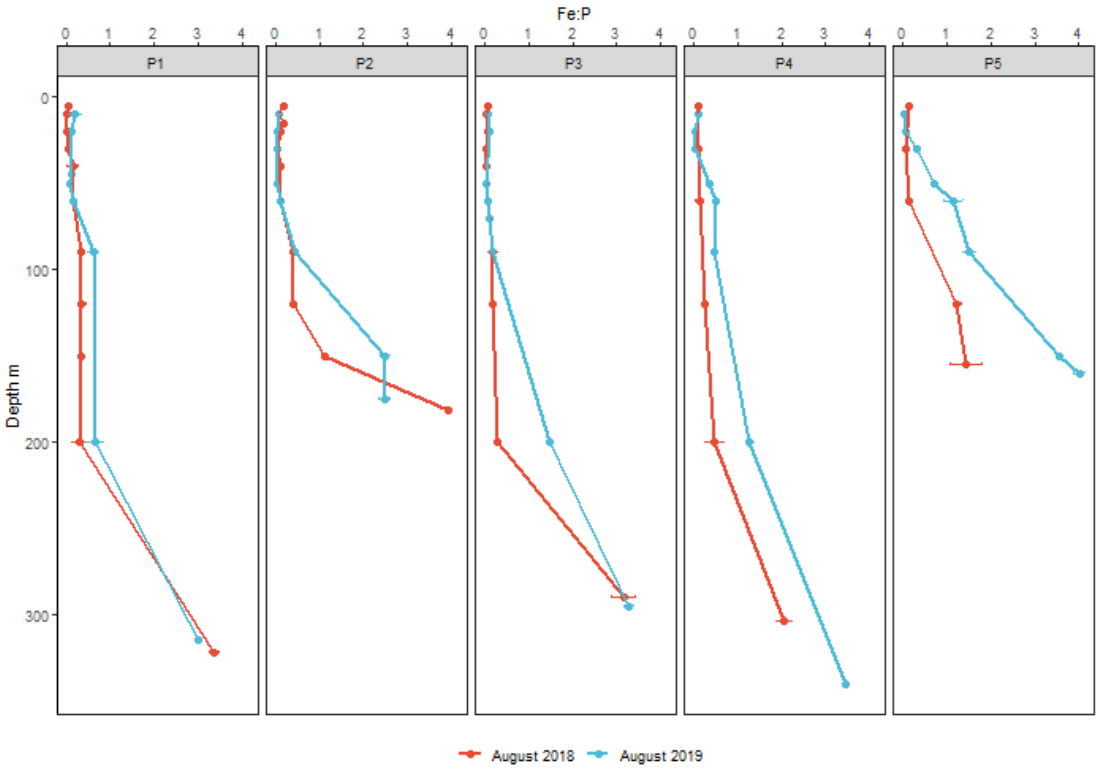
Fe:P
P1
P2
P3
P4
P5
Depth m
0
100
200
300
0 1 2 3 4
August 2018
August 2019

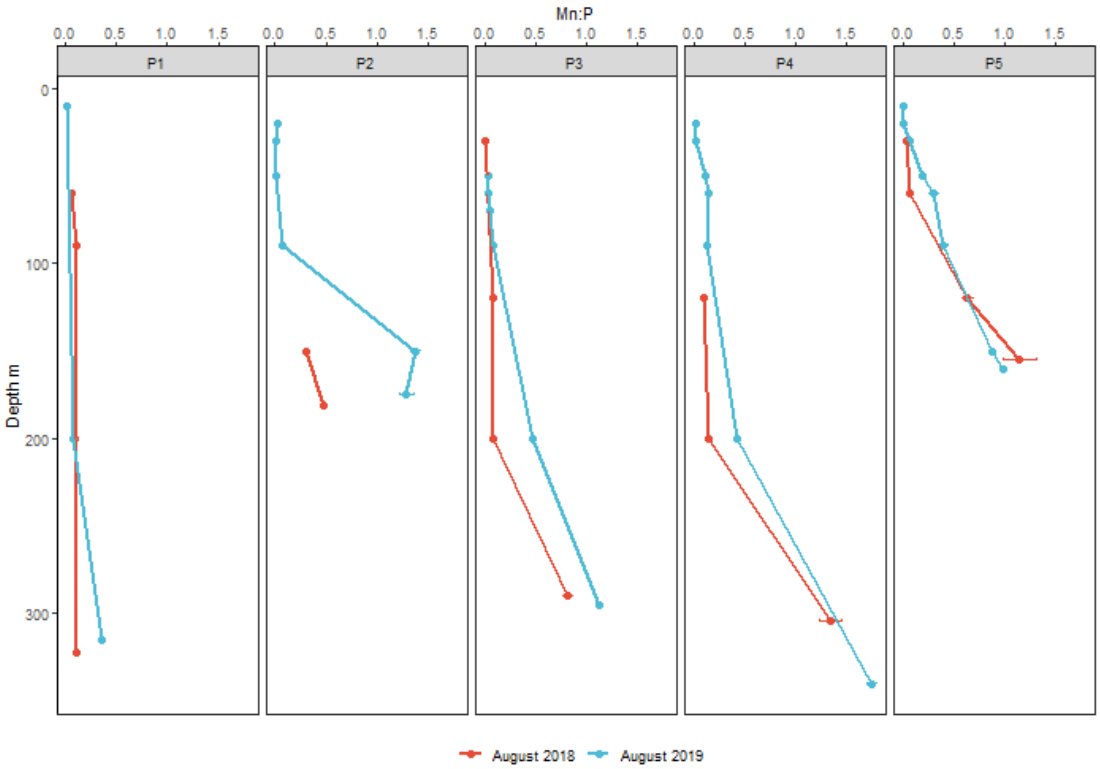
Mn:P
0.0 0.5 1.0 1.5
P1
P2
P3
P4
P5
Depth m
0
100
200
300
August 2018
August 2019

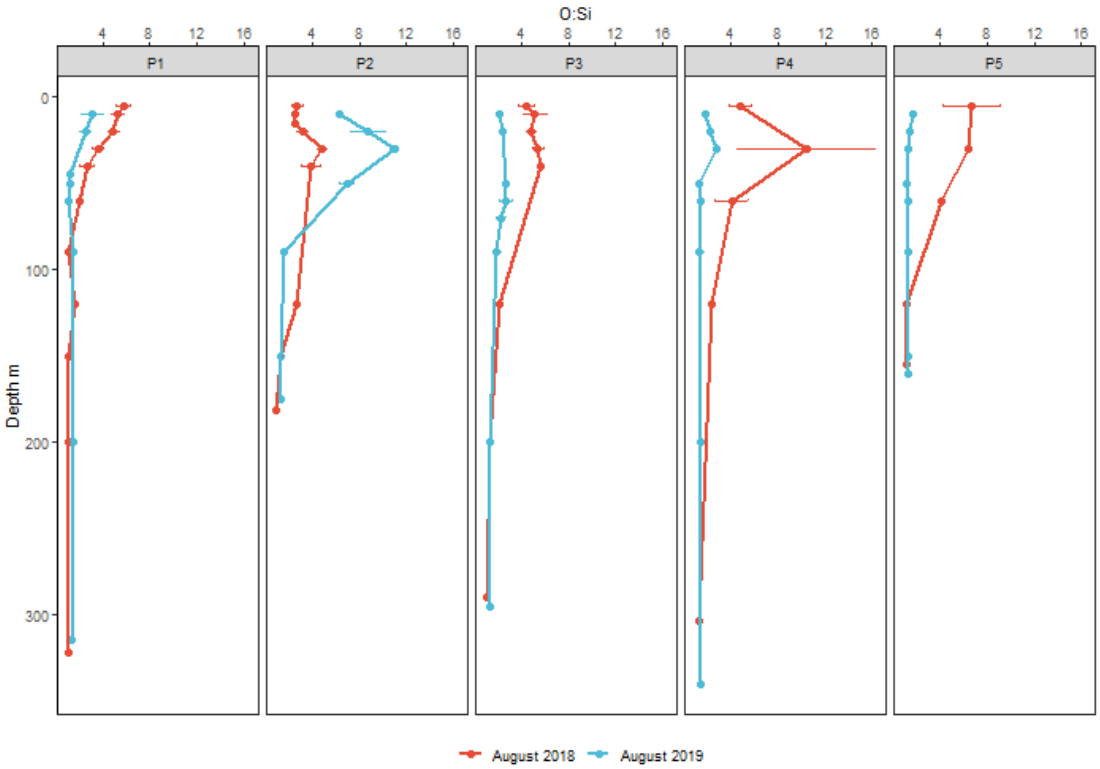
O:Si
4 8 12 16
P1
P2
P3
P4
P5
Depth m
0
100
200
300
August 2018
August 2019

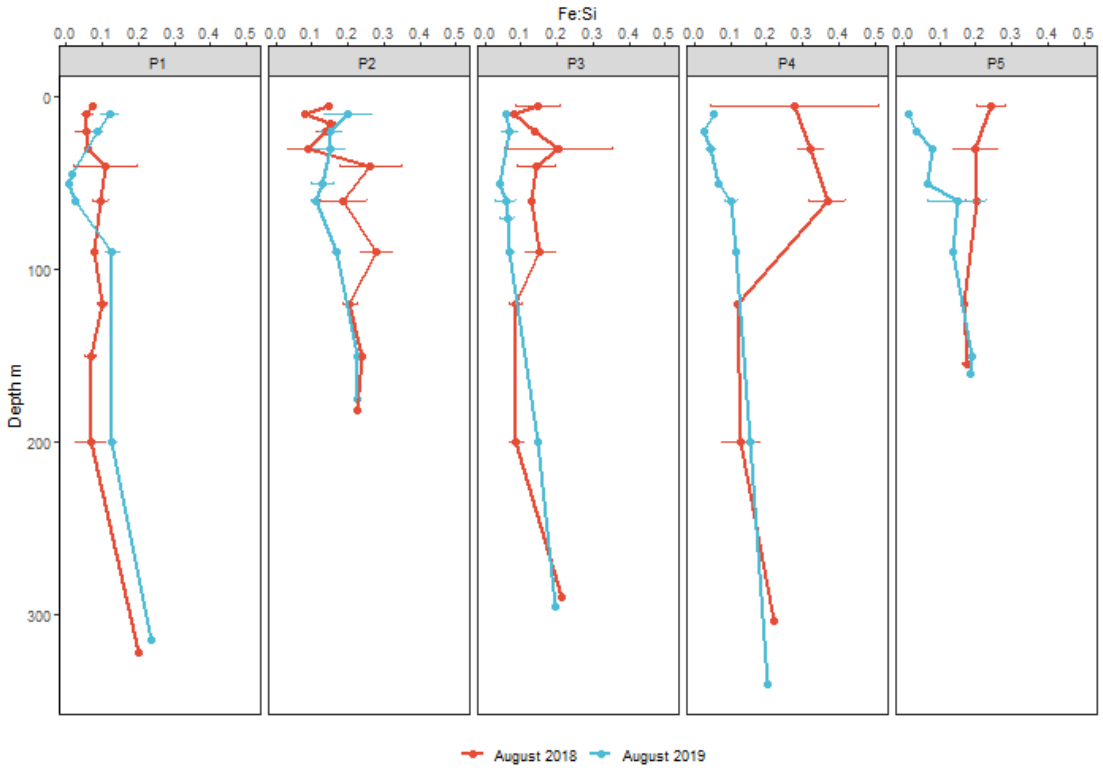
Fe:Si
0.0 0.1 0.2 0.3 0.4 0.5
P1
P2
P3
P4
P5
Depth m
0
100
200
300
August 2018
August 2019